UNIVERSITÉ DE MONTRÉAL

GENERAL FORMULATION AND ACCURATE EVALUATION OF EARTH-RETURN PARAMETERS FOR OVERHEAD / UNDERGROUND CABLES

HAOYAN XUE

DÉPARTEMENT DE GÉNIE ÉLECTRIQUE

ÉCOLE POLYTECHNIQUE DE MONTRÉAL

THÈSE PRÉSENTÉE EN VUE DE L'OBTENTION

DU DIPLÔME DE PHILOSOPHIAE DOCTOR

(GÉNIE ÉLECTRIQUE)

AOÛT 2018

© Haoyan Xue, 2018.

UNIVERSITÉ DE MONTRÉAL

ÉCOLE POLYTECHNIQUE DE MONTRÉAL

Cette thèse intitulée:

GENERAL FORMULATION AND ACCURATE EVALUATION OF EARTH-RETURN PARAMETERS FOR OVERHEAD / UNDERGROUND CABLES

présentée par : XUE Haoyan

en vue de l'obtention du diplôme de : Philosophiae Doctor

a été dûment acceptée par le jury d'examen constitué de :

M. KOCAR Ilhan, Ph. D., président

M. MAHSEREDJIAN Jean, Ph. D., membre et directeur de recherche

M. AMETANI Akihiro, Ph. D., membre et codirecteur de recherche

M. SHESHYEKANI Keyhan, Ph. D., membre

M. PAPADOPOULOS Theofilos, Ph. D., membre externe

DEDICATION

To My Son, Anthony Jiahui XUE

ACKNOWLEDGEMENTS

Foremost, I would like to express my very great appreciation to my Ph.D. supervisor Prof. Jean Mahseredjian for the continuous support of my research and the valuable study opportunity in Polytechnique Montréal.

I would like to express my sincere gratitude to my co-supervisor Prof. Akihiro Ametani for his patience, motivation and comprehensive knowledge. Advice given by him has been a great help in all the time of research.

Discussion and assistance provided by co-supervisor Prof. Ilhan Kocar were much appreciated.

I would like to offer my special thanks to Prof. Piero Triverio and Mr. Utkarsh Patel for the comprehensive understanding of MoM-SO.

I would also like to thank Diane Desjardins and Gwendoline Le Bomin for their help in my French studies.

All colleagues at the department for their friendship and support. To those who already left: Isabel Lafaia, Baki Cetindag, Louis Filliot, Xiaopeng Fu, Fidji Diboune and Serigne Seye. To those who will continue: Anas Abusalah, Ming Cai, Jesus Morales, Miguel Martinez, Anton Stepanov, Aboutaleb Haddadi, Reza Hassani, Thomas Kauffmann, Masashi Natsui, David Tobar, Nazak Soleimanpour, Maryam Torabi, Amir Sadati and Willy Mimbe.

Finally, I would like to thank my family: my parents Feng Xue and Ming Wan, my wife Yanfei Liu for their support and encouragement.

RÉSUMÉ

La simulation de transitoire électromagnétique (EMT) dans les réseaux électriques est devenue un outil important pour la recherche et les applications pratiques. Les outils de simulation de type EMT nécessitent des modèles de ligne / câble aérien(ne) et de câble souterrain qui sont basés sur le calcul de paramètres d'impédance série et d'admittance shunt. Ces paramètres sont calculés en utilisant des données géométriques du système de transmission et des paramètres physiques. Un aspect important dans les calculs est la formulation de l'impédance et l'admittance de retour à la terre.

Premièrement, dans cette thèse, les formules nouvelles et généralisées d'impédance et d'admittance de retour à la terre sont dérivées pour une ligne aérienne et un câble souterrain, en se basant sur les équations de Maxwell avec des conditions initiales et aux limites complètes. De plus, les composantes complètes du champ électromagnétique émis sur la ligne aérienne et le câble souterrain sont dérivées. Afin d'éviter les difficultés numériques de la résolution complète, les formules d'impédance et d'admittance de retour à la terre sont simplifiées en adoptant les hypothèses appropriées. Ensuite, les formules approximées d'impédance et d'admittance de retour à la terre sont proposées pour le câble souterrain. Grâce à l'absence d'intégrale de Sommerfeld, les formules approximées peuvent être calculées facilement. Les formules existantes telles que les formules de retour à la terre par Pollaczek et Carson se déduisent simplement si les mêmes conditions sont adoptées dans la formulation généralisée proposée. Une Green fonction modifiée de retour à la terre de la méthode Method of Moment (MoM) - Surface Admittance Operator (SO) pour la ligne / le câble aérien(ne) est aussi dérivée. La stabilité numérique du MoM-SO pour la ligne / le câble aérien(ne) est améliorée en adoptant la Green fonction dérivée.

Ensuite, le concept de méthode de ligne de transmission (TL) étendue est proposé par rapport à la méthode de TL classique. En adoptant la méthode de TL étendue, l'allure des réponses en fréquence montrent des améliorations et des impacts significatifs dans les hautes fréquences pour une ligne aérienne, un câble aérien et un câble souterrain. Il est bien connu qu'il existe une transition de mode pour les lignes et les câbles aériens qui transforme l'onde de retour à la terre dans les fréquences basses en l'onde de surface dans les fréquences hautes. L'atténuation plus faible de l'onde de surface montre une différence significative pour les fonctions de propagation évaluées par la méthode de TL classique. Ensuite, les caractéristiques de l'onde de propagation du câble souterrain sont

évaluées par la méthode de TL étendue. L'influence des paramètres du sol, comme la résistivité et la permittivité de la terre, est clarifiée pour les caractéristiques de l'onde de propagation dans le domaine fréquentiel.

Suite à l'analyse du domaine fréquentiel, des simulations transitoires utilisant la méthode TL étendue sont effectuée aussi pour différentes applications aux réseaux électriques. Pour la première, le pic de tension du front d'onde de réponse à un échelon dans le domaine temporel est observé pour un bus simple à isolation gazeuse (GIB), car l'atténuation est plus faible dans les hautes fréquences. Ce phénomène explique que les tensions et courants transitoires mesurés dans les postes à isolation gazeuse (GIS) montrent des composantes fréquentielles qui sont entre quelques MHz et environ 100 MHz, et que les tensions et courants transitoires qui se trouvent le conduit du GIB sont maintenus pendant plus de quelques microsecondes. Ce phénomène ne peut pas être reproduit par la méthode TL classique. Ensuite, des études approfondies sont menées sur des transitoires très rapides (VFT) dans un 500 kV GIS en adoptant la méthode TL étendue. Les VFT simulations s'effectuent sur le modèle large bande (WB) de l'effet de dépendance en fréquence dans le Programme de Transitoire Électromagnétique (EMTP). Les effets de divers paramètres du GIS sur le VFT, par exemple la longueur et la mise à la terre du conduit, sont explorés. Ensuite, une analyse de la foudre sur une ligne aérienne de distribution est étudiée avec le résultat d'un essai pratique. Enfin, l'excitation des modes de propagations d'un câble avec transposition du blindage avec la méthode TL étendue montrent plus d’amortissement et une convergence plus lisse vers un régime permanent que la méthode TL classique. Les formules proposées sont aussi validées avec les résultats d'essais pratiques sur un 110 kV câble avec transposition du blindage.

ABSTRACT

Electromagnetic transient (EMT) simulations in power systems have become an important tool for both research and practical applications. EMT-type simulation tools require overhead line/cable and underground cable models which are based on the calculation of series impedance and shunt admittance parameters. These parameters are calculated using the input of transmission system geometrical data and physical parameters. An important aspect in the calculations is formulation of earth-return impedance and admittance.

As a first step in this thesis, new and generalized earth-return impedance and admittance formulas of overhead lines and underground cables are derived based on Maxwell equations with complete initial and boundary conditions. Also, the complete electromagnetic field components radiated by the overhead line and the underground cable are derived. In order to avoid numerical difficulties in the complete field solution, the earth-return impedance and admittance formulas are simplified by adopting the appropriate assumptions. Moreover, approximate earth-return impedance and admittance formulas for the underground cable are proposed. Those formulas can be easily calculated because no Sommerfeld integral is involved. In addition, existing formulas such as Pollaczek's and Carson's earth-return impedance formulas are easily deduced from the proposed generalized formulation under the conditions adopted by Pollaczek and Carson. A modified earth-return Green function of Method of Moment (MoM) - Surface Admittance Operator (SO) for overhead lines and cables is also derived. The numerical stability of MoM-SO for overhead lines and cables can be improved by adopting derived earth-return Green function.

Next, the concept of an extended transmission line (TL) approach is proposed in comparison with the classical TL approach. By adopting the extended TL approach, the characteristics of frequency responses of overhead lines, overhead cables and underground cables show significant improvements and impacts in high frequencies. As it is well-known, an overhead line and an overhead cable involve mode transition from a low frequency earth-return wave to a high frequency surface wave. The lower attenuation of the surface wave shows a significant difference in the propagation functions evaluated by the classical TL approach. Also, wave propagation characteristics of an underground cable are evaluated by the extended TL approach. The influences of earth parameters such as earth resistivity and permittivity are clarified for the wave propagation characteristics in frequency domain.

Further to the frequency domain analysis, transient simulations in time domain by adopting the extended TL approach are also performed for different power system applications. First of all, a spike-like voltage at the wave-front of a step response in time domain is observed for a simple gas-insulated bus (GIB) because of the lower attenuation in the high frequency region. This phenomenon explains the reason why measured transient voltages and currents in gas-insulated substations (GISs) show frequency components ranging from some MHz to about 100 MHz, and the transient voltages and currents along the GIB pipe are sustained for more than a few microseconds. This phenomenon cannot be reproduced by the classical TL approach. Then, this thesis performs thorough investigations of very fast transients (VFTs) in a 500 kV GIS by adopting the extended TL approach. VFT simulations are performed by the wide-band (WB) model of the frequency-dependent effect in the Electromagnetic Transients Program (EMTP). The effects of various GIS parameters such as length and pipe grounding on the VFTs are investigated. Also, a lightning surge analysis on an overhead distribution line is investigated together with a field test result. Finally, energization of propagation modes and a cross-bonded cable with the extended TL approach show more damping and smooth convergence to steady-state in comparison with the classical TL approach. The proposed formulas are also validated with a field test on a 110 kV cross-bonded cable.

TABLE OF CONTENTS

LIST OF TABLES

LIST OF FIGURES

LIST OF SYMBOLS AND ABBREVIATIONS

$\mathbf{A}$	Voltage transformation matrix
α	Attenuation constant
$\mathbf{B}$	Current transformation matrix
β	Phase constant
c	Phase velocity
CB	Circuit breaker
CP	Constant parameter
DS	Disconnector
ECC	Earth continuity cable
EMT	Electromagnetic transient
EMI	Electromagnetic interference
EMTP	Electromagnetic transients programs
$\bar{\mathbf{F}}$	Vector field
FEM	Finite element method
FW	Fast wave
GIB	Gas-insulated bus
GIS	Gas-insulated substation
LCP	Line / cable parameters
MoM	Method of moment
NLT	Numerical Laplace transform
$\underline{\mathbf{P}}_{\mathbf{e}}$	Earth-return potential coefficient matrix based on quasi-TEM assumption
SA	Surface attach
SO	Surface admittance operator

SVL	Surge voltage limiter
TE	Transverse electric
TEM	Transverse electromagnetic
TL	Transmission line
TM	Transverse magnetic
VFT	Very fast transient
WB	Wide-band
$\mathbf{Y}_e$	Earth-return admittance matrix based on complete field solution
$\mathbf{Z}_e$	Earth-return impedance matrix based on complete field solution
$\underline{\mathbf{Z}}_e$	Earth-return impedance matrix based on quasi-TEM assumption
3D	3 dimensions

LIST OF APPENDICES

CHAPTER 1 INTRODUCTION

1.1 Motivation

The Electromagnetic Transients Program (EMTP) [1], [2] has been widely accepted and used all over the world as a standard and powerful simulation tool for studies and research on power system issues. The studies of electromagnetic transients are the most difficult and complicated ones. Because the EMT-type simulation tool is based on circuit theories, it requires the circuit parameters to perform simulations. Among various parameters, the series impedance and shunt admittance play an important role in the steady-state and transient phenomena on an overhead line, an overhead cable and an underground cable.

The generalized impedance and admittance formulas were found in [3]-[5] (Ametani) and implemented into the EMTP subroutine called Cable Constants in 1976. The Cable Constants are still widely used to calculate the parameters of overhead lines and underground cables in EMTP [1], [2].

In the documented formulas [3], the earth-return parameters are important. The derivation of earth-return impedance formulas for an overhead line started in 1920 [6], [7] (Carson and Pollaczek formulas). Although their approaches involved some inaccurate initial assumptions of fields [8], their formulas have been used since 1930. Because of the publications of Carson and Pollaczek, a number of different and improved methods have been developed, but some adopted Carson's and Pollaczek's initial assumptions, and are regarded as Carson's or Pollaczek's corrections [9]-[16].

In [17], [18] (Wise) modified the uniform current and field assumptions [8] from Carson and Pollaczek, and more generalized earth-return impedance and admittance of an overhead line above a homogenous earth were introduced. The homogenous earth model was further improved by [19]-[21] (Nakagawa), [22] (Ametani) and recently by [23], [24], (Papadopoulos) who also extended the formulas of earth-return impedance and admittance for the earth configurations consisting of several horizontal layers with different electromagnetic characteristics. The calculated results and performances of different electromagnetic characteristics of earth were discussed by [25]-[27].

The aforementioned methods only considered the axial electric field in the formulations. An attempt to find exact solutions of the problem was proposed by [28], [29] (Kikuchi). In [30]-[32]

(Wait) extended Kikuchi's work by adopting the method of complete Hertzian vector. Other attempts of complete field solutions of an overhead line were found by [8] (Olsen) and [33], [34] (Bridges) with the same method of [30]-[32]. In [35]-[39], it proposed different approaches in which the formulation of earth-return impedance and admittance are based on the vertical electric field and voltage propagation equation.

Propagation characteristics of an overhead line were also investigated and discussed in [28], [29]. In [28], [29], it pointed out that the wave propagation along an overhead line showed a transition between quasi-transverse electromagnetic (TEM) mode and transverse magnetic (TM) or transverse electric (TE) surface wave mode in a high frequency, and it was named Sommerfeld-Goubau propagation [28], [29]. For a clarity of definition, it has [28], [29]:

- TEM mode: neither electric nor magnetic field in the direction of wave propagation.
- TE mode: no electric field in the direction of wave propagation.
- TM mode: no magnetic field in the direction of wave propagation.

Recently, in [26], it further discussed the effect of earth-return admittance of overhead lines. A more general propagation characteristic was proposed by [40], [41] (Olsen) and [42] (Kuester) for investigations of a full frequency spectrum propagation of an overhead line. In general, the totally excited current on a conductor due to a finite source consists of a sum of discrete propagation modes or guided wave modes as well as a contribution from continuous propagation modes or radiation modes. Two different discrete roots can be extracted from the evaluation of a complete form of the propagation constant by Newton-Raphson's method [37]. One of the roots represents the transmission line (TL) mode, and it is associated with quasi-TEM mode. The TL mode reduces to the pure TEM mode of a conductor over a perfectly conducting earth. Another one is named fast wave (FW) mode or surface attached (SA) mode which is supported by the air-earth interface and can be related to the Zenneck surface wave. It should be noted that the TL mode is characterized by a smaller attenuation constant than the FW mode in a high frequency.

In [7] (Pollaczek), a formula of the earth-return impedance for an underground cable is also developed. The extended expression of Pollaczek's formula is proposed in [9], [14]-[16], [43]-[46]. Some simplified closed-form approximation for the formulas in [7] and [43] are made and

summarized in [47]-[50]. Also, references [51]-[53] tried to revise the numerical instability by adopting different numerical methods.

In [54], [55] (Wait) and [56], [57] (Bridges) derived the complete field solutions of an underground cable which buried in a homogenous earth. The formulas of the earth-return impedance and admittance were deduced from the axial electric field with the impedance boundary condition at the outer radius of cable. Recently, lightning induced voltages are studied on an underground cable [58] by adopting the formulas based on reference [44]. Also, another quasi-TEM based earth-return admittance formula is derived in [59], [60], however the formula relies on the earth surface as the reference of the line voltage integral [59], [60].

It is crucial to recognize that a thin wire approximation is made for all the above methods. This assumption means that the carried current of a conductor is assumed to be only the axial direction of waveguide and uniformly distributed around the circumference of the conductor. Under this approximation, the current can be regarded as a filamentary current and located at the center of the conductor [61].

Except the analytical methods discussed above, the numerical electromagnetic analysis [62]-[70] is another approach for the calculations of parameters of lines and cables.

This thesis emphasizes the derivation of new and generalized earth-return impedance and admittance formulas of an overhead line, an overhead cable and an underground cable. The derived analytical formulas and Method of Moment (MoM) - Surface Admittance Operator (SA) method [64]-[67] are compared to each other. Also, the frequency and transient responses of different power system applications by adopting the newly derived formulas are investigated.

1.2 Thesis outline

This thesis is composed of six chapters and two appendices.

- CHAPTER 1 INTRODUCTION

This chapter introduces the motivation of this Ph.D. work, highlights its contributions, publications and summarizes the contents of each chapter.

- CHAPTER 2 DERIVATION OF ELECTROMAGNETIC FIELD EQUATIONS AND EARTH-RETURN PARAMETERS FOR AN OVERHEAD LINE

The essential formulations of electromagnetic field components and the earth-return impedance and admittance of an overhead line with N conductors are proposed and derived in this chapter. The discussion of existing formulas is also included. A modified earth-return Green function is derived to eliminate the numerical instability of MoM-SO for an overhead line and cable.

- CHAPTER 3 DERIVATION OF ELECTROMAGNETIC FIELD EQUATIONS AND EARTH-RETURN PARAMETERS FOR AN UNDERGROUND CABLE

It presents the essential formulations of electromagnetic field components and the earth-return impedance and admittance of a multi-phase underground cable. It shows approximate earth-return impedance and admittance formulas. Also, the drawbacks of existing formulas are made clear in comparison with the derived complete formulas.

- CHAPTER 4 WAVE PROPAGATION IN FREQUENCY DOMAIN

This chapter explains the details of extended TL and classical TL approaches. It contains the calculations of wave propagation characteristics in frequency domain for an overhead line, an overhead cable and an underground cable.

- CHAPTER 5 TRANSIENT SIMULATIONS IN TIME DOMAIN

The transient simulations in time domain of different power system applications by adopting the extended and classical TL approaches presented in Chapter 4 are studied and investigated.

- CHAPTER 6 CONCLUSIONS

It presents the main conclusions of this thesis and future works.

- APPENDIX A

It summarizes Sommerfeld integrals used in Chapter 2 and Chapter 3.

- APPENDIX B

It shows the list of publications.

1.3 Contributions

The main research achievements and contributions are summarized here.

- Derivation of new and generalized earth-return impedance / admittance formulas for an underground cable

New and generalized formulas of the earth-return impedance and admittance on an underground cable based on the complete field solution are derived. Differences of wave propagation and surge characteristics calculated by the newly proposed formulas and existing formulas implemented in EMTP are investigated. It is made clear that the complete formulas of impedance and admittance should be adopted especially when studying high-frequency phenomena. Also, the proposed impedance formula is verified in comparison with computed results by MoM-SO method.

- Time responses of an overhead cable due to mode transition from TEM to TM or TE propagation

It is known that wave propagation on an overhead conductor shows mode transition from a TEM mode at low frequencies to TM or TE modes at higher frequencies and finally reaches the so-called Sommerfeld-Goubau (surface wave) propagation with lower attenuation than that of the TEM mode [26], [28], [29]. The lower attenuation is estimated to influence significantly transient responses in time domain. However, all the previous studies were carried out in frequency domain. Thus, the basic characteristics of time domain responses considering mode transition which have not been studied in the past are investigated. The step response and switching surges of an overhead cable are calculated by using numerical Laplace transform (NLT) [71]-[73] and wide-band (WB) model in EMTP [1], [74].

- Mode transition of an overhead conductor from the viewpoint of the axial electric field

This work investigates the frequency responses of electric and magnetic fields by deriving the formulas based on the complete field solutions in comparison with the formulas derived using the Carson or Pollaczek's approach [6], [7]. Specifically, the correlation between the axial electric field and the attenuation constant is confirmed and validated in the mode transition area.

- Electromagnetic disturbances in gas-insulated substation (GIS) and very fast transient (VFT) calculations

VFTs are produced in a GIS during switching operation of a disconnector (DS) or a circuit breaker (CB) [75]-[77]. Because of very high frequency components, the VFTs in the GISs can cause electromagnetic interference (EMI) such as malfunctions in control circuits of the GISs [78]-[84].

In this work, modelling of GIS elements by the extended TL approach is explained. Also, the sensitive analysis of GIS parameters in VFT calculations are investigated.

- New cable parameters code

The newly produced cable parameters code can deal with the series impedance and shunt admittance for overhead cables, underground cables and overhead-underground cables above or buried in up to five layers of stratified earth.

CHAPTER 2 DERIVATION OF ELECTROMAGNETIC FIELD EQUATIONS AND EARTH-RETURN PARAMETERS FOR AN OVERHEAD LINE

In this chapter, formulas of the complete electromagnetic field solutions on an overhead line with N conductors are derived based on rigorous Maxwell equations. The derived formulas of electromagnetic fields are applied to formulate a generalized earth-return impedance and admittance on the multi-phase overhead line. Existing formulas of the earth-return impedance and admittance are discussed in comparison with the derived formulas. Finally, a modified earth-return Green function is derived and it is used for the recently developed software called MoM-SO [64]-[67]. By adopting the newly derived Green function, MoM-SO becomes able to generate accurate parameters of overhead lines within TEM mode of wave propagation, and the numerical instability observed in the original MoM-SO is eliminated [66], [67].

2.1 Derivation of electromagnetic field formulas

An overhead line with N conductors is located above a homogenous earth, as illustrated in Figure 2.1.

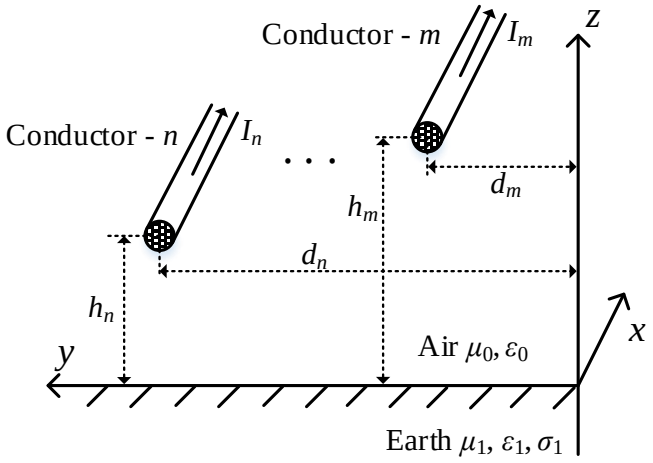

Figure 2.1: Configuration of an overhead line with *N* conductors above a homogenous earth

The air is the medium in the region $z > 0$, and characterized by permeability μ_0 and permittivity ε_0. The region of $z < 0$ is the lossy earth, and it is characterized by permeability μ_1, permittivity

ε_1 and conductivity σ_1. It is assumed that the radius of each conductor is small compared with the height and separation. Thus, a filament current approximation can be adopted where all the conductor currents are only expressed by the axial component [35].

There exists as many propagation modes as the number of conductors in the system [35]. The conductor - m with radius r_m carries the following current in phase domain [38].

$$I_m(x) = \sum_{v=1}^{N} B_{mv} i_v(x) \tag{2.1}$$

where B_{mv} is the mv-th element of the $N \times N$ unknown current transformation matrix $\mathbf{B}$ (to be determined by impedance boundary condition) and the v-th modal current $i_v(x)$ is defined by:

$$i_v(x) = i_{vp} e^{-jk_v x} \tag{2.2}$$

where i_{vp} is the amplitude of the modal current and k_v is the unknown wave number of the v-th mode.

The electromagnetic vector fields can be defined by using Hertz vectors as [85]:

$$\overline{\mathbf{E}} = \nabla\nabla\cdot\overline{\mathbf{\Pi}}_{\mathbf{E}} + \omega^2\mu\varepsilon\overline{\mathbf{\Pi}}_{\mathbf{E}} - j\omega\mu\nabla\times\overline{\mathbf{\Pi}}_{\mathbf{M}} \tag{2.3}$$

$$\overline{\mathbf{H}} = \nabla\nabla\cdot\overline{\mathbf{\Pi}}_{\mathbf{M}} + \omega^2\mu\varepsilon\overline{\mathbf{\Pi}}_{\mathbf{M}} + j\omega\varepsilon\nabla\times\overline{\mathbf{\Pi}}_{\mathbf{E}} \tag{2.4}$$

where ω is angular frequency.

$\overline{\mathbf{\Pi}}_{\mathbf{E}}$ and $\overline{\mathbf{\Pi}}_{\mathbf{M}}$ are electric and magnetic Hertz vectors. It should be noted that any continuously differentiable vector field is define by:

$$\overline{\mathbf{F}} = \mathbf{e}_{\mathbf{x}} F_x + \mathbf{e}_{\mathbf{y}} F_y + \mathbf{e}_{\mathbf{z}} F_z \tag{2.5}$$

where $\mathbf{e}_{\mathbf{x}}$, $\mathbf{e}_{\mathbf{y}}$ and $\mathbf{e}_{\mathbf{z}}$ be the corresponding basis of unit vector $\mathbf{e}$.

For the present problem, it is convenient to adopt only x-component of Hertz vectors because $\overline{\mathbf{\Pi}}_{\mathbf{E}}$ and $\overline{\mathbf{\Pi}}_{\mathbf{M}}$ are generated by $I_m(x)$ and will be directed parallel to the x-axis [35], [37].

Thus, the expressions of the *x*-component of the electric and magnetic Hertz vectors at any point in the air ("0") and earth ("1") can be derived as a sum of contributions by the current in each conductor [38]. By adopting the superposition theorem, it gives:

$$\Pi_{0E}\left(x,y,z\right)=\sum_{m=1}^{N}\Pi_{0Em}\left(x,y,z\right) \tag{2.6}$$

$$\Pi_{0M}\left(x,y,z\right)=\sum_{m=1}^{N}\Pi_{0Mm}\left(x,y,z\right) \tag{2.7}$$

$$\Pi_{1E}\left(x,y,z\right)=\sum_{m=1}^{N}\Pi_{1Em}\left(x,y,z\right) \tag{2.8}$$

$$\Pi_{1M}\left(x,y,z\right)=\sum_{m=1}^{N}\Pi_{1Mm}\left(x,y,z\right) \tag{2.9}$$

where $\Pi_{0Em}\left(x,y,z\right)$, $\Pi_{0Mm}\left(x,y,z\right)$, $\Pi_{1Em}\left(x,y,z\right)$ and $\Pi_{1Mm}\left(x,y,z\right)$ are the *x*-components of electric and magnetic Hertz vectors in the air and earth, generated by the current $I_m\left(x\right)$ of the *m*-th cable.

By adopting the formulas of Hertz vectors [30] into (2.6) to (2.9), the following formulas are deduced.

$$\Pi_{0E}\left(x,y,z\right)=-\frac{j\omega\mu_0}{4\pi k_a^2}\sum_{m=1}^{N}\sum_{v=1}^{N}B_{mv}i_v\left(x\right)\int_{-\infty}^{+\infty}\frac{e^{-\left|z-h_m\right|u_{0v}}+R_{Ev}e^{-\left(z+h_m\right)u_{0v}}}{u_{0v}}e^{-j\left(y-d_m\right)\lambda}d\lambda \tag{2.10}$$

$$\Pi_{0M}\left(x,y,z\right)=-\frac{j\omega\mu_0}{4\pi k_a^2}\sum_{m=1}^{N}\sum_{v=1}^{N}B_{mv}i_v\left(x\right)\int_{-\infty}^{+\infty}\frac{R_{Mv}e^{-\left(z+h_m\right)u_{0v}}}{u_{0v}}e^{-j\left(y-d_m\right)\lambda}d\lambda \tag{2.11}$$

$$\Pi_{1E}\left(x,y,z\right)=-\frac{j\omega\mu_0}{4\pi k_a^2}\sum_{m=1}^{N}\sum_{v=1}^{N}B_{mv}i_v\left(x\right)\int_{-\infty}^{+\infty}\frac{T_{Ev}e^{zu_{1v}-h_mu_{0v}}}{u_{0v}}e^{-j\left(y-d_m\right)\lambda}d\lambda \tag{2.12}$$

$$\Pi_{1M}\left(x,y,z\right)=-\frac{j\omega\mu_0}{4\pi k_a^2}\sum_{m=1}^{N}\sum_{v=1}^{N}B_{mv}i_v\left(x\right)\int_{-\infty}^{+\infty}\frac{T_{Mv}e^{zu_{1v}-h_mu_{0v}}}{u_{0v}}e^{-j\left(y-d_m\right)\lambda}d\lambda \tag{2.13}$$

where λ is integral variable and

$$u_{0v} = \sqrt{\lambda^2 + k_v^2 - k_a^2}\ ,\ u_{1v} = \sqrt{\lambda^2 + k_v^2 - k_e^2} \tag{2.14}$$

with

$$k_a^2 = -j\omega\mu_0 j\omega\varepsilon_0\ ,\ k_e^2 = -j\omega\mu_1\left(\sigma_1 + j\omega\varepsilon_1\right) \tag{2.15}$$

The irrationals R_{Ev}, R_{Mv}, T_{Ev} and T_{Mv} are derived by adopting the following boundary conditions [30] at the air / earth interface ($z = 0$), referred to the *v*-th mode.

$$\left.\begin{aligned} E_{0x} &= E_{1x} \\ E_{0y} &= E_{1y} \\ H_{0x} &= H_{1x} \\ H_{0y} &= H_{1y} \end{aligned}\right\} \tag{2.16}$$

where E_x, E_y, H_x and H_y are axial and horizontal electric and magnetic field components.

Substituting (2.10) to (2.13) into (2.16) and assuming $\mu_1 = \mu_0$, R_{Ev} and R_{Mv} can be deduced.

$$R_{Ev} = -1 + 2\frac{k_a^2 u_{0v}}{k_a^2 - k_v^2}\left(\frac{1}{u_{0v} + u_{1v}} - \frac{k_v^2}{k_e^2 u_{0v} + k_a^2 u_{1v}}\right) \tag{2.17}$$

$$R_{Mv} = -2\frac{k_a^2 k_v \lambda}{j\omega\mu_0\left(k_a^2 - k_v^2\right)}\left(\frac{1}{u_{0v} + u_{1v}} - \frac{k_a^2}{k_e^2 u_{0v} + k_a^2 u_{1v}}\right) \tag{2.18}$$

By adopting (2.17) and (2.18) into (2.10) and (2.11), and solving (2.3) and (2.4), the formulas of electromagnetic field components at an arbitrary point in the air are derived.

$$E_{0x}\left(x, y, z\right) = \sum_{m=1}^{N}\sum_{v=1}^{N}\Lambda_{0x}\left(y, z, d_m, h_m, v\right)B_{mv}i_v\left(x\right) \tag{2.19}$$

$$E_{0y}\left(x, y, z\right) = \sum_{m=1}^{N}\sum_{v=1}^{N}\Lambda_{0y}\left(y, z, d_m, h_m, v\right)B_{mv}i_v\left(x\right) \tag{2.20}$$

$$E_{0z}\left(x, y, z\right) = \sum_{m=1}^{N}\sum_{v=1}^{N}\Lambda_{0z}\left(y, z, d_m, h_m, v\right)B_{mv}i_v\left(x\right) \tag{2.21}$$

$$H_{0x}\left(x, y, z\right) = \sum_{m=1}^{N}\sum_{v=1}^{N}\Psi_{0x}\left(y, z, d_m, h_m, v\right)B_{mv}i_v\left(x\right) \tag{2.22}$$

$$H_{0y}(x,y,z)=\sum_{m=1}^{N}\sum_{v=1}^{N}\Psi_{0y}(y,z,d_m,h_m,v)B_{mv}i_v(x) \tag{2.23}$$

$$H_{0z}(x,y,z)=\sum_{m=1}^{N}\sum_{v=1}^{N}\Psi_{0z}(y,z,d_m,h_m,v)B_{mv}i_v(x) \tag{2.24}$$

where $E_z(x,y,z)$ and $H_z(x,y,z)$ are vertical electric and magnetic field components. The kernel functions $\Lambda_{0x}(y,z,d_m,h_m,v)$, $\Lambda_{0y}(y,z,d_m,h_m,v)$, $\Lambda_{0z}(y,z,d_m,h_m,v)$, $\Psi_{0x}(y,z,d_m,h_m,v)$, $\Psi_{0y}(y,z,d_m,h_m,v)$ and $\Psi_{0z}(y,z,d_m,h_m,v)$ are given in Appendix A.1.

Equations (2.19) to (2.24) can be rewritten into matrix expressions as a function of the exciting modal currents.

$$\begin{bmatrix}E_{0x}(x,y,z)\\E_{0y}(x,y,z)\\E_{0z}(x,y,z)\end{bmatrix}=\begin{bmatrix}\Phi_{0x}(y,z,d_m,h_m,1) & \cdots & \Phi_{0x}(y,z,d_m,h_m,N)\\\Phi_{0y}(y,z,d_m,h_m,1) & \cdots & \Phi_{0y}(y,z,d_m,h_m,N)\\\Phi_{0z}(y,z,d_m,h_m,1) & \cdots & \Phi_{0z}(y,z,d_m,h_m,N)\end{bmatrix}\begin{bmatrix}i_1(x)\\\vdots\\i_N(x)\end{bmatrix} \tag{2.25}$$

$$\begin{bmatrix}H_{0x}(x,y,z)\\H_{0y}(x,y,z)\\H_{0z}(x,y,z)\end{bmatrix}=\begin{bmatrix}\Upsilon_{0x}(y,z,d_m,h_m,1) & \cdots & \Upsilon_{0x}(y,z,d_m,h_m,N)\\\Upsilon_{0y}(y,z,d_m,h_m,1) & \cdots & \Upsilon_{0y}(y,z,d_m,h_m,N)\\\Upsilon_{0z}(y,z,d_m,h_m,1) & \cdots & \Upsilon_{0z}(y,z,d_m,h_m,N)\end{bmatrix}\begin{bmatrix}i_1(x)\\\vdots\\i_N(x)\end{bmatrix} \tag{2.26}$$

where

$$\Phi_{0x}(y,z,d_m,h_m,v)=\sum_{m=1}^{N}\Lambda_{0x}(y,z,d_m,h_m,v)B_{mv} \tag{2.27}$$

$$\Phi_{0y}(y,z,d_m,h_m,v)=\sum_{m=1}^{N}\Lambda_{0y}(y,z,d_m,h_m,v)B_{mv} \tag{2.28}$$

$$\Phi_{0z}(y,z,d_m,h_m,v)=\sum_{m=1}^{N}\Lambda_{0z}(y,z,d_m,h_m,v)B_{mv} \tag{2.29}$$

$$\Upsilon_{0x}(y,z,d_m,h_m,v)=\sum_{m=1}^{N}\Psi_{0x}(y,z,d_m,h_m,v)B_{mv} \tag{2.30}$$

$$\Upsilon_{0y}(y,z,d_m,h_m,v)=\sum_{m=1}^{N}\Psi_{0y}(y,z,d_m,h_m,v)B_{mv} \tag{2.31}$$

$$\Upsilon_{0z}\left(y,z,d_m,h_m,v\right)=\sum_{m=1}^{N}\Psi_{0z}\left(y,z,d_m,h_m,v\right)B_{mv} \tag{2.32}$$

The matrices expressions (2.25) and (2.26) describing the electromagnetic field components can be also represented in the following compact forms.

$$\left.\begin{aligned}\mathbf{E}_0&=\mathbf{\Phi}_0\mathbf{i}\\ \mathbf{H}_0&=\mathbf{\Upsilon}_0\mathbf{i}\end{aligned}\right\} \tag{2.33}$$

where $\mathbf{E}_0$ and $\mathbf{H}_0$ are $N\times1$ electromagnetic field vectors, $\mathbf{\Phi}_0$ and $\mathbf{\Upsilon}_0$ are $3\times N$ modal current to field operator's matrices, and $\mathbf{i}$ is an $N\times1$ modal current vector.

It should be noted that (2.33) derived in the above is based on the assumption of unidirectional propagation of voltage and current waves. The responses of electromagnetic fields should be related to the exciting sources which are impressed by the transmitting device. Thus, the transfer function from voltage to field can be defined by using $\mathbf{\Phi}_0$ and $\mathbf{\Upsilon}_0$ matrices together with the following modal current vector [4], [5]:

$$\mathbf{i}=\mathbf{B}^{-1}\mathbf{Y}_0\mathbf{A}\zeta\mathbf{A}^{-1}\mathbf{V_f} \tag{2.34}$$

where $\mathbf{Y}_0$ is an $N\times N$ characteristic admittance matrix of an overhead line in phase domain, $\mathbf{A}$ is an $N\times N$ voltage transformation matrix, ζ is an $N\times N$ reflection free transition diagonal matrix, $\mathbf{V_f}$ is an $N\times1$ impressed voltage source vector, and

$$\mathbf{A}=\left(\mathbf{B}^{T}\right)^{-1} \tag{2.35}$$

$$\zeta=\mathrm{diag}\left(e^{-jk_v x}\right) \tag{2.36}$$

Equation (2.33) can be rewritten by replacing $\mathbf{i}$ by (2.34):

$$\left.\begin{aligned}\mathbf{E}_0&=\mathbf{\Phi}_0\mathbf{B}^{-1}\mathbf{Y}_0\mathbf{A}\zeta\mathbf{A}^{-1}\mathbf{V_f}\\ \mathbf{H}_0&=\mathbf{\Upsilon}_0\mathbf{B}^{-1}\mathbf{Y}_0\mathbf{A}\zeta\mathbf{A}^{-1}\mathbf{V_f}\end{aligned}\right\} \tag{2.37}$$

Therefore, the radiated electromagnetic fields of a multi-phase overhead line can be calculated by applying the impressed voltage source $\mathbf{V_f}$ in (2.37).

2.2 Derivation of generalized earth-return impedance and admittance formulas

In this section, the generalized earth-return impedance and admittance formulas are derived based on the electromagnetic field components in Section 2.1. Then, the derived formulas are discussed in comparison with existing formulas.

2.2.1 Complete field solution

The same configuration of an overhead line with N conductors illustrated in Figure 2.1 is considered. The continuity of axial electric field must be fulfilled at the air / conductor interface for each conductor in the configuration. The *x*-component of electric field along the *n*-th overhead conductor can be expressed by:

$$E_{xn}(x) = \sum_{v=1}^{N} Z_{sn}(r_n, v) B_{nv} i_v(x) : \; n = 1, \cdots, N \tag{2.38}$$

where r_n is the radius of the *n*-th conductor, B_{nv} is the *nv*-th element of $\mathbf{B}$, and $Z_{sn}(r_n, v)$ is the surface impedance of the *n*-th conductor for the *v*-th mode [3].

By adopting the impedance boundary condition into (2.19) and (2.38), the continuity gives

$$\sum_{v=1}^{N} Z_{sn}(r_n, v) B_{nv} i_v(x) = \sum_{m=1}^{N} \sum_{v=1}^{N} \Lambda_{0x}(d_n, h_n, d_m, h_m, v) B_{mv} i_v(x) \tag{2.39}$$

In the evaluation of the right side of (2.39), the self-element, $n = m$, is calculated at the surface of conductor. The mutual element, $n \neq m$, can be calculated at the center of two conductors. When $N = 1$, (2.39) becomes the same as the exact approach in reference [31].

Equation (2.39) can be rewritten in the following matrix expression based on an eigenvalue analysis [4].

$$\mathbf{P^r B_v} = -k_v^2 \mathbf{B_v} \tag{2.40}$$

where vector $\mathbf{B_v}$ is related to the *v*-th column of $\mathbf{B}$ and $N \times N$ matrix $\mathbf{P^r}$ is defined by:

$$\mathbf{P^r} = \left(\mathbf{P_2^r}\right)^{-1} \mathbf{P_1^r} \tag{2.41}$$

where

$$\mathbf{P}_1^{\mathbf{r}} = \mathbf{Z}_{\mathbf{s}} + \frac{j\omega\mu_0}{4\pi}\left(\underline{\mathbf{\Delta}}_1 + 2\underline{\mathbf{S}}_1\right),\ \mathbf{P}_2^{\mathbf{r}} = \frac{1}{4\pi\, j\omega\varepsilon_0}\left(\underline{\mathbf{\Delta}}_1 + 2\underline{\mathbf{S}}_2\right) \tag{2.42}$$

$\mathbf{Z}_{\mathbf{s}}$ is an $N \times N$ surface impedance diagonal matrix and its each element is given in (2.38), $\underline{\mathbf{\Delta}}_1$, $\underline{\mathbf{S}}_1$ and $\underline{\mathbf{S}}_2$ are $N \times N$ matrices and its each element is given in (2.39) together with (A.7), (A.11) and (A.12).

It is clear that (2.41) represents the nature of the series impedance and shunt admittance of a multi-phase overhead line, and the earth-return impedance and admittance matrices can be extracted from (2.41).

$$\mathbf{Z}_{\mathbf{e}} = \frac{j\omega\mu_0}{4\pi}\left(\underline{\mathbf{\Delta}}_1 + 2\underline{\mathbf{S}}_1\right),\quad \mathbf{Y}_{\mathbf{e}} = \left(\mathbf{P}_2^{\mathbf{r}}\right)^{-1} \tag{2.43}$$

It should be noted that each element of (2.43) is also the function of unknown wave number k_v.

2.2.2 Quasi-TEM solution

When a single overhead line ($N = 1$) is considered, the solution of k_v can be performed by Newton-Raphson method in (2.40). Then, (2.43) can be calculated with k_v and the configuration of the overhead line without any difficulty. However, a multi-phase overhead line creates heavy mathematical challenges to accurately calculate each modal k_v in (2.40). Because each element of $\mathbf{P}^{\mathbf{r}}$ involves k_v and nonlinear Sommerfeld integrals. Therefore, in order to avoid such numerical infeasibility, the quasi-TEM assumption $k_v \approx k_a$ [8] is used and adopted into (2.43). Then, the earth-return impedance and admittance formulas can be significantly simplified and rewritten based on references [31], [33], [34].

$$\underline{Z}_{e(nm)}\left(d_n, h_n, d_m, h_m\right) = \frac{j\omega\mu_0}{2\pi}\left\{\ln\left[\frac{D_{nm}\left(d_n, h_n, d_m, h_m\right)}{d_{nm}\left(d_n, h_n, d_m, h_m\right)}\right] + 2\underline{\underline{S}}_1\left(d_n, h_n, d_m, h_m\right)\right\} \tag{2.44}$$

$$\underline{P}_{e(nm)}\left(d_n, h_n, d_m, h_m\right) = \frac{1}{2\pi\varepsilon_0}\left\{\ln\left[\frac{D_{nm}\left(d_n, h_n, d_m, h_m\right)}{d_{nm}\left(d_n, h_n, d_m, h_m\right)}\right] + 2\underline{\underline{S}}_2\left(d_n, h_n, d_m, h_m\right)\right\} \tag{2.45}$$

where $\underline{Z}_{e(nm)}(d_n, h_n, d_m, h_m)$ and $\underline{P}_{e(nm)}(d_n, h_n, d_m, h_m)$ are the earth-return impedance and potential coefficient based on quasi-TEM assumption between conductors n and m. $\underline{\underline{S}}_1(y, z, d_m, h_m)$ and $\underline{\underline{S}}_2(y, z, d_m, h_m)$ are Sommerfeld integrals $\underline{S}_1(y, z, d_m, h_m, v)$ and $\underline{S}_2(y, z, d_m, h_m, v)$ based on the quasi-TEM assumption and are given by:

$$\underline{\underline{S}}_1(y, z, d_m, h_m) = \int_0^{+\infty} \frac{e^{-(z+h_m)\lambda}}{\lambda + \sqrt{\lambda^2 + k_a^2 - k_e^2}} \cos\left[(y - d_m)\lambda\right] d\lambda \tag{2.46}$$

$$\underline{\underline{S}}_2(y, z, d_m, h_m) = \int_0^{+\infty} \frac{e^{-(z+h_m)\lambda}}{k_e^2 k_a^{-2}\lambda + \sqrt{\lambda^2 + k_a^2 - k_e^2}} \cos\left[(y - d_m)\lambda\right] d\lambda \tag{2.47}$$

$$d_{nm}(y, z, d_m, h_m) = \sqrt{(y - d_m)^2 + (z - h_m)^2} \tag{2.48}$$

$$D_{nm}(y, z, d_m, h_m) = \sqrt{(y - d_m)^2 + (z + h_m)^2} \tag{2.49}$$

The self-elements of (2.44) and (2.45) are calculated by adopting $h_n = h_m$ and $d_n - d_m = r_n$ / $d_n - d_m = r_m$. The mutual elements are calculated at the center of the two conductors.

2.2.3 Discussions

The earth-return impedance and space potential coefficient formulas derived in 1920s to 1930s are related to (2.44) and (2.45). If $k_a^2 = 0$, $\varepsilon_1 = 0$ and $\underline{\underline{S}}_2(y, z, d_m, h_m) = 0$ are assumed in (2.44) and (2.45), Carson's and Pollaczek's earth-return impedance and space potential coefficient formulas for a multi-phase overhead line are derived [6], [7].

$$\underline{Z}_{e(nm)}^{\text{Carson}}(d_n, h_n, d_m, h_m) = \frac{j\omega\mu_0}{2\pi}\left\{\ln\left[\frac{D_{nm}(d_n, h_n, d_m, h_m)}{d_{nm}(d_n, h_n, d_m, h_m)}\right] + 2\underline{\underline{S}}_1^{\text{Carson}}(d_n, h_n, d_m, h_m)\right\} \tag{2.50}$$

$$\underline{P}_{e(nm)}^{\text{Carson}}(d_n, h_n, d_m, h_m) = \frac{1}{2\pi\varepsilon_0}\ln\left[\frac{D_{nm}(d_n, h_n, d_m, h_m)}{d_{nm}(d_n, h_n, d_m, h_m)}\right] \tag{2.51}$$

where

$$\underline{\underline{S}}_1^{\text{Carson}}\left(y,z,d_m,h_m\right)=\int_0^{+\infty}\frac{e^{-\left(z+h_m\right)\lambda}}{\lambda+\sqrt{\lambda^2-k_e^2}}\cos\left[\left(y-d_m\right)\lambda\right]d\lambda \tag{2.52}$$

with

$$k_e^2=-j\omega\mu_0\sigma_1 \tag{2.53}$$

If (2.53) is replaced by $k_e^2=-j\omega\mu_0\left(\sigma_1+j\omega\varepsilon_1\right)$, (2.52) becomes identical to Sunde's earth-return impedance formula [9].

The Carson's and Pollaczek's earth-return impedance formulas neglect the intrinsic wave number of air and displacement currents in the earth. Although Sunde's formula includes the displacement current term, it is correct only in the case of earth relative permittivity of 2 [86]. Moreover, the lossy earth correction term $\underline{\underline{S}}_2\left(d_n,h_n,d_m,h_m\right)$ has been neglected in (2.51), and it leads to inaccurate wave propagation characteristics and transient simulations in high frequencies, i.e. $f >$ several MHz [8], [26].

Moreover, (2.43) covers the formulas derived by Bridges [33], [34]. By adopting $N=1$ into (2.39) and (2.43), Kikuchi's and Wait's earth-return impedance and admittance formulas can be obtained [28]-[32]. As already explained in Section 2.2.2, the complete field solution requires the numerical results of k_v to calculate the earth-return impedance and admittance. Thus, the quasi-TEM assumption $k_v\approx k_a$ can be adopted in (2.43) to simplify the calculation procedure. Then, (2.44) and (2.45) become the same as Wise's earth-return impedance and potential coefficient formulas [17], [18]. Also, Nakagawa, Ametani and Papadopoulos [19]-[24] extended (2.44) and (2.45) to consider the stratified earth.

Other earth-return impedance and admittance formulas based on the complete field solutions were derived by Olsen [8] with the same method of Wait [31]. Wedepohl [35], D'Amore [37], [38] and Pettersson [39] proposed different approaches, in which the formulations of the earth-return impedance and admittance are based on the vertical electric field, the voltage and current propagation equations.

2.3 Derivation of modified earth-return Green function for MoM-SO

Recently, MoM-SO has been proposed to calculate the frequency dependent series impedance of overhead lines and underground cables. It is based on the surface admittance operator combined with the method of moments [64]-[67]. The MoM-SO has several advantages for calculating the series impedance of the overhead lines and underground cables. For example, the skin and proximity effects of conductors can be considered. A stratified earth with arbitrary earth parameters (permeability, permittivity and conductivity) can be properly modeled. Also, arbitrary cable configurations, such as tunnel installed and submarine cables, can be handled. Furthermore, the MoM-SO provides much higher computational efficiency than a software based on the finite element method (FEM).

A numerical instability for overhead lines has been observed when using MoM-SO as described in references [66], [67]. Considering the above, a modified earth-return Green function for an overhead line with N conductors is derived in this section. The numerical instability inherent in the existing MoM-SO [66], [67] can be eliminated by adopting the newly derived Green function.

The configuration of an overhead line with N conductors illustrated in Figure 2.1 is used. Green function considering a lossy earth can be derived based on the electromagnetic field components in the air and earth [85].

$$\overline{\mathbf{E}} = -j\omega\overline{\mathbf{A}}_{\mathbf{M}} - j\frac{\nabla\nabla\cdot\overline{\mathbf{A}}_{\mathbf{M}}}{\omega\mu\varepsilon} - \frac{\nabla\times\overline{\mathbf{A}}_{\mathbf{E}}}{\varepsilon} \tag{2.54}$$

$$\overline{\mathbf{H}} = -j\omega\overline{\mathbf{A}}_{\mathbf{E}} - j\frac{\nabla\nabla\cdot\overline{\mathbf{A}}_{\mathbf{E}}}{\omega\mu\varepsilon} + \frac{\nabla\times\overline{\mathbf{A}}_{\mathbf{M}}}{\mu} \tag{2.55}$$

where $\overline{\mathbf{A}}_{\mathbf{M}}$ and $\overline{\mathbf{A}}_{\mathbf{E}}$ are vector magnetic and electric potentials and given by:

$$\overline{\mathbf{A}}_{\mathbf{M}} = j\omega\mu\varepsilon\overline{\mathbf{\Pi}}_{\mathbf{E}},\ \overline{\mathbf{A}}_{\mathbf{E}} = j\omega\mu\varepsilon\overline{\mathbf{\Pi}}_{\mathbf{M}} \tag{2.56}$$

where $\overline{\mathbf{\Pi}}_{\mathbf{E}}$ and $\overline{\mathbf{\Pi}}_{\mathbf{M}}$ are given in (2.3) and (2.4).

By adopting the same modal analysis in Section 2.1, the *x*-component of Green function in the air can be derived

$$G_{0x}(x,y,z) = \mathbf{\Phi}_{0x}^{G}\mathbf{B}^{-1}\mathbf{I} \tag{2.57}$$

where $\mathbf{B}$ is given in (2.1), $\mathbf{I}$ is an $N\times 1$ phase domain current vector and each element is defined in (2.1), and the 1v-th element of $1\times N$ vector $\mathbf{\Phi}_{0x}^{G}$ is given in (2.27).

The above is the same as the complete field solution in Sections 2.1 and 2.2. Equation (2.57) requires to find k_v and $\mathbf{B}$ as the first step. However, the quasi-TEM assumption $k_v \approx k_a$ and a uniform current assumption $k_v \approx 0$ [8] can be used to simplify (2.57). It should be noted that MoM-SO calculates only the series impedance matrix but not the admittance, and the second term of (A.1) (kernel function of (2.27)) can be neglected because it represents the earth-return admittance [31], [33]. Then, the Green function based on quasi-TEM assumption has:

$$\underline{G}_{0x}\left(x,y,z\right)=\underline{\mathbf{\Phi}}_{0x}^{G}\mathbf{I} \tag{2.58}$$

where $\mathbf{I}$ is given in (2.57) and the 1m-th element of $1\times N$ vector $\underline{\mathbf{\Phi}}_{0x}^{G}$ is:

$$\underline{\Phi}_{0x(1m)}^{G}\left(y,z,d_m,h_m\right)=-\frac{j\omega\mu_0}{2\pi}\left\{\ln\left[\frac{D_{nm}\left(y,z,d_m,h_m\right)}{d_{nm}\left(y,z,d_m,h_m\right)}\right]+2\underline{\underline{S}}_{1}\left(y,z,d_m,h_m\right)\right\} \tag{2.59}$$

where $\underline{\underline{S}}_{1}\left(y,z,d_m,h_m\right)$, $d_{nm}\left(y,z,d_m,h_m\right)$ and $D_{nm}\left(y,z,d_m,h_m\right)$ are given in (2.46), (2.48) and (2.49).

Green function based on the uniform current assumption gives the same expression as (2.58), but with different elements of $\underline{\mathbf{\Phi}}_{0x}^{G}$:

$$\begin{aligned}\underline{\Phi}_{0x(1m)}^{G}\left(y,z,d_m,h_m\right)=-\frac{j\omega\mu_0}{2\pi}\Big\{&K_0\left[jk_a d_{nm}\left(y,z,d_m,h_m\right)\right]\\&-K_0\left[jk_a D_{nm}\left(y,z,d_m,h_m\right)\right]+2\underline{\underline{S}}_{1}^{\mathrm{u}}\left(y,z,d_m,h_m\right)\Big\}\end{aligned} \tag{2.60}$$

where K_0 is the modified Bessel function of the second kind with zero order and $\underline{\underline{S}}_{1}^{\mathrm{u}}\left(y,z,d_m,h_m\right)$ is Sommerfeld integral (A.11) based on the uniform current assumption.

$$\underline{\underline{S}}_{1}^{\mathrm{u}}\left(y,z,d_m,h_m\right)=\int_0^{+\infty}\frac{e^{-\left(z+z_m\right)\sqrt{\lambda^2-k_a^2}}}{\sqrt{\lambda^2-k_a^2}+\sqrt{\lambda^2-k_e^2}}\cos\left[\left(y-y_m\right)\lambda\right]d\lambda \tag{2.61}$$

Also, K_0 can be represented by Bessel function of third kind (Hankel function) [87].

$$K_0(jw) = \frac{j\pi}{2} H_0^{(2)}(w) \tag{2.62}$$

where w is the argument.

2.4 Concluding remarks

This chapter shows a rigorous formulation of electromagnetic fields produced by an overhead line with N conductors. The proposed formulas allow an efficient calculation of electric and magnetic field components radiated from the overhead line. The generalized earth-return impedance and admittance formulas have been proposed based on complete field solution. However, the formulas based on the complete field solution require accurately evaluated unknown modal wave number. Thus, in order to avoid such numerical difficulties, the earth-return impedance and admittance formulas based on a quasi-TEM assumption are also derived. It is shown that well-known Carson's and Pollaczek's earth-return impedance and existing formulas of the earth-return impedance and admittance are deduced from the complete field solution by considering the same assumptions. Finally, a modified earth-return Green function based on the quasi-TEM and uniform current assumptions has been proposed. It can be adopted into the existing MoM-SO method.

CHAPTER 3 DERIVATION OF ELECTROMAGNETIC FIELD EQUATIONS AND EARTH-RETURN PARAMETERS FOR AN UNDERGROUND CABLE SYSTEM

Similarly to Chapter 2, the complete electromagnetic field solution of an underground cable system with N cables is developed based on rigorous Maxwell equations. Then, the generalized earth-return impedance and admittance formulas are derived by adopting the complete field solution with exact voltage and current propagation equations for a multi-phase cable. Three different approaches of a cable voltage calculation related to different earth-return impedance and admittance formulas are discussed. Moreover, quasi-TEM based earth-return impedance and admittance formulas are deduced from the formulas of the complete field solution. In addition, approximate earth-return impedance and admittance formulas are also developed. No Sommerfeld integral is involved in the approximate formulas which can be easily calculated. In the last section, the proposed formulas are discussed in comparison with existing formulas.

3.1 Derivation of electromagnetic field formulas

The configuration of an underground cable system with N cables is illustrated in Figure 3.1, where the cable is composed of an ideal conductor of radius r_i and an insulator (μ_{ins} and ε_{ins}) of radius r_o. The homogenous earth has the same parameters as in Figure 2.1.

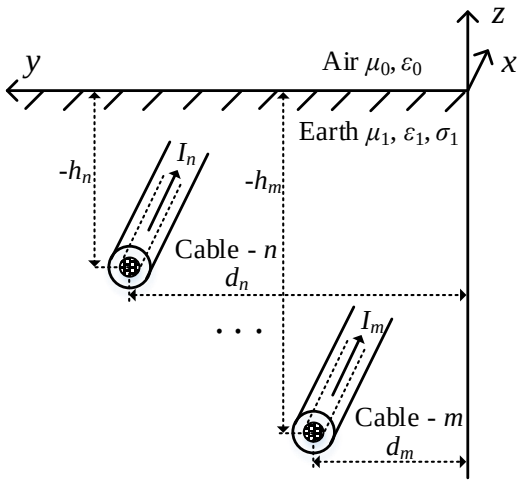

Figure 3.1: Configuration of an underground cable system with *N* cables buried in a homogenous earth

It should be noted that the cables are located at the negative side of *z*-axis, i.e. the buried depth of a cable is negative. Cable - m carries the same filament current $I_m(x)$ as (2.1). By adopting the same modal and electromagnetic analysis in Section 2.1, the *x*-component of the electric and magnetic Hertz vectors at any point in the air and earth can be given by [54]:

$$\Pi_{0E}(x,y,z) = -\frac{j\omega\mu_1}{4\pi k_e^2}\sum_{m=1}^{N}\sum_{v=1}^{N} B_{mv} i_v(x) \int_{-\infty}^{+\infty} \frac{R_{Ev} e^{h_m u_{1v} - z u_{0v}}}{u_{1v}} e^{-j(y-d_m)\lambda} d\lambda \tag{3.1}$$

$$\Pi_{0M}(x,y,z) = -\frac{j\omega\mu_1}{4\pi k_e^2}\sum_{m=1}^{N}\sum_{v=1}^{N} B_{mv} i_v(x) \int_{-\infty}^{+\infty} \frac{R_{Mv} e^{h_m u_{1v} - z u_{0v}}}{u_{1v}} e^{-j(y-d_m)\lambda} d\lambda \tag{3.2}$$

$$\Pi_{1E}(x,y,z) = -\frac{j\omega\mu_1}{4\pi k_e^2}\sum_{m=1}^{N}\sum_{v=1}^{N} B_{mv} i_v(x) \int_{-\infty}^{+\infty} \frac{e^{-|z-h_m|u_{1v}} + T_{Ev} e^{(z+h_m)u_{1v}}}{u_{1v}} e^{-j(y-d_m)\lambda} d\lambda \tag{3.3}$$

$$\Pi_{1M}(x,y,z) = -\frac{j\omega\mu_1}{4\pi k_e^2}\sum_{m=1}^{N}\sum_{v=1}^{N} B_{mv} i_v(x) \int_{-\infty}^{+\infty} \frac{T_{Mv} e^{(z+h_m)u_{1v}}}{u_{1v}} e^{-j(y-d_m)\lambda} d\lambda \tag{3.4}$$

where u_{0v}, u_{1v} and k_e^2 are given in (2.14) and (2.15).

The irrationals R_{Ev}, R_{Mv}, T_{Ev} and T_{Mv} can be derived by adopting the following boundary conditions [54] at the air / earth interface ($z = 0$), referred to the *v*-th mode.

$$\left.\begin{aligned} E_{1x} &= E_{0x} \\ E_{1y} &= E_{0y} \\ H_{1x} &= H_{0x} \\ H_{1y} &= H_{0y} \end{aligned}\right\} \tag{3.5}$$

Solving (3.5) with $\mu_1 = \mu_0$, T_{Ev} and T_{Mv} can be deduced as:

$$T_{Ev} = -1 + 2\frac{k_e^2 u_{1v}}{k_e^2 - k_v^2}\left(\frac{1}{u_{0v} + u_{1v}} - \frac{k_v^2}{k_e^2 u_{0v} + k_a^2 u_{1v}}\right) \tag{3.6}$$

$$T_{Mv} = -2\frac{k_e^2 k_v \lambda}{j\omega\mu_0\left(k_e^2 - k_v^2\right)}\left(\frac{1}{u_{0v} + u_{1v}} - \frac{k_e^2}{k_e^2 u_{0v} + k_a^2 u_{1v}}\right) \tag{3.7}$$

By substituting (3.6) and (3.7) into (3.3) and (3.4), and solving (2.3) and (2.4), the formulas of electromagnetic field components at an arbitrary point in the earth are derived.

$$E_{1x}(x,y,z)=\sum_{m=1}^{N}\sum_{v=1}^{N}\Lambda_{1x}(y,z,d_m,h_m,v)B_{mv}i_v(x) \tag{3.8}$$

$$E_{1y}(x,y,z)=\sum_{m=1}^{N}\sum_{v=1}^{N}\Lambda_{1y}(y,z,d_m,h_m,v)B_{mv}i_v(x) \tag{3.9}$$

$$E_{1z}(x,y,z)=\sum_{m=1}^{N}\sum_{v=1}^{N}\Lambda_{1z}(y,z,d_m,h_m,v)B_{mv}i_v(x) \tag{3.10}$$

$$H_{1x}(x,y,z)=\sum_{m=1}^{N}\sum_{v=1}^{N}\Psi_{1x}(y,z,d_m,h_m,v)B_{mv}i_v(x) \tag{3.11}$$

$$H_{1y}(x,y,z)=\sum_{m=1}^{N}\sum_{v=1}^{N}\Psi_{1y}(y,z,d_m,h_m,v)B_{mv}i_v(x) \tag{3.12}$$

$$H_{1z}(x,y,z)=\sum_{m=1}^{N}\sum_{v=1}^{N}\Psi_{1z}(y,z,d_m,h_m,v)B_{mv}i_v(x) \tag{3.13}$$

where the kernel functions $\Lambda_{1x}(y,z,d_m,h_m,v)$, $\Lambda_{1y}(y,z,d_m,h_m,v)$, $\Lambda_{1z}(y,z,d_m,h_m,v)$, $\Psi_{1x}(y,z,d_m,h_m,v)$, $\Psi_{1y}(y,z,d_m,h_m,v)$ and $\Psi_{1z}(y,z,d_m,h_m,v)$ are given in Appendix A.2.

Equations (3.8) to (3.13) can be rewritten into matrix expression as a function of the exciting modal currents.

$$\begin{bmatrix}E_{1x}(x,y,z)\\E_{1y}(x,y,z)\\E_{1z}(x,y,z)\end{bmatrix}=\begin{bmatrix}\Phi_{1x}(y,z,d_m,h_m,1) & \cdots & \Phi_{1x}(y,z,d_m,h_m,N)\\\Phi_{1y}(y,z,d_m,h_m,1) & \cdots & \Phi_{1y}(y,z,d_m,h_m,N)\\\Phi_{1z}(y,z,d_m,h_m,1) & \cdots & \Phi_{1z}(y,z,d_m,h_m,N)\end{bmatrix}\begin{bmatrix}i_1(x)\\\vdots\\i_N(x)\end{bmatrix} \tag{3.14}$$

$$\begin{bmatrix}H_{1x}(x,y,z)\\H_{1y}(x,y,z)\\H_{1z}(x,y,z)\end{bmatrix}=\begin{bmatrix}\Upsilon_{1x}(y,z,d_m,h_m,1) & \cdots & \Upsilon_{1x}(y,z,d_m,h_m,N)\\\Upsilon_{1y}(y,z,d_m,h_m,1) & \cdots & \Upsilon_{1y}(y,z,d_m,h_m,N)\\\Upsilon_{1z}(y,z,d_m,h_m,1) & \cdots & \Upsilon_{1z}(y,z,d_m,h_m,N)\end{bmatrix}\begin{bmatrix}i_1(x)\\\vdots\\i_N(x)\end{bmatrix} \tag{3.15}$$

where

$$\Phi_{1x}(y,z,d_m,h_m,v)=\sum_{m=1}^{N}\Lambda_{1x}(y,z,d_m,h_m,v)B_{mv} \tag{3.16}$$

$$\Phi_{1y}(y,z,d_m,h_m,v)=\sum_{m=1}^{N}\Lambda_{1y}(y,z,d_m,h_m,v)B_{mv} \tag{3.17}$$

$$\Phi_{1z}(y,z,d_m,h_m,v)=\sum_{m=1}^{N}\Lambda_{1z}(y,z,d_m,h_m,v)B_{mv} \tag{3.18}$$

$$\Upsilon_{1x}(y,z,d_m,h_m,v)=\sum_{m=1}^{N}\Psi_{1x}(y,z,d_m,h_m,v)B_{mv} \tag{3.19}$$

$$\Upsilon_{1y}(y,z,d_m,h_m,v)=\sum_{m=1}^{N}\Psi_{1y}(y,z,d_m,h_m,v)B_{mv} \tag{3.20}$$

$$\Upsilon_{1z}(y,z,d_m,h_m,v)=\sum_{m=1}^{N}\Psi_{1z}(y,z,d_m,h_m,v)B_{mv} \tag{3.21}$$

The matrix expression (3.14) and (3.15) is rewritten in the following simple form.

$$\left.\begin{aligned}\mathbf{E}_1&=\mathbf{\Phi}_1\mathbf{i}\\ \mathbf{H}_1&=\mathbf{\Upsilon}_1\mathbf{i}\end{aligned}\right\} \tag{3.22}$$

where $\mathbf{E}_1$ and $\mathbf{H}_1$ are an $N\times 1$ electromagnetic field vector, $\mathbf{\Phi}_1$ and $\mathbf{\Upsilon}_1$ are a $3\times N$ modal current to field operator's matrix, and $\mathbf{i}$ is defined in (2.33).

In the same manner as Section 2.1, the radiated electromagnetic field in the earth driven by the impressed voltage source $\mathbf{V_f}$ is given by:

$$\left.\begin{aligned}\mathbf{E}_1&=\mathbf{\Phi}_1\mathbf{B}^{-1}\mathbf{Y}_0\mathbf{A}\zeta\mathbf{A}^{-1}\mathbf{V_f}\\ \mathbf{H}_1&=\mathbf{\Upsilon}_1\mathbf{B}^{-1}\mathbf{Y}_0\mathbf{A}\zeta\mathbf{A}^{-1}\mathbf{V_f}\end{aligned}\right\} \tag{3.23}$$

where $\mathbf{Y}_0$ is an $N\times N$ characteristic admittance matrix of an underground cable in phase domain, $\mathbf{A}$ and ζ are given in (2.35) and (2.36).

3.2 Derivation of modal equation

The modal equation of an underground cable is used to solve unknown modal wave number k_v for (3.23). The derivation of the modal equation is based on the continuity of the axial electric field on the *n*-th cable.

$$\sum_{v=1}^{N} Z_{sn}^{c}\left(r_{on}, r_{in}, v\right) B_{nv} i_v\left(x\right) = \sum_{m=1}^{N}\sum_{v=1}^{N} \Lambda_{1x}\left(d_n, h_n, d_m, h_m, v\right) B_{mv} i_v\left(x\right) \tag{3.24}$$

where $Z_{sn}^{c}\left(r_{on}, r_{in}, v\right)$ is the surface impedance of *n*-th cable for *v*-th mode and it is given by

$$Z_{sn}^{c}\left(r_{on}, r_{in}, v\right) = \frac{k_v^2 - k_{ins}^2}{j\omega 2\pi\varepsilon_{ins}} \ln\left(\frac{r_{on}}{r_{in}}\right) \tag{3.25}$$

where r_{on} and r_{in} are outer and inner radii of *n*-th cable, and

$$k_{ins}^2 = \omega^2 \mu_{ins}\varepsilon_{ins} \tag{3.26}$$

In the evaluation of the right side of (3.24), the self-component, $n = m$, is calculated at the surface of the cable. The mutual element, $n \neq m$, can be calculated at the center of two cables. If $N = 1$, (3.24) is the same as the exact approach of references [54]-[57]. Taking further mathematical manipulation to (3.24) and considering the same eigenvalue analysis in (2.40), the matrix expression of (3.24) can be derived.

$$\mathbf{P^c B_v} = -k_v^2 \mathbf{B_v} \tag{3.27}$$

where the full $N \times N$ matrix $\mathbf{P^c}$ is given by:

$$\mathbf{P^c} = \left(\mathbf{P_2^c}\right)^{-1} \mathbf{P_1^c} \tag{3.28}$$

with

$$\mathbf{P_1^c} = \mathbf{Z_{ins}} + \frac{j\omega\mu_0}{4\pi}\left(\underline{\mathbf{\Delta}}_1^{\mathbf{c}} + 2\underline{\mathbf{S}}_1^{\mathbf{c}}\right),\ \mathbf{P_2^c} = \mathbf{Y_{ins}^{-1}} + \frac{1}{4\pi\left(\sigma_1 + j\omega\varepsilon_1\right)}\left(\underline{\mathbf{\Delta}}_1^{\mathbf{c}} + 2\underline{\mathbf{S}}_2^{\mathbf{c}}\right) \tag{3.29}$$

$\mathbf{Z}_{\mathbf{ins}}$ and $\mathbf{Y}_{\mathbf{ins}}$ are an $N \times N$ diagonal matrix and each element is related to the insulator impedance and admittance of the *n*-th cable [3]. Also, each element of $N \times N$ matrices $\underline{\boldsymbol{\Delta}}_1^{\mathbf{c}}$, $\underline{\mathbf{S}}_1^{\mathbf{c}}$ and $\underline{\mathbf{S}}_2^{\mathbf{c}}$ are given in (3.24) together with (A.27), (A.31) and (A.32).

3.3 Derivation of generalized earth-return impedance and admittance formulas

In this section, the generalized earth-return impedance and admittance formulas of a single underground cable is derived based on the exact voltage and current propagation equations. The same method is also extended to a multi-phase underground cable. Then, the earth-return impedance and admittance formulas based on a quasi-TEM assumption which avoids the numerical difficulties due to k_v in the complete field solution are proposed. The approximate earth-return impedance and admittance formulas are also deduced. The approximate formulas involve no Sommerfeld integrals and thus easily are calculated. Finally, the proposed formulas are discussed in comparison with existing formulas.

3.3.1 Complete field solution

The generalized earth-return impedance and admittance formulas are derived based on the complete field solution with exact voltage and current propagation equations for a single and multi-phase underground cable. Curl Maxwell equations of electromagnetic field and Kelvin-Stokes theorem [85] are:

$$\nabla \times \overline{\mathbf{E}}_1 = -j\omega\mu_0 \overline{\mathbf{H}}_1 \tag{3.30}$$

$$\nabla \times \overline{\mathbf{H}}_1 = \left(j\omega\varepsilon_1 + \sigma_1\right)\overline{\mathbf{E}}_1 \tag{3.31}$$

$$\int_c \overline{\mathbf{F}} \cdot d\mathbf{l} = \iint_s \nabla \times \overline{\mathbf{F}} \cdot d\mathbf{s} \tag{3.32}$$

where $\overline{\mathbf{F}}$ is given in (2.5), ∇ is Laplacian operator, $\overline{\mathbf{E}}_1$ and $\overline{\mathbf{H}}_1$ are:

$$\overline{\mathbf{E}}_1 = \left(\mathbf{E}_1\right)^T \mathbf{e}\,,\ \overline{\mathbf{H}}_1 = \left(\mathbf{H}_1\right)^T \mathbf{e} \tag{3.33}$$

with $\mathbf{E}_1$, $\mathbf{H}_1$ and $\mathbf{e}$ are given in (3.22) and (2.5).

By substituting (3.30) into (3.32), it gives:

$$\int_c \overline{\mathbf{E}}_1 \cdot d\mathbf{l} = -j\omega\mu_0 \iint_s \overline{\mathbf{H}}_1 \cdot d\mathbf{s} \tag{3.34}$$

Equation (3.34) involves a line integral to the electric vector field and a surface integral to the magnetic vector field. Then, taking *z*-component of (3.31), it becomes:

$$\frac{\partial H_{1y}(x,y,z)}{\partial x} - \frac{\partial H_{1x}(x,y,z)}{\partial y} = j\omega\left(\varepsilon_1 - j\frac{\sigma_1}{\omega}\right)E_{1z}(x,y,z) \tag{3.35}$$

where $E_{1z}(x,y,z)$, $H_{1x}(x,y,z)$ and $H_{1y}(x,y,z)$ are given in (3.10), (3.11) and (3.12).

The exact voltage and current propagation equations can be derived by (3.34) and (3.35) together with the following line voltage integral equation on the *n*-th cable.

$$V_n(x) = -\int_{h_r}^{h_n - r_{on}} E_{1z}(x, d_n, z)\, dz \tag{3.36}$$

where h_r indicates a position (depth) in the earth, at which E_{1z} has decayed sufficiently to permit this position to be taken as an effective zero potential level [35], [88].

The accurate way to evaluate (3.36) requires to find the unknown modal wave number and current transformation matrix in modal equation (3.27) firstly. Then, the vertical electric field component is calculated to depth h_r which is adopted by considering the contributions of E_{1z} at different depths until these can be neglected. Next, this depth is adopted in (3.36). However, the accurate method requires the numerical calculations of (3.27) and E_{1z} at each frequency step, and thus it causes complexities. Instead, h_r can be assumed to be the earth surface $h_r = 0$ [60], [88] and the infinite depth in the earth $h_r = -\infty$ [88]-[92]. Also, the following penetration depth of soil can be used [48]:

$$h_r = -\delta_e = -\left\{\frac{\omega^2\varepsilon_1\mu_0}{2}\left[\sqrt{1+\left(\frac{\sigma_1}{\omega\varepsilon_1}\right)^2} - 1\right]\right\}^{-\frac{1}{2}} \tag{3.37}$$

Therefore, the generalized telegrapher's equations are proposed based on different h_r.

3.3.1.1 A single underground cable

3.3.1.1.1 Line voltage integral equation referred to infinite depth in the earth

Figure 3.2 illustrates the integral path of the infinite depth in the earth. It should be noted that a single underground cable (Cable 1) is considered and assumes $d_1 = 0$ in Figure 3.1. The positive direction of the integral path: C_1-C_2-C_3-C_4 adopts the anti-clock direction. Also, the direction of the normal vector $\mathbf{n}$ of area S is $-\mathbf{e}_\mathbf{y}$.

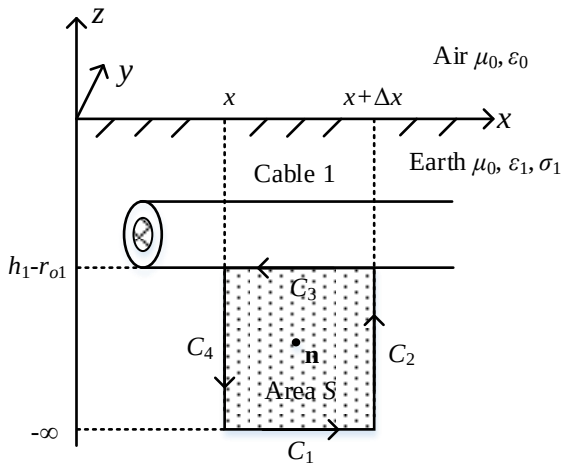

Figure 3.2: The integral path with the reference at the infinite depth

The following expression is deduced by solving (3.34).

$$\int_{-\infty}^{h_1-r_{o1}} E_{1z}\left(x+\Delta x,0,z\right)dz-\int_{-\infty}^{h_1-r_{o1}} E_{1z}\left(x,0,z\right)dz+\int_{x}^{x+\Delta x} E_{1x}\left(x,0,-\infty\right)dx \\ -\int_{x}^{x+\Delta x} E_{1x}\left(x,0,h_1-r_{o1}\right)dx=j\omega\mu_0\int_{-\infty}^{h_1-r_{o1}}\int_{x}^{x+\Delta x} H_{1y}\left(x,0,z\right)dxdz \tag{3.38}$$

Based on the radiation condition, the electromagnetic fields are zero at infinite position, and it has:

$$\int_{x}^{x+\Delta x} E_{1x}\left(x,0,-\infty\right)dx=0 \tag{3.39}$$

By substituting (3.39) into (3.38) and taking limit $\Delta x\to 0$, the following relation is obtained.

$$\lim_{\Delta x\to 0}\frac{\int_{-\infty}^{h_1-r_{o1}} E_{1z}\left(x+\Delta x,0,z\right)dz-\int_{-\infty}^{h_1-r_{o1}} E_{1z}\left(x,0,z\right)dz}{\Delta x}-\lim_{\Delta x\to 0}\frac{\int_{x}^{x+\Delta x} E_{1x}\left(x,0,h_1-r_{o1}\right)dx}{\Delta x}$$
$$=\lim_{\Delta x\to 0}\frac{j\omega\mu_0\int_{-\infty}^{h_1-r_{o1}}\int_{x}^{x+\Delta x} H_{1y}\left(x,0,z\right)dxdz}{\Delta x} \tag{3.40}$$

The first term on the left side of (3.40) represents the voltage propagation characteristic. The voltage propagation equation of Cable 1 is derived by substituting (3.36) into (3.40).

$$-\frac{dV_1\left(x\right)}{dx}=E_{1x}\left(x,0,h_1-r_{o1}\right)+j\omega\mu_0\int_{-\infty}^{h_1-r_{o1}} H_{1y}\left(x,0,z\right)dz \tag{3.41}$$

where $E_{1x}\left(x,0,h_1-r_{o1}\right)$ represents the axial electric field at Cable 1 surface, and it can be replaced by the surface impedance of the cable in (3.25). $H_{1y}\left(x,y,z\right)$ is given in (3.12).

The second term of the right side in (3.41) represents the external magnetic flux between the cable and earth. Then, (3.41) is rewritten in the following form.

$$-\frac{dV_1\left(x\right)}{dx}=Z_{s1}^{c}\left(r_{o1},r_{i1},1\right)I_1\left(x\right)+Z_e\left(0,h_1-r_{o1},d_1,h_1,1\right)I_1\left(x\right) \tag{3.42}$$

where $Z_e\left(0,h_1-r_{o1},d_1,h_1,1\right)$ is the earth-return impedance of Cable 1 given by:

$$\begin{aligned}Z_e\left(y,z,d_1,h_1,v\right)&=\frac{j\omega\mu_0}{4\pi}\underline{\Delta}_1^{c}\left(y,z,d_1,h_1,v\right)\\&+\frac{j\omega\mu_0}{2\pi}\left[\underline{S}_{11}^{c}\left(y,z,d_1,h_1,v\right)-k_e^2\underline{S}_{13}^{c}\left(y,z,d_1,h_1,v\right)+k_v^2\underline{S}_{14}^{c}\left(y,z,d_1,h_1,v\right)\right]\end{aligned} \tag{3.43}$$

where $\underline{\Delta}_1^{c}\left(y,z,d_1,h_1,v\right)$, $\underline{S}_{11}^{c}\left(y,z,d_1,h_1,v\right)$, $\underline{S}_{13}^{c}\left(y,z,d_1,h_1,v\right)$ and $\underline{S}_{14}^{c}\left(y,z,d_1,h_1,v\right)$ are given in Appendix A.2.

Integrating (3.35) with the same integral path:

$$\int_{-\infty}^{h_1-r_{o1}}\left[\frac{\partial H_{1y}\left(x,0,z\right)}{\partial x}-\left.\frac{\partial H_{1x}\left(x,y,z\right)}{\partial y}\right|_{y=0}\right]dz=\left(j\omega\varepsilon_1+\sigma_1\right)\int_{-\infty}^{h_1-r_{o1}} E_{1z}\left(x,0,z\right)dz \tag{3.44}$$

where $E_{1z}\left(x,y,z\right)$ and $H_{1x}\left(x,y,z\right)$ are given in (3.10) and (3.11).

The current propagation equation of Cable 1 is deduced by solving (3.44) and (3.36).

$$-\frac{dI_1(x)}{dx} = Y_e(0, h_1 - r_{o1}, d_1, h_1, 1)V_1(x) \tag{3.45}$$

where $Y_e(0, h_1 - r_{o1}, d_1, h_1, 1)$ is the earth-return admittance of Cable 1 given by:

$$Y_e(y, z, d_1, h_1, v) = \frac{4\pi(j\omega\varepsilon_1 + \sigma_1)}{\left[\underline{\Delta}_1^c(y, z, d_1, h_1, v) + 2\underline{S}_{12}^c(y, z, d_1, h_1, v) - 2k_e^2\underline{S}_{13}^c(y, z, d_1, h_1, v) + 2k_v^2\underline{S}_{14}^c(y, z, d_1, h_1, v)\right]} \tag{3.46}$$

where $\underline{S}_{12}^c(y, z, d_1, h_1, v)$ is given in Appendix A.2.

3.3.1.1.2 Line voltage integral equation referred to the earth surface

In this section, the earth-return impedance and admittance formulas are developed by adopting the earth surface as the integral reference in (3.36). Figure 3.3 shows the same direction of the integral path and the normal vector of area *S* as those in Figure 3.2.

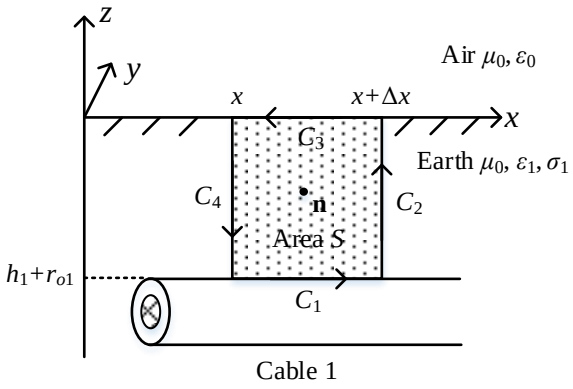

Figure 3.3: The integral path with the reference at the earth surface

In the same manner as (3.42), the voltage propagation equation of Cable 1 is given by:

$$-\frac{dV_1(x)}{dx} = E_{1x}(x, 0, h_1 + r_{o1}) - E_{1x}(x, 0, 0) + j\omega\mu_0\int_0^{h_1+r_{o1}} H_{1y}(x, 0, z)\,dz \tag{3.47}$$

Equation (3.47) is rewritten in the following form similarly to (3.42).

$$-\frac{dV_1(x)}{dx} = Z_{s1}^c(r_{o1}, r_{i1}, 1) I_1(x) + Z_e(0, h_1 - r_{o1}, d_1, h_1, 1) I_1(x) \tag{3.48}$$

where the earth-return impedance $Z_e(0, h_1 - r_{o1}, d_1, h_1, 1)$ becomes:

$$Z_e(0, h_1 - r_{o1}, d_1, h_1, 1) = Z_{es}(0, 0, d_1, h_1, 1) + Z_{e\varphi}(0, h_1 - r_{o1}, d_1, h_1, 1) \tag{3.49}$$

where $Z_{es}(0, 0, d_1, h_1, 1)$ and $Z_{e\varphi}(0, h_1 - r_{o1}, d_1, h_1, 1)$ are the earth surface impedance and external magnetic flux impedance defined as:

$$Z_{es}(y, z, d_1, h_1, v) = \frac{j\omega\mu_0}{2\pi}\left[\underline{S}_1^c(y, z, d_1, h_1, v) - \frac{k_v^2}{k_e^2}\underline{S}_2^c(y, z, d_1, h_1, v)\right] \tag{3.50}$$

$$\begin{aligned} Z_{e\varphi}(y, z, d_1, h_1, v) = {} & \frac{j\omega\mu_0}{4\pi}\underline{\Delta}_1^c(y, z, d_1, h_1, v) \\ & + \frac{j\omega\mu_0}{2\pi}\left[\underline{S}_{11}^c(y, z, d_1, h_1, v) - k_e^2\underline{S}_{13}^c(y, z, d_1, h_1, v) + k_v^2\underline{S}_{14}^c(y, z, d_1, h_1, v)\right] \\ & - \frac{j\omega\mu_0}{2\pi}\left[\underline{S}_{11}^c(y, 0, d_1, h_1, v) - k_e^2\underline{S}_{13}^c(y, 0, d_1, h_1, v) + k_v^2\underline{S}_{14}^c(y, 0, d_1, h_1, v)\right] \end{aligned} \tag{3.51}$$

In (3.48) and (3.49), $Z_{es}(0, 0, d_1, h_1, 1) I_1(x)$ represents the per-unit length voltage drop on the earth surface due to the current $I_1(x)$. $Z_{e\varphi}(0, h_1 - r_{o1}, d_1, h_1, 1)$ is the external magnetic flux impedance due to the field scattered from the earth surface.

The current propagation equation is developed in the same manner as (3.45) but referring to the earth surface as the integral reference as:

$$-\frac{dI_1(x)}{dx} = Y_e(0, h_1 - r_{o1}, d_1, h_1, 1) V_1(x) \tag{3.52}$$

where the earth-return admittance $Y_e(0, h_1 - r_{o1}, d_1, h_1, 1)$ is:

$$\begin{aligned} Y_e(y, z, d_1, h_1, v) = {} & 4\pi(j\omega\varepsilon_1 + \sigma_1)\Big[\underline{\Delta}_1^c(y, z, d_1, h_1, v) + 2\underline{S}_{12}^c(y, z, d_1, h_1, v) \\ & - 2k_e^2\underline{S}_{13}^c(y, z, d_1, h_1, v) + 2k_v^2 S_{14}^c(y, z, d_1, h_1, v) - 2\underline{S}_{12}^c(y, 0, d_1, h_1, v) \\ & + 2k_e^2\underline{S}_{13}^c(y, 0, d_1, h_1, v) - 2k_v^2 S_{14}^c(y, 0, d_1, h_1, v)\Big]^{-1} \end{aligned} \tag{3.53}$$

3.3.1.2 Multi-phase underground cable

3.3.1.2.1 Line voltage integral equation referred to infinite depth in the earth

The earth-return impedance and admittance formulas of a multi-phase cable are derived based on the modal analysis and the formulation of voltage and current propagation equations as explained in Section 3.3.1.1. The voltage propagation equation of the *n*-th cable to the reference of the infinite depth is:

$$-\frac{dV_n(x)}{dx} = E_{1x}(x, d_n, h_n - r_{on}) + j\omega\mu_0 \int_{-\infty}^{h_n - r_{on}} H_{1y}(x, d_n, z)\, dz \tag{3.54}$$

Similarly to (3.41), the first term on the right side of (3.54) represents the axial electric field at the *n*-th cable surface. The second term represents the external magnetic flux between the *n*-th cable and earth. Substituting (3.8) and (3.12) into (3.54), rewriting in a matrix expression and transferring back to the phase domain, the following earth-return impedance formula is obtained.

$$\mathbf{Z_e} = \mathbf{Z_f}\mathbf{B}^{-1} \tag{3.55}$$

where $\mathbf{Z_f}$ is the earth flux impedance matrix in modal domain and the *nv*-th element of matrix $\mathbf{Z_f}$ is given by:

$$Z_{f(nv)}(d_n, h_n - r_{on}, d_m, h_m, v) = \sum_{m=1}^{N} Z_{fn}(d_n, h_n - r_{on}, d_m, h_m, v) B_{mv} \tag{3.56}$$

where

$$\begin{aligned} Z_{fn}(y, z, d_m, h_m, v) = {} & \frac{j\omega\mu_0}{4\pi} \underline{\Delta}_1^c(y, z, d_m, h_m, v) \\ & + \frac{j\omega\mu_0}{2\pi}\left[\underline{S}_{11}^c(y, z, d_m, h_m, v) - k_e^2 \underline{S}_{13}^c(y, z, d_m, h_m, v) + k_v^2 \underline{S}_{14}^c(y, z, d_m, h_m, v)\right] \end{aligned} \tag{3.57}$$

In the same manner, the following earth-return admittance formula in phase domain is obtained from the current propagation equation of the *n*-th cable.

$$\mathbf{Y_e} = \left(\mathbf{Y_f}\mathbf{B}^{-1}\right)^{-1} \tag{3.58}$$

where $\mathbf{Y_f}$ is a coefficient matrix in modal domain and the *nv*-th element of $\mathbf{Y_f}$ is given by:

$$Y_{f(nv)}\left(d_n, h_n - r_{on}, d_m, h_m, v\right) = \sum_{m=1}^{N} Y_{fn}\left(d_n, h_n - r_{on}, d_m, h_m, v\right) B_{mv} \tag{3.59}$$

where

$$\begin{aligned} Y_{fn}\left(y, z, d_m, h_m, v\right) = \frac{1}{4\pi\left(\sigma_1 + j\omega\varepsilon_1\right)}\Big[& \underline{\Delta}_1^c\left(y, z, d_m, h_m, v\right) \\ & + 2\underline{S}_{12}^c\left(y, z, d_m, h_m, v\right) - 2k_e^2\,\underline{S}_{13}^c\left(y, z, d_m, h_m, v\right) + 2k_v^2\,\underline{S}_{14}^c\left(y, z, d_m, h_m, v\right)\Big] \end{aligned} \tag{3.60}$$

3.3.1.2.2 Line voltage integral equation referred to the earth surface

If the integral reference is changed to the earth surface, the earth-return impedance and admittance formulas have the same expressions as (3.55) and (3.58) with different $\mathbf{Z_f}$ and $\mathbf{Y_f}$. For the earth-return impedance formula, the *nv*-th element of matrix $\mathbf{Z_f}$ is given by:

$$Z_{f(nv)}\left(d_n, h_n - r_{on}, d_m, h_m, v\right) = \sum_{m=1}^{N} Z_{fn}\left(d_n, h_n - r_{on}, d_m, h_m, v\right) B_{mv} \tag{3.61}$$

where

$$Z_{fn}\left(y, z, d_m, h_m, v\right) = Z_{es}\left(y, 0, d_m, h_m, v\right) + Z_{e\varphi}\left(y, z, d_m, h_m, v\right) \tag{3.62}$$

and

$$Z_{es}\left(y, 0, d_m, h_m, v\right) = \frac{j\omega\mu_0}{2\pi}\left[\underline{S}_1^c\left(y, 0, d_m, h_m, v\right) - \frac{k_v^2}{k_e^2}\underline{S}_2^c\left(y, 0, d_m, h_m, v\right)\right] \tag{3.63}$$

$$\begin{aligned} Z_{e\varphi}\left(y, z, d_m, h_m, v\right) = & \frac{j\omega\mu_0}{4\pi}\underline{\Delta}_1^c\left(y, z, d_m, h_m, v\right) \\ & + \frac{j\omega\mu_0}{2\pi}\left[\underline{S}_{11}^c\left(y, z, d_m, h_m, v\right) - k_e^2\,\underline{S}_{13}^c\left(y, z, d_m, h_m, v\right) + k_v^2\,\underline{S}_{14}^c\left(y, z, d_m, h_m, v\right)\right] \\ & - \frac{j\omega\mu_0}{2\pi}\left[\underline{S}_{11}^c\left(y, 0, d_m, h_m, v\right) - k_e^2\,\underline{S}_{13}^c\left(y, 0, d_m, h_m, v\right) + k_v^2\,\underline{S}_{14}^c\left(y, 0, d_m, h_m, v\right)\right] \end{aligned} \tag{3.64}$$

Similarly, the earth-return admittance formula is given by:

$$Y_{f(nv)}\left(d_n, h_n - r_{on}, d_m, h_m, v\right) = \sum_{m=1}^{N} Y_{fn}\left(d_n, h_n - r_{on}, d_m, h_m, v\right) B_{mv} \tag{3.65}$$

where

$$\begin{aligned} Y_{fn}\left(y, z, d_m, h_m, v\right) = \frac{1}{4\pi\left(\sigma_1 + j\omega\varepsilon_1\right)} \Big[& \underline{\Delta}_1^c\left(y, z, d_m, h_m, v\right) \\ & + 2\underline{S}_{12}^c\left(y, z, d_m, h_m, v\right) - 2k_e^2\,\underline{S}_{13}^c\left(y, z, d_m, h_m, v\right) + 2k_v^2\,\underline{S}_{14}^c\left(y, z, d_m, h_m, v\right) \\ & - 2\underline{S}_{12}^c\left(y, 0, d_m, h_m, v\right) + 2k_e^2\,\underline{S}_{13}^c\left(y, 0, d_m, h_m, v\right) - 2k_v^2\,\underline{S}_{14}^c\left(y, 0, d_m, h_m, v\right) \Big] \end{aligned} \tag{3.66}$$

3.3.2 Quasi-TEM solution

The earth-return impedance and admittance formulas based on the complete electromagnetic field solutions are proposed in Section 3.3.1. In this section, the assumption of quasi-TEM propagation is adopted to derive a quite simple form of the earth-return impedance and admittance so that anyone can use the formulas in a study of wave propagation and power system transients.

3.3.2.1 Numerical difficulties for the formulas based on complete electromagnetic field solutions

The modal equation and earth-return impedance and admittance formulas of a multi-phase underground cable are summarized as:

$$\mathbf{P^c B_v} = -k_v^2 \mathbf{B_v} \tag{3.67}$$

$$\left.\begin{aligned} \mathbf{Z_e} &= \mathbf{Z_f B^{-1}} \\ \mathbf{Y_e} &= \left(\mathbf{Y_f B^{-1}}\right)^{-1} \end{aligned}\right\} \tag{3.68}$$

Equation (3.67) is the modal equation of a multi-phase underground cable, which is obtained by enforcing the boundary condition for the electric field at the earth / cable interface. Equation (3.68) shows the matrices of the earth-return parameters of the multi-phase cable based on $h_r = -\infty$ or $h_r = 0$. The details can be found in Sections 3.2 and 3.3.1. Before solving (3.68), unknown modal

wave number k_v and current transformation matrix $\mathbf{B}$ should be calculated by solving a nonlinear integral eigenvalue equation in (3.67). Then, by substituting k_v, $\mathbf{B}$, geometrical data of the cable and the earth parameters into (3.68), $\mathbf{Z_e}$ and $\mathbf{Y_e}$ can be calculated. However, the numerical calculation of (3.67) is very complicated in any case because each element of target matrix $\mathbf{P^c}$ is a nonlinear integral function of k_v. The quasi-TEM assumption, $k_v \approx 0$ [56], [57], [59], can be adopted and it covers the majority of surge phenomena in a cable system [56], [57], [59].

3.3.2.2 Earth-return impedance and admittance formulas based on quasi-TEM assumption

By substituting $k_v \approx 0$ into the formulation of (3.68), the earth-return impedance and admittance formulas can be significantly simplified and rewritten based on reference [54]. For the earth-return impedance between cables n and m:

$$\begin{aligned}\underline{Z}_{e(nm)}\left(d_n,h_n,d_m,h_m\right)=\frac{j\omega\mu_0}{2\pi}\Big\{&K_0\left[jk_e d_{nm}\left(d_n,h_n,d_m,h_m\right)\right]-K_0\left[jk_e D_{nm}\left(d_n,h_n,d_m,h_m\right)\right]\\&+2\underline{\underline{S}}^c_{11}\left(d_n,h_n,d_m,h_m\right)-2k_e^2\underline{\underline{S}}^c_{13}\left(d_n,h_n,d_m,h_m\right)\Big\}\end{aligned} \tag{3.69}$$

where $d_{nm}\left(y,z,d_m,h_m\right)$, $D_{nm}\left(y,z,d_m,h_m\right)$ and K_0 are given in (2.48), (2.49) and (2.60).

and, $\underline{\underline{S}}^c_{11}\left(y,z,d_m,h_m\right)$ and $\underline{\underline{S}}^c_{13}\left(y,z,d_m,h_m\right)$ are Sommerfeld integrals $\underline{S}^c_{11}\left(y,z,d_m,h_m,v\right)$ and $\underline{S}^c_{13}\left(y,z,d_m,h_m,v\right)$ based on quasi-TEM assumption.

$$\underline{\underline{S}}^c_{11}\left(y,z,d_m,h_m\right)=\int_0^{+\infty}\frac{e^{(z+h_m)\sqrt{\lambda^2-k_e^2}}}{\left(\lambda^2-k_e^2\right)\left(\sqrt{\lambda^2-k_a^2}+\sqrt{\lambda^2-k_e^2}\right)}\lambda^2\cos\left[\left(y-d_m\right)\lambda\right]d\lambda \tag{3.70}$$

$$\underline{\underline{S}}^c_{13}\left(y,z,d_m,h_m\right)=\int_0^{+\infty}\frac{e^{(z+h_m)\sqrt{\lambda^2-k_e^2}}}{\left(\lambda^2-k_e^2\right)\left(\sqrt{\lambda^2-k_a^2}+\sqrt{\lambda^2-k_e^2}\right)}\cos\left[\left(y-d_m\right)\lambda\right]d\lambda \tag{3.71}$$

The earth-return admittance between cables n and m can be represented by the earth-return potential coefficient. The different formulas are derived based on different voltage integral references.

3.3.2.2.1 Line voltage integral equation referred to infinite depth in the earth

The earth-return potential coefficient formula between *m*-th and *n*-th cables based on the integral path to infinite depth in the earth ($h_r = -\infty$) is:

$$\begin{aligned}\underline{P}_{e(nm)}\left(d_n,h_n,d_m,h_m\right)=&\frac{j\omega}{2\pi\left(\sigma_1+j\omega\varepsilon_1\right)}\Big\{K_0\left[jk_e d_{nm}\left(d_n,h_n,d_m,h_m\right)\right]\\&-K_0\left[jk_e D_{nm}\left(d_n,h_n,d_m,h_m\right)\right]+2\underline{\underline{S}}^c_{12}\left(d_n,h_n,d_m,h_m\right)\\&-2k_e^2\,\underline{\underline{S}}^c_{13}\left(d_n,h_n,d_m,h_m\right)\Big\}\end{aligned}\tag{3.72}$$

where $\underline{\underline{S}}^c_{12}\left(y,z,d_m,h_m\right)$ is Sommerfeld integral $\underline{S}^c_{12}\left(y,z,d_m,h_m,v\right)$ based on quasi-TEM assumption.

$$\underline{\underline{S}}^c_{12}\left(y,z,d_m,h_m\right)=\int_0^{+\infty}\frac{e^{(z+h_m)\sqrt{\lambda^2-k_e^2}}}{\left(\lambda^2-k_e^2\right)\left(\sqrt{\lambda^2-k_a^2}+k_a^2k_e^{-2}\sqrt{\lambda^2-k_e^2}\right)}\lambda^2\cos\left[\left(y-d_m\right)\lambda\right]d\lambda\tag{3.73}$$

3.3.2.2.2 Line voltage integral equation referred to the earth surface

The earth-return potential coefficient formula between cables n and m based on the integral path to the earth surface ($h_r = 0$) is:

$$\begin{aligned}\underline{P}_{e(nm)}\left(d_n,h_n,d_m,h_m\right)=&\frac{j\omega}{2\pi\left(\sigma_1+j\omega\varepsilon_1\right)}\Big\{K_0\left[jk_e d_{nm}\left(d_n,h_n,d_m,h_m\right)\right]\\&-K_0\left[jk_e D_{nm}\left(d_n,h_n,d_m,h_m\right)\right]+2\underline{\underline{S}}^c_{12}\left(d_n,h_n,d_m,h_m\right)\\&-2k_e^2\,\underline{\underline{S}}^c_{13}\left(d_n,h_n,d_m,h_m\right)\Big\}-\underline{P}_{ec(nm)}\left(d_n,h_n,d_m,h_m\right)\end{aligned}\tag{3.74}$$

where the earth surface correction term $\underline{P}_{ec(nm)}\left(y,z,d_m,h_m\right)$ has:

$$\underline{P}_{ec(nm)}\left(y,z,d_m,h_m\right)=\frac{j\omega}{\pi\left(\sigma_1+j\omega\varepsilon_1\right)}\left[\underline{\underline{S}}^c_{14}\left(y,z,d_m,h_m\right)-k_e^2\,\underline{\underline{S}}^c_{15}\left(y,z,d_m,h_m\right)\right]\tag{3.75}$$

where

$$\underline{\underline{S}}^c_{14}\left(y,z,d_m,h_m\right)=\int_0^{+\infty}\frac{e^{\frac{z+h_m}{2}\sqrt{\lambda^2-k_e^2}}}{\left(\lambda^2-k_e^2\right)\left(\sqrt{\lambda^2-k_a^2}+k_a^2k_e^{-2}\sqrt{\lambda^2-k_e^2}\right)}\lambda^2\cos\left[\left(y-d_m\right)\lambda\right]d\lambda\tag{3.76}$$

$$\underline{\underline{S}}_{15}^{c}\left(y,z,d_m,h_m\right)=\int_0^{+\infty}\frac{e^{\frac{z+h_m}{2}\sqrt{\lambda^2-k_e^2}}}{\left(\lambda^2-k_e^2\right)\left(\sqrt{\lambda^2-k_a^2}+\sqrt{\lambda^2-k_e^2}\right)}\cos\left[\left(y-d_m\right)\lambda\right]d\lambda \tag{3.77}$$

3.3.2.2.3 Line voltage integral equation referred to penetration depth in the earth

The earth-return potential coefficient formula between cable n and m based on penetration depth in the earth ($h_r=-\delta_e$) is:

$$\begin{aligned}\underline{P}_{e(nm)}\left(d_n,h_n,d_m,h_m\right)=&\frac{j\omega}{2\pi\left(\sigma_1+j\omega\varepsilon_1\right)}\left\{K_0\left[jk_e d_{nm}\left(d_n,h_n,d_m,h_m\right)\right]\right.\\&-K_0\left[jk_e D_{nm}\left(d_n,h_n,d_m,h_m\right)\right]+2\underline{\underline{S}}_{12}^{c}\left(d_n,h_n,d_m,h_m\right)\\&\left.-2k_e^2\underline{\underline{S}}_{13}^{c}\left(d_n,h_n,d_m,h_m\right)\right\}-\underline{P}_{ec(nm)}\left(d_n,h_n,d_m,h_m,h_r\right)\end{aligned} \tag{3.78}$$

where the penetration depth correction term $\underline{P}_{ec(nm)}\left(y,z,d_m,h_m,h_r\right)$ has:

$$\begin{aligned}\underline{P}_{ec(nm)}\left(y,z,d_m,h_m,h_r\right)=&\frac{j\omega}{2\pi\left(\sigma_1+j\omega\varepsilon_1\right)}\left\{K_0\left[jk_e d_{nmc}\left(y,z,d_m,h_m,h_r\right)\right]\right.\\&-K_0\left[jk_e D_{nmc}\left(y,z,d_m,h_m,h_r\right)\right]+2\underline{\underline{S}}_{16}^{c}\left(y,z,d_m,h_m,h_r\right)\\&\left.-2k_e^2\underline{\underline{S}}_{17}^{c}\left(y,z,d_m,h_m,h_r\right)\right\}\end{aligned} \tag{3.79}$$

where h_r is given in (3.37) and

$$d_{nmc}\left(y,z,d_m,h_m,h_r\right)=\sqrt{\left(y-d_m\right)^2+\left(h_r-\frac{z+h_m}{2}\right)^2} \tag{3.80}$$

$$D_{nmc}\left(y,z,d_m,h_m,h_r\right)=\sqrt{\left(y-d_m\right)^2+\left(h_r+\frac{z+h_m}{2}\right)^2} \tag{3.81}$$

$$\underline{\underline{S}}_{16}^{c}\left(y,z,d_m,h_m,h_r\right)=\int_0^{+\infty}\frac{e^{\left(h_r+\frac{z+h_m}{2}\right)\sqrt{\lambda^2-k_e^2}}}{\left(\lambda^2-k_e^2\right)\left(\sqrt{\lambda^2-k_a^2}+k_a^2k_e^{-2}\sqrt{\lambda^2-k_e^2}\right)}\lambda^2\cos\left[\left(y-d_m\right)\lambda\right]d\lambda \tag{3.82}$$

$$\underline{\underline{S}}_{17}^{c}\left(y,z,d_m,h_m,h_r\right)=\int_0^{+\infty}\frac{e^{\left(h_r+\frac{z+h_m}{2}\right)\sqrt{\lambda^2-k_e^2}}}{\left(\lambda^2-k_e^2\right)\left(\sqrt{\lambda^2-k_a^2}+\sqrt{\lambda^2-k_e^2}\right)}\cos\left[\left(y-d_m\right)\lambda\right]d\lambda \qquad (3.83)$$

It should be noted that $h_n=h_m$ and $d_n-d_m=r_{on}$ or $d_n-d_m=r_{om}$ are used for the self-impedance and potential coefficient. The mutual element can be calculated at the center of two cables. By substituting $h_r=0$ into (3.78), (3.74) is deduced. If $h_r=-\infty$ is assumed in (3.78), $\underline{P}_{ec(nm)}\left(d_n,h_n,d_m,h_m,h_r\right)\to 0$, (3.72) is derived.

It is important to discuss the influence of h_r on the earth-return impedance and potential coefficient. By adopting quasi-TEM assumption, the earth-return impedance becomes independent on h_r, i.e. (3.69) becomes identical to the formulas based on $h_r=-\infty$ and $h_r=0$.

However, h_r shows a significant influence on the earth-return potential coefficient. In fact, correction term $\underline{P}_{ec(nm)}\left(d_n,h_n,d_m,h_m,h_r\right)$ of (3.78) comes from the influence of E_{1z} at the effective zero potential level "h_r" in (3.36). In theory, E_{1z} should have decayed sufficiently at h_r, otherwise non-zero E_{1z} contributes to the voltage in (3.36) and results in the correction term $\underline{P}_{ec(nm)}\left(d_n,h_n,d_m,h_m,h_r\right)$ in (3.78). Thus, (3.74) should not be used considering the fact that a cable is often buried close to the earth surface and E_{1z} cannot decay sufficiently to permit the earth surface as an effective zero potential level. Instead of (3.74), (3.72) is adopted to keep $E_{1z}=0$ for the entire region [88]-[92].

3.3.2.3 Applicable limit of quasi-TEM based formulas

It should be noted that (3.69) and (3.72) are limited to the highest frequency of about 10 MHz, because only the first region of quasi-TEM assumption $k_v\approx 0$ is adopted [59]. The configuration of a cable should be much smaller than the wavelength in the earth, and the wavelength is greater than the penetration depth (3.37) in the soil. According to the critical frequency analysis [46], the quasi-TEM assumption or a TL based approach can be applicable up to 10 MHz by assuming that the earth resistivity does not exceed 1000 Ωm. If necessary, a much higher frequency can be handled by adopting $k_v\approx k_e$ [59] in the complete field solutions (3.55) and (3.58).

3.3.3 Discussion of existing and approximate formulas

Pollaczek developed the earth-return impedance of an underground cable for a frequency below several MHz [7]:

$$\begin{aligned}\underline{Z}_{e(nm)}^{\text{Pollaczek}}\left(d_n,h_n,d_m,h_m\right)=\frac{j\omega\mu_0}{2\pi}\Big\{&K_0\left[\,jk_e d_{nm}\left(d_n,h_n,d_m,h_m\right)\right]\\&-K_0\left[\,jk_e D_{nm}\left(d_n,h_n,d_m,h_m\right)\right]+2\underline{\underline{S}}^{\text{Pollaczek}}\left(d_n,h_n,d_m,h_m\right)\Big\}\end{aligned} \tag{3.84}$$

where

$$\underline{\underline{S}}^{\text{Pollaczek}}\left(y,z,d_m,h_m\right)=\int_0^{+\infty}\frac{e^{\left(z+h_m\right)\sqrt{\lambda^2-k_e^2}}}{\lambda+\sqrt{\lambda^2-k_e^2}}\cos\left[\left(y-d_m\right)\lambda\right]d\lambda \tag{3.85}$$

where

$$k_e^2=-j\omega\mu_0\sigma_1 \tag{3.86}$$

Sunde's earth-return impedance formula can be derived when (3.86) is replaced by [9]:

$$k_e^2=-j\omega\mu_0\left(\sigma_1+j\omega\varepsilon_1\right) \tag{3.87}$$

It has been well-known that Pollaczek's formula cannot deal with displacement currents because of neglecting ε_1 in (3.86). Although Sunde's formula includes ε_1, it neglects the intrinsic propagation constant of air.

The concept of the earth-return impedance together with the admittance of an underground cable was originated by Bridges [56], [57]. Papadopoulos proposed modified earth-return impedance and admittance equations and extended to a stratified earth with arbitrary earth properties [44]-[46]. The formula for a homogeneous earth by adopting $\mu_1=\mu_0$ is given by [44]:

$$\underline{Z}_{e(nm)}^{\text{Papadopoulos}}\left(d_n,h_n,d_m,h_m\right)=\frac{j\omega\mu_0}{2\pi}\left[\underline{\underline{\Delta}}_1^{\text{Papadopoulos}}\left(d_n,h_n,d_m,h_m\right)+2\underline{\underline{S}}^{\text{Papadopoulos}}\left(d_n,h_n,d_m,h_m\right)\right] \tag{3.88}$$

$$\underline{P}_{e(nm)}^{\text{Papadopoulos}}\left(d_n,h_n,d_m,h_m\right)=\frac{j\omega}{2\pi\left(\sigma_1+j\omega\varepsilon_1\right)}\left[\underline{\underline{\Delta}}_1^{\text{Papadopoulos}}\left(d_n,h_n,d_m,h_m\right)+2\underline{\underline{S}}^{\text{Papadopoulos}}\left(d_n,h_n,d_m,h_m\right)\right] \tag{3.89}$$

where

$$\underline{\underline{\Delta}}_1^{\text{Papadopoulos}}\left(y,z,d_m,h_m\right)=\int_0^{+\infty}\frac{\left[e^{-|z-h_m|\sqrt{\lambda^2-k_e^2+k_x^2}}-e^{(z+h_m)\sqrt{\lambda^2-k_e^2+k_x^2}}\right]}{\sqrt{\lambda^2-k_e^2+k_x^2}}\cos\left[\left(y-d_m\right)\lambda\right]d\lambda \tag{3.90}$$

$$\underline{\underline{S}}^{\text{Papadopoulos}}\left(y,z,d_m,h_m\right)=\int_0^{+\infty}\frac{e^{(z+h_m)\sqrt{\lambda^2-k_e^2+k_x^2}}}{\sqrt{\lambda^2-k_a^2+k_x^2}+k_a^2k_e^{-2}\sqrt{\lambda^2-k_e^2+k_x^2}}\cos\left[\left(y-d_m\right)\lambda\right]d\lambda \tag{3.91}$$

where k_a^2 is given in (2.15), k_e^2 is given in (3.87) and $k_x=\omega\sqrt{\mu_0\varepsilon_1}$.

In fact, the issue of Papadopoulos' formulas comes from the less generalized formulation of the earth-return impedance and admittance because only electric Hertz vector is adopted [60].

Recently, Magalhaes [59], [60] derived the following formula of the earth-return potential coefficient based on quasi-TEM assumption, which the numerical results are the same as (3.74).

$$\underline{P}_{e(nm)}^{\text{Magalhaes}}\left(d_n,h_n,d_m,h_m\right)=\frac{j\omega}{2\pi\left(\sigma_1+j\omega\varepsilon_1\right)}\left\{K_0\left[jk_ed_{nm}\left(d_n,h_n,d_m,h_m\right)\right]-K_0\left[jk_eD_{nm}\left(d_n,h_n,d_m,h_m\right)\right]-2\underline{\underline{S}}^{\text{Magalhaes}}\left(d_n,h_n,d_m,h_m\right)\right\} \tag{3.92}$$

where

$$\underline{\underline{S}}^{\text{Magalhaes}}\left(y,z,d_m,h_m\right)=\int_0^{+\infty}\frac{\sqrt{\lambda^2-k_a^2}}{\sqrt{\lambda^2-k_e^2}}\frac{e^{\frac{z+h_m}{2}\sqrt{\lambda^2-k_e^2}}-e^{(z+h_m)\sqrt{\lambda^2-k_e^2}}}{\sqrt{\lambda^2-k_a^2}+k_a^2k_e^{-2}\sqrt{\lambda^2-k_e^2}}\cos\left[\left(y-d_m\right)\lambda\right]d\lambda \tag{3.93}$$

where k_a^2 is given in (2.15) and k_e^2 is given in (3.87).

The problem of the above formula by Magalhaes is that the effective zero potential level h_r is assumed to be the earth surface ($h_r=0$). As already explained in Section 3.3.2, this assumption gives inaccurate results.

Saad derived an approximate formula of Pollaczek's earth-return impedance [47]. It is shown in reference [49] that the formula is identical or better compared with the other low frequency approximations proposed by Wedepohl [43] and Semlyen [5].

$$\underline{Z}_{e(nm)}^{\text{Saad}} = \frac{j\omega\mu_0}{2\pi}\left[K_0\left(jk_e R_{ab} \right) + \frac{2e^{(h_n+h_m)jk_e}}{4-k_e^2 R_{ab}^2} \right] \tag{3.94}$$

where k_e^2 is given in (3.86).

Note that in (3.94) and all the closed formulas below, for self-impedance, R_{ab} is the same as the outer insulator radius of a cable. For the mutual impedance between two parallel cables, R_{ab} needs to be replaced by the horizontal distance between the buried cables.

Petrache proposed a simple logarithmic approximation for the earth-return impedance as given by [50]:

$$\underline{Z}_{e(nm)}^{\text{Petrache}} = \frac{j\omega\mu_0}{2\pi}\ln\left(\frac{1+jk_e R_{ab}}{jk_e R_{ab}} \right) \tag{3.95}$$

where k_e^2 is given in (3.87).

However, neglecting the cable depth in (3.95) may result in inaccuracies, especially for low frequencies. Theethayi proposed a modified empirical logarithmic-exponential formula [49], which combines (3.94) and (3.95) to account for the cable depth.

$$\underline{Z}_{e(nm)}^{\text{Theethayi}} = \frac{j\omega\mu_0}{2\pi}\left[\ln\left(\frac{1+jk_e R_{ab}}{jk_e R_{ab}} \right) + \frac{2e^{(h_n+h_m)|jk_e|}}{4-k_e^2 R_{ab}^2} \right] \tag{3.96}$$

where k_e^2 is given in (3.87).

The following approximate formula of the earth-return potential coefficient is proposed in this thesis based on (3.94) and (3.95) by adopting the same manner in references [48]-[50].

$$\underline{P}_{e(nm)} = \frac{j\omega}{2\pi\left(\sigma_1 + j\omega\varepsilon_1\right)}\left[\ln\left(\frac{1+jk_e R_{ab}}{jk_e R_{ab}} \right) + \frac{2e^{(h_n+h_m)jk_e}}{4-k_e^2 R_{ab}^2} \right] \tag{3.97}$$

where k_e^2 is given in (3.87).

3.4 Concluding remarks

Rigorous formulation of electromagnetic fields produced by an underground cable system with N cables has been derived in this chapter. The proposed formulas allow an efficient calculation of electric and magnetic field components radiated from the underground cable. Next, the generalized earth-return impedance and admittance formulas have been proposed based on the complete field solution and exact telegrapher's equations. By adopting the different references for a line voltage integral, such as earth surface and infinite depth of earth, different earth-return impedance and admittance formulas are developed. Moreover, the complete field solutions require the numerical calculations of unknown modal wave number, and thus it causes numerical difficulties. Again, the quasi-TEM based earth-return impedance and admittance formulas are derived to overcome such numerical difficulties.

By adopting the quasi-TEM assumption, the earth-return impedance formula becomes independent on the voltage integral reference. However, the earth-return potential coefficient formula is dependent on the voltage integral. Also, existing formulas are discussed and compared with the newly derived formulas. Finally, an approximate formula of the earth-return potential coefficient is developed. The approximate formula has no Sommerfeld integral, and it can be calculated easily.

CHAPTER 4 WAVE PROPAGATION IN FREQUENCY DOMAIN

In this chapter, the extended and classical TL approaches are explained. The frequency-dependent wave propagation characteristics are investigated for an overhead line, an overhead cable and an underground cable based on the extended and classical TL approaches. The difference between the approaches are also discussed.

4.1 Extended and classical TL approaches

The series impedance and shunt admittance of a cable system, such as an overhead line, overhead cable and underground cable, are defined in the two matrix equations based on TL approach [3].

$$-\frac{d\mathbf{V}}{dx} = \underline{\mathbf{Z}}\mathbf{I} \tag{4.1}$$

$$-\frac{d\mathbf{I}}{dx} = \underline{\mathbf{Y}}\mathbf{V} \tag{4.2}$$

where $\mathbf{V}$ and $\mathbf{I}$ are an $N \times 1$ vector of the voltages and currents at distance x along the cable. $\underline{\mathbf{Z}}$ and $\underline{\mathbf{Y}}$ are an $N \times N$ matrix of the series impedance and shunt admittance of the cable.

In general, the series impedance and shunt admittance matrices of a cable can be expressed in the following forms.

$$\underline{\mathbf{Z}} = \underline{\mathbf{Z}}_{\mathbf{i}} + \underline{\mathbf{Z}}_{\mathbf{e}} \tag{4.3}$$

$$\underline{\mathbf{Y}} = j\omega\underline{\mathbf{P}}^{-1} \tag{4.4}$$

where $\underline{\mathbf{Z}}_{\mathbf{i}}$ and $\underline{\mathbf{Z}}_{\mathbf{e}}$ are the internal and earth-return impedances of the cable. The potential coefficient matrix $\underline{\mathbf{P}}$ is defined as:

$$\underline{\mathbf{P}} = \underline{\mathbf{P}}_{\mathbf{i}} + \underline{\mathbf{P}}_{\mathbf{e}} \tag{4.5}$$

where $\underline{\mathbf{P}}_{\mathbf{i}}$ and $\underline{\mathbf{P}}_{\mathbf{e}}$ are the internal and earth-return potential coefficients of the cable.

Hereafter, (4.3) and (4.4) are designated as “extended TL approach”. Carson’s or Pollaczek’s earth-return impedance with constant space or insulator potential coefficient is called “classical TL

approach". The formulas adopted into extended and classical TL approaches are summarized in Table 4.1. The internal impedance and potential coefficients of the cable is based on references [5].

Table 4.1: Summary of formulas adopted into extended and classical TL approaches

		An Overhead Line / Cable	**An Underground Cable**
Extended TL Approach	$\underline{\mathbf{Z}}_{\mathbf{e}}$	(2.44)	(3.69)
	$\underline{\mathbf{P}}_{\mathbf{e}}$	(2.45)	(3.72)
Classical TL Approach	$\underline{\mathbf{Z}}_{\mathbf{e}}$	(2.50)	(3.84)
	$\underline{\mathbf{P}}_{\mathbf{e}}$	(2.51)	-

4.2 Propagation constant

It has the following matrix operation by adopting (4.3) and (4.4):

$$\mathbf{A}^{-1}\left(\underline{\mathbf{Z}}\underline{\mathbf{Y}}\right)\mathbf{A}=\mathbf{Q} \tag{4.6}$$

where $\mathbf{A}$ is the voltage transformation matrix defined in (2.34) and $\mathbf{Q}$ is an $N\times N$ diagonal matrix.

The modal propagation constant related to *v*-th mode is given by:

$$\gamma_v=\alpha_v+j\beta_v=\sqrt{Q_v}:\ v=1,\cdots,N \tag{4.7}$$

where α_v is modal attenuation constant of the *v*-th mode, β_v is modal phase constant of the *v*-th mode and Q_v is the *v*-th diagonal element of $\mathbf{Q}$.

The modal phase velocity related to *v*-th mode is defined:

$$c_v=\frac{\omega}{\beta_v} \tag{4.8}$$

The wave propagation characteristics in the following sections are investigated by modal attenuation constant and phase velocity.

4.3 An overhead line

Figure 4.1 illustrates a single overhead conductor investigated in this section. The conductor resistivity is $\rho_c = 1.68\times10^{-8}\,\Omega$m. The earth resistivity and permittivity are ρ_e and ε_e.

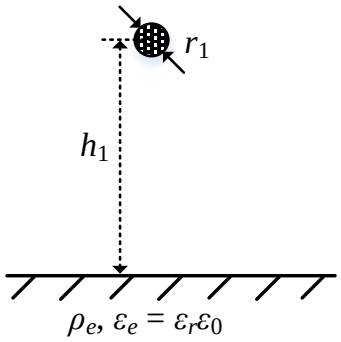

Figure 4.1: A single overhead conductor, h_1 = 10 m and r_1 = 1 cm

4.3.1 Series impedance

Figure 4.2 shows calculated results of the series impedance of a single overhead conductor by the extended TL approach. The influence of earth parameters is clearly observed. The resistance increases monotonously as frequency increases. A saturated behavior of the resistance is observed in high frequencies if a large earth permittivity is used such as $\varepsilon_r = 20$. This is caused by displacement currents in the earth. Also, a large earth resistivity increases the resistance in high frequencies.

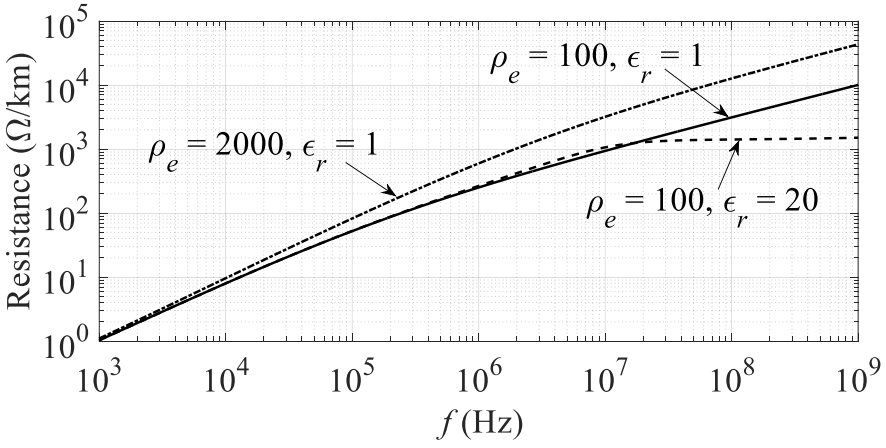

(a) Resistance

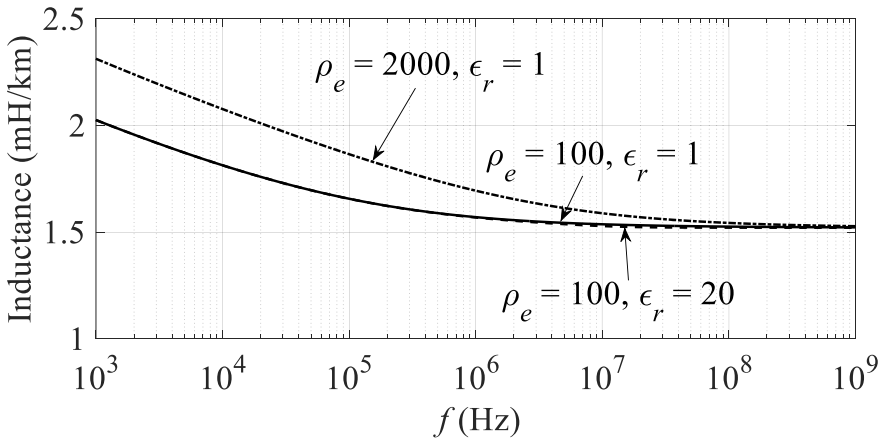

(b) Inductance

Figure 4.2: Series impedance of the conductor illustrated in Figure 4.1 by the extended TL approach

Moreover, the earth permittivity has a negligible effect on the inductance in the whole frequency range. Similarly to the resistance, the earth resistivity shows a significant influence on the inductance.

Figure 4.3 shows a comparison of the impedance between the extended and classical approaches. No difference is observed between the extended and classical TL approaches for $\varepsilon_r = 1$. It is well-known that the earth-return impedance of the classical approach is the same as the extended TL approach for $\varepsilon_r = 1$ [25].

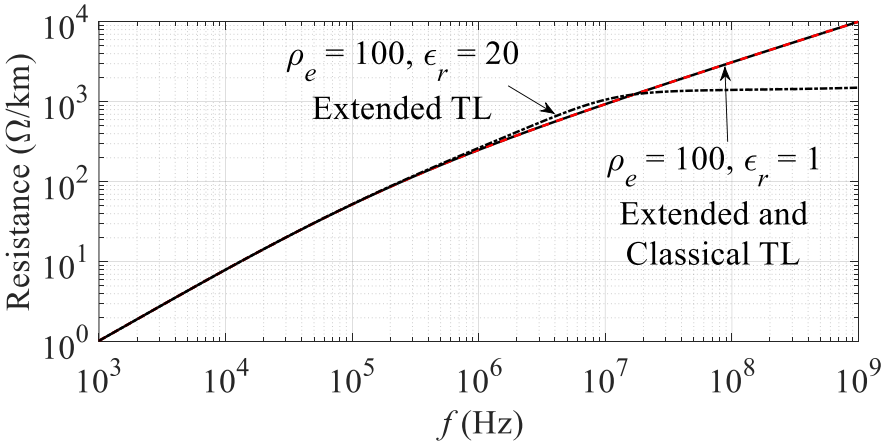

(a) Resistance

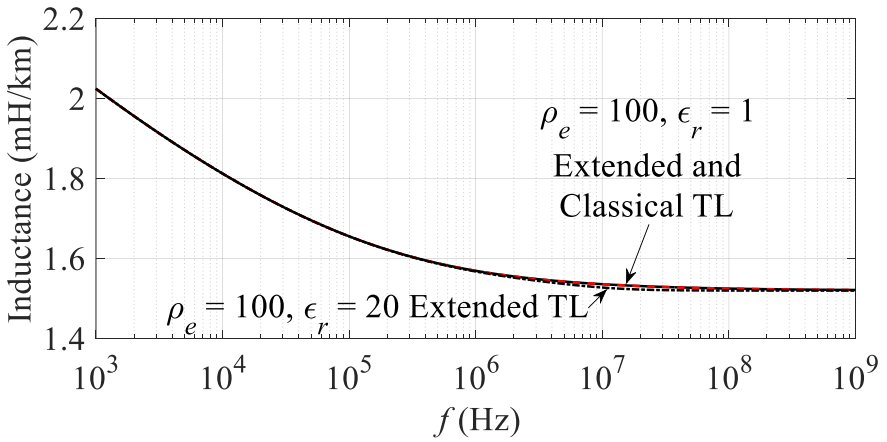

(b) Inductance

Figure 4.3: Series impedance of the conductor illustrated in Figure 4.1 by the extended and classical TL approaches

4.3.2 Numerical instability of MoM-SO and solution

Figure 4.4 shows the series impedance of the conductor illustrated in Figure 4.1 calculated by original MoM-SO [66], [67] corresponding to (2.60), improved MoM-SO with (2.59) and the extended TL approach. It is apparent that a numerical instability is observed in the results calculated by the original MoM-SO above several hundreds of kHz. The reason for this is due to the uniform current assumption adopted in the Green function of the earth-return path. The two Bessel functions in (2.60) cause the unstable numerical values at high frequencies.

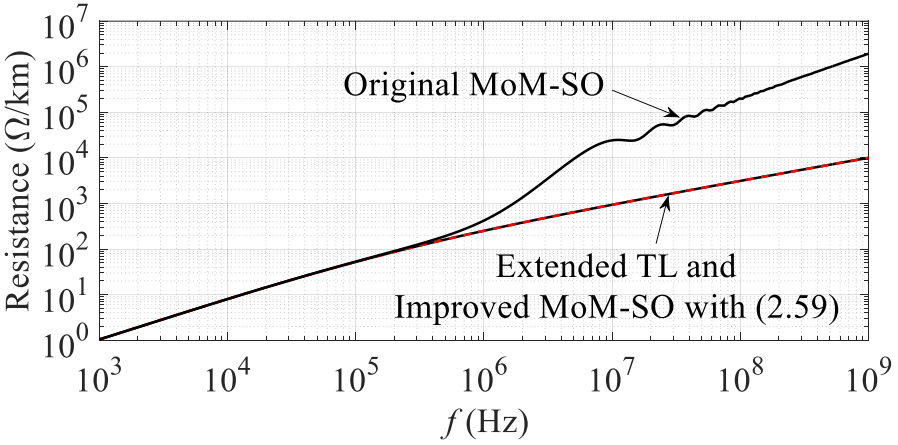

(a) Resistance

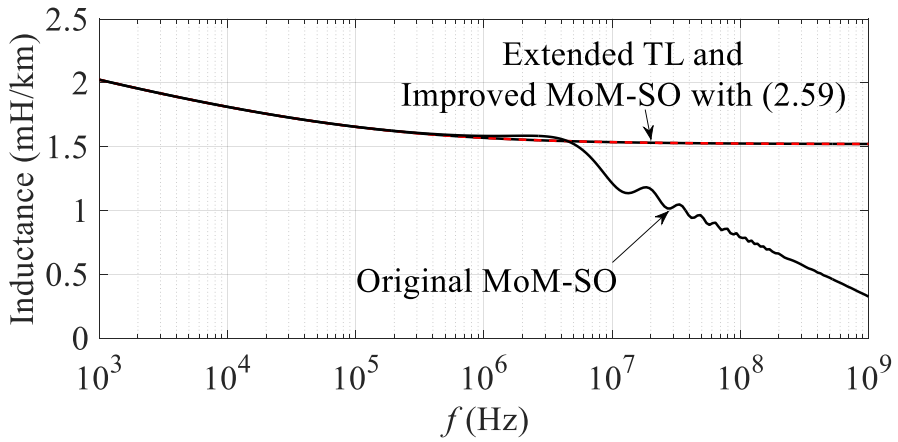

(b) Inductance

Figure 4.4: Series impedance of the conductor illustrated in Figure 4.1 by the extended TL approach and MoM-SO, ρ_e = 100 Ωm and ε_r = 1

Further as shown in Figure 4.4, the results of the improved MoM-SO with (2.59) agree very well with those by the extended TL approach. Therefore, the quasi-TEM based Green function (2.59) should be adopted to model an overhead line or an overhead cable to avoid the instability in the original MoM-SO.

4.3.3 Shunt admittance

The conductance and capacitance of the shunt admittance in Figure 4.1 are shown in Figure 4.5 for various earth resistivities and permittivities. The earth permittivity shows less influence on the admittance in the entire frequency region. The admittance is more sensitive to the earth resistivity.

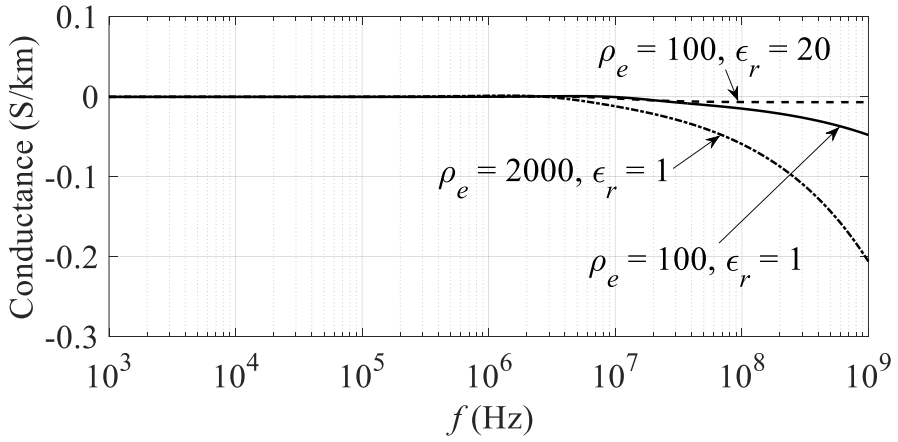

(a) Conductance

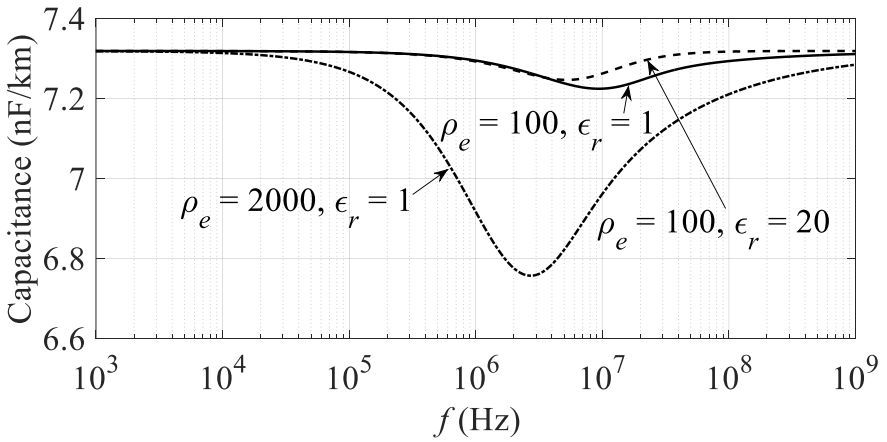

(b) Capacitance

Figure 4.5: Shunt admittance of the conductor illustrated in Figure 4.1 by the extended TL approaches

Figure 4.6 shows a comparison of the shunt admittance between the extended and classical TL approaches. It is recalled that the potential coefficient in the classical TL approach is a real constant, i.e. the admittance is purely capacitive. Thus, no frequency-dependent characteristic of the shunt admittance appears in the classical TL approach. The influence of a lossy earth correction term of (2.47) in a high frequency region on the propagation function calculated by the extended TL approach is significantly different from that calculated by the classical TL approach.

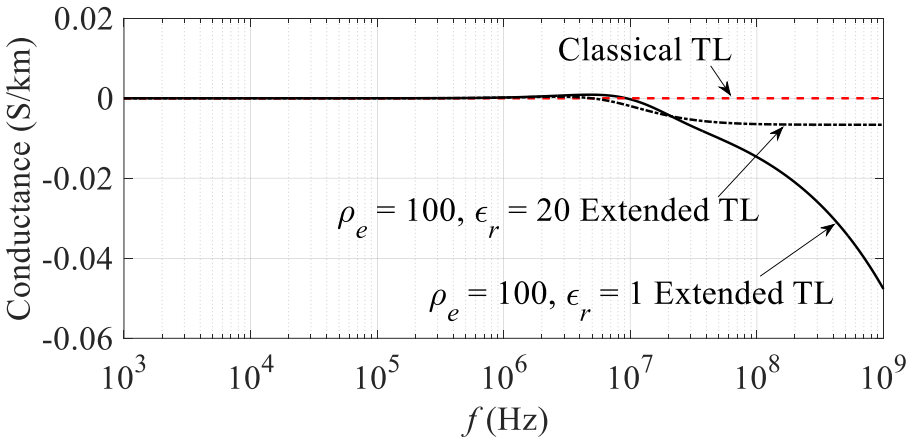

(a) Conductance

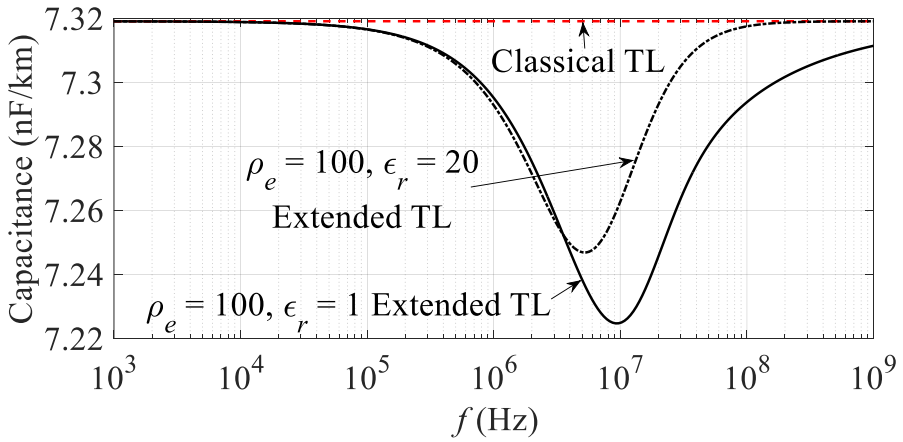

(b) Capacitance

Figure 4.6: Shunt admittance of the conductor illustrated in Figure 4.1 by the extended and classical TL approaches

4.3.4 Attenuation constant

Figure 4.7 and Figure 4.8 show the frequency responses of the attenuation constant for the overhead conductor illustrated in Figure 4.1. In Figure 4.7, the attenuation constant is calculated by extended TL approach, considering three different earth parameters. The earth permittivity has a minor influence on the attenuation constant in the entire frequency range. Also, a significant influence due to a large earth resistivity is observed.

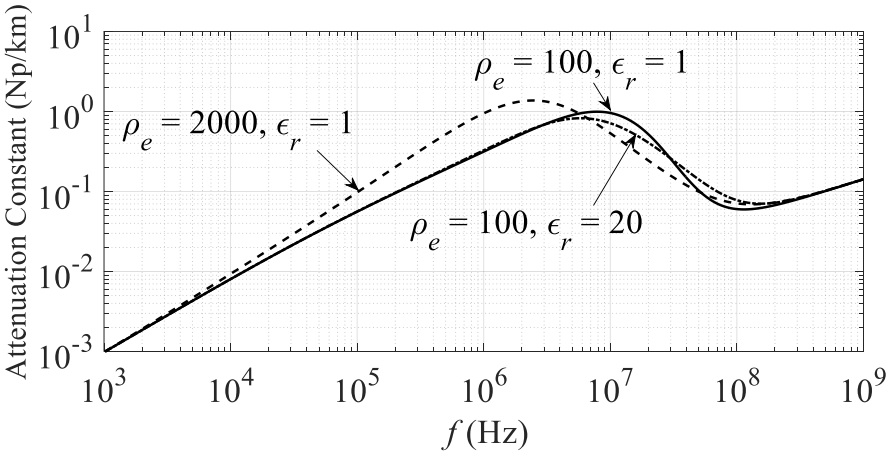

Figure 4.7: Attenuation constant of the conductor illustrated in Figure 4.1 by the extended TL approach

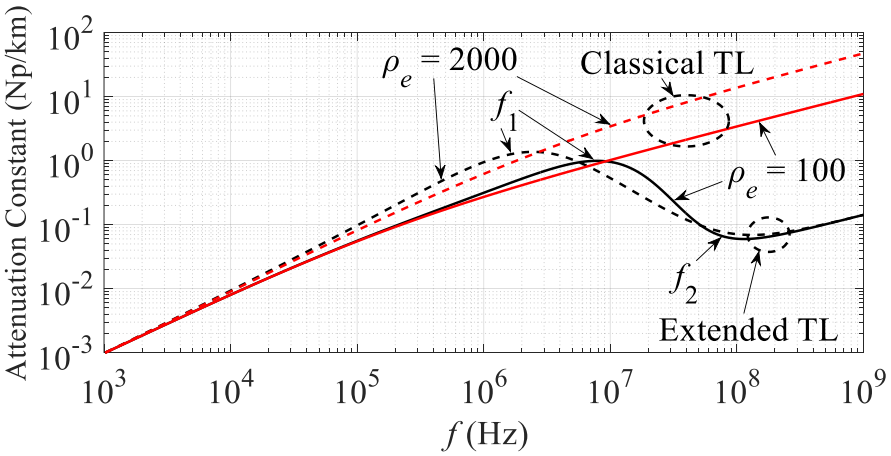

Figure 4.8: Attenuation constant of the conductor illustrated in Figure 4.1 by the extended and classical TL approaches, ε_r = 1

The attenuation calculated by the classical TL approach in Figure 4.8 monotonously increases as a function of frequency. On the contrary, the extended approach shows that the attenuation starts to decrease at the frequency f_1, and increases again monotonously after the frequency f_2. This phenomenon is referred to as "mode transition" by Kikuchi [28], [29]. Later, Chiba [93] presented an experimental validation of the Kikuchi's theory. The attenuation in frequencies lower than f_1 is related to the low frequency quasi-TEM (earth-return wave) propagation. Olsen described it as "strictly speaking the earth-return wave is a TM mode with a very small axial electric field component" [8]. In the frequency region up to f_1, the classical TL approach agrees with the extended TL approach. For frequencies higher than f_1, the propagation mode changes from the quasi-TEM propagation, and reaches the Sommerfeld-Goubau (surface wave) propagation at the frequency f_2 [26], [28], [29], . The surface wave is a result of large displacement currents which represent the return current in air nearby the conductor. The displacement currents are generated by high electric field strength at the conductor surface [8], [94]. It is also interpreted physically that the earth shows a capacitive nature at high frequencies, while it is inductive at low frequencies [8], [94]. This phenomenon cannot be explained by the classical TL approach. In Figure 4.7 and Figure 4.8, only the TL mode is calculated by the iteration of modal equation as shown in [28], [29]. In [37], it is shown that the frequency spectra of the TL and FW or SA modes are much closed to each other until a break-point where two different branches appear. Above the frequency of this break-point, the attenuation constants of the TL and FW modes are respectively decreasing and increasing

as frequency increases. The TL mode approaches to zero if the conductor is perfectly conducting. If the conductor is lossy, the TL mode decreases to a critical frequency f_2 and then increases again, and eventually it reaches the Sommerfeld-Goubau propagation wave. The attenuation constant of the FW mode approaches infinite. Therefore, the TL mode can be regarded as the dominant one for the wave propagation with finite attenuation constant even in the high frequency region [37]. It should be noted that the attenuation at frequencies higher than f_2 is significantly smaller than that at frequencies lower than f_1. The reason for the lower attenuation is that the dominant cause of the attenuation in this region is the conductor internal impedance which is much smaller than the earth-return impedance [26].

4.3.5 Calculated results of electromagnetic field components

The formulas of $\mathbf{E}_0$ and $\mathbf{H}_0$ have been derived and given in (2.37) based on the complete field solutions shown in Section 2.1.

The basic characteristics of axial and vertical electric field components of the conductor illustrated in Figure 4.1 have been already investigated in [36] for an earth resistivity $\rho_e = 200\,\Omega\text{m}$ and relative permittivity $\varepsilon_r = 1$. Considering the same parameters, the calculated field components are identical to those in [36]. This section focuses on the high frequency characteristics of both $\mathbf{E}_0$ and $\mathbf{H}_0$ with various earth resistivities and permittivities to observe the mode transition described in Section 4.3.4.

4.3.5.1 High-frequency characteristics of E_{0x}, E_{0z} and H_{0y}

Figure 4.1 illustrates a single overhead conductor investigated in this section and the rectangular coordinate is referred to Figure 2.1.

Figure 4.9 shows (a) axial E_{0x}, (b) vertical E_{0z} and (c) horizontal H_{0y} field components in the air as a function of frequency. In each figure, one group of curves corresponds to a vertical distance z from the earth surface being 9.99 m, i.e. at the conductor surface. The other group corresponds to $z = 0.01\text{m}$, i.e. 1 cm from the earth surface. Also, included in the figure are the cases of (1) $\rho_e = 100\,\Omega\text{m},\ \varepsilon_r = 1$, (2) $\rho_e = 100\,\Omega\text{m},\ \varepsilon_r = 20$ and (3) $\rho_e = 2000\,\Omega\text{m},\ \varepsilon_r = 1$.

It is clear in Figure 4.9 (b) and (c) that E_{0z} and H_{0y} at $z = 9.99\,\text{m}$, i.e. at the conductor surface, are almost independent of the frequency, i.e. $E_{0z} \approx 7000\,\text{V/m}$ and $H_{0y} = 16\,\text{A/m}$. At $z = 0.01\,\text{m}$, E_{0z} and H_{0y} are nearly constant or little increasing up to $f = 4\,\text{MHz}$ in the case of $\rho_e = 100\,\Omega\text{m}$, and up to $f = 1\,\text{MHz}$ in the case of $\rho_e = 2000\,\Omega\text{m}$. Then, those field components start to decrease as frequency increases, because the earth becomes less influential at high frequencies where the surface wave becomes dominant, as will be explained later for E_{0x}.

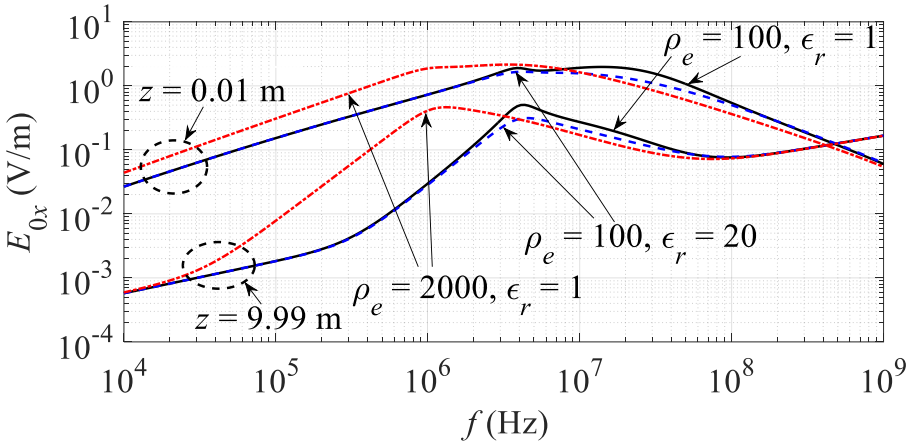

(a) Axial electric field

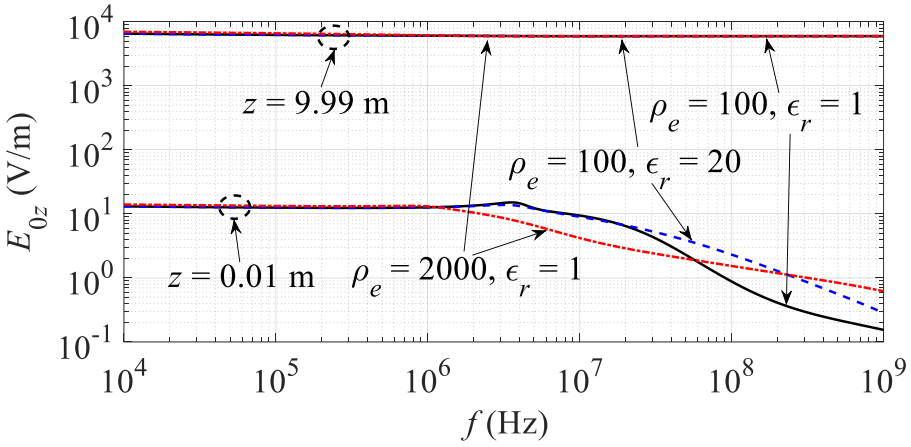

(b) Vertical electric field

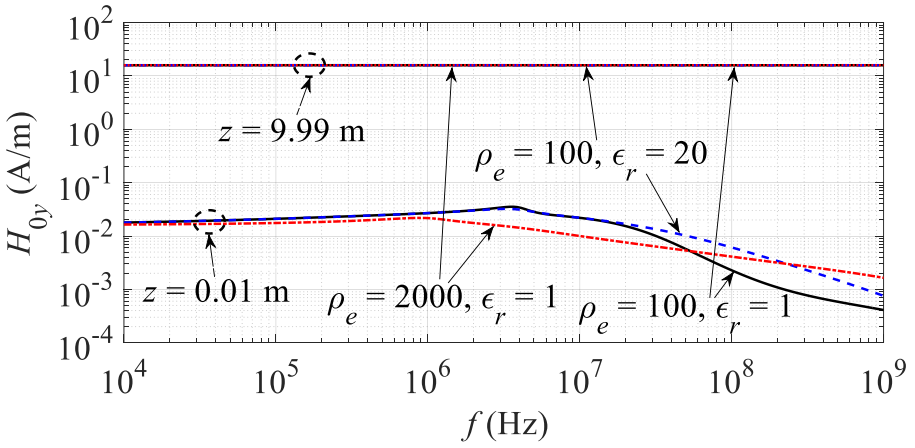

(c) Horizontal magnetic field

Figure 4.9: Frequency responses of electromagnetic field components in the air, y = 0 m

No noticeable difference is observed between $\varepsilon_r = 1$ and 20 with $\rho_e = 100\,\Omega$m up to 20 MHz. E_{0z} and H_{0y} in the case of $\varepsilon_r = 20$ become greater than those in the case of $\varepsilon_r = 1$. For $\rho_e = 2000\,\Omega$m, E_{0z} is slightly greater than that for $\rho_e = 100\,\Omega$m up to about 1 MHz. E_{0z} becomes smaller up to 50 MHz. Above this frequency, E_{0z} for $\rho_e = 2000\,\Omega$m is greater than that for $\rho_e = 100\,\Omega$m. H_{0y} for $\rho_e = 2000\,\Omega$m is smaller up to 50 MHz, and becomes greater than that for $\rho_e = 100\,\Omega$m.

The axial electric field E_{0x} shows a more complicated behavior than those of E_{0z} and H_{0y}. It should be noted that E_{0x} is far smaller than E_{0z} especially at the conductor surface ($z = 9.99$ m). E_{0x} for $\rho_e = 2000\,\Omega$m is greater than that for $\rho_e = 100\,\Omega$m up to frequencies of some MHz. Then, it becomes smaller. E_{0x} with $\varepsilon_r = 20$ is always smaller than that with $\varepsilon_r = 1$, even though the difference is quite small. However, when frequency becomes very high, above 100 MHz, no significant difference is observed between various ρ_e and ε_r. This fact indicates that the earth causes no significant effect on the axial electric field, and corresponds to the surface wave propagation explained in Section 4.3.4. In fact, E_{0x} near the earth surface becomes smaller than that at the conductor surface above 300 MHz.

Moreover, E_{0x} increases as frequency increases up to some MHz. Then, E_{0x} at the earth surface decreases as frequency increases. E_{0x} at the conductor surface decreases up to a frequency of about

80 MHz. Then, it increases again. This characteristic is very similar to that of attenuation constant as shown in Figure 4.10, attenuation constant and E_{0x} are shown in the same plot for an easy observation of the correlation for the same conductor geometry and earth electrical parameters. It should be noted that E_{0x} on the conductor surface at various positions, for example, ($z = 9.99\,\text{m}$, $y = 0\,\text{m}$), ($z = 10.01\,\text{m}$, $y = 0\,\text{m}$) and ($z = 9.9929\,\text{m}$, $y = 0.00707\,\text{m}$) is the same.

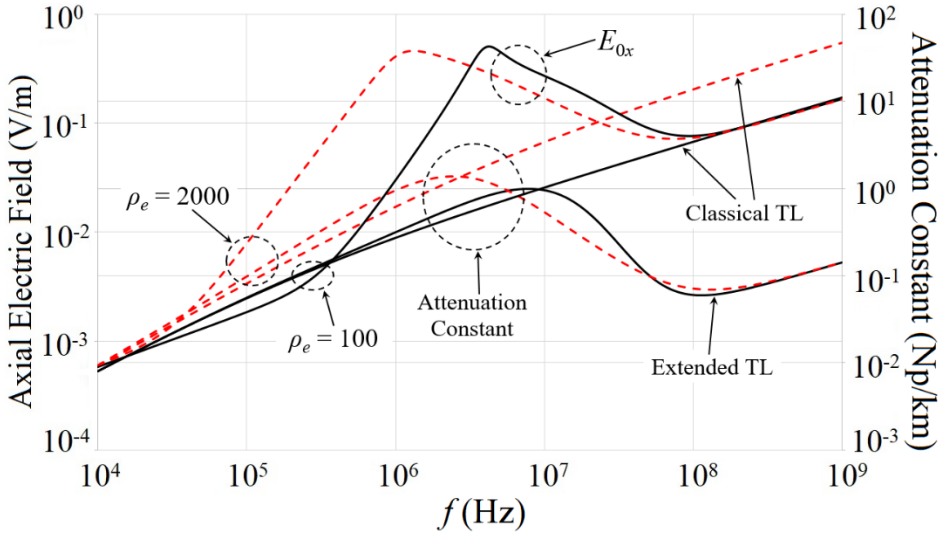

Figure 4.10: Frequency responses of attenuation constant and axial electric field component by the extended and classical TL approaches

4.3.5.2 Comparison with classical TL approach

Based on the classical TL approach with well-known Pollaczek's earth-return impedance and the space admittance, the attenuation is calculated and the result is shown in Figure 4.10. As is explained in Section 4.3.4, the attenuation constant by the classical TL approach is a monotonously increasing function of frequency and shows no mode transition.

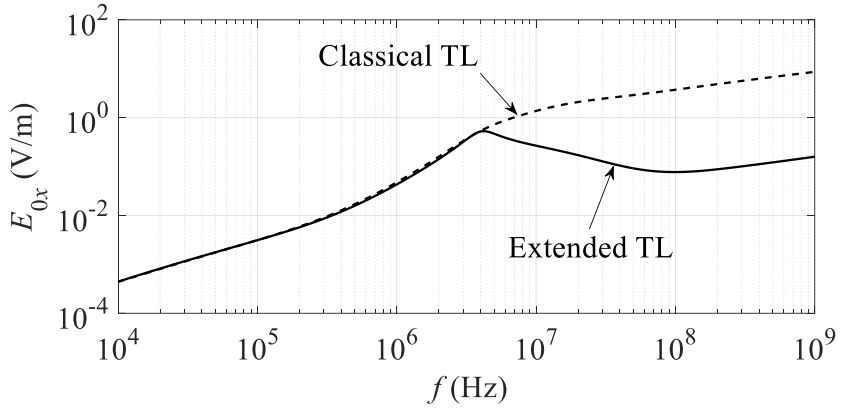

(a) Axial electric field

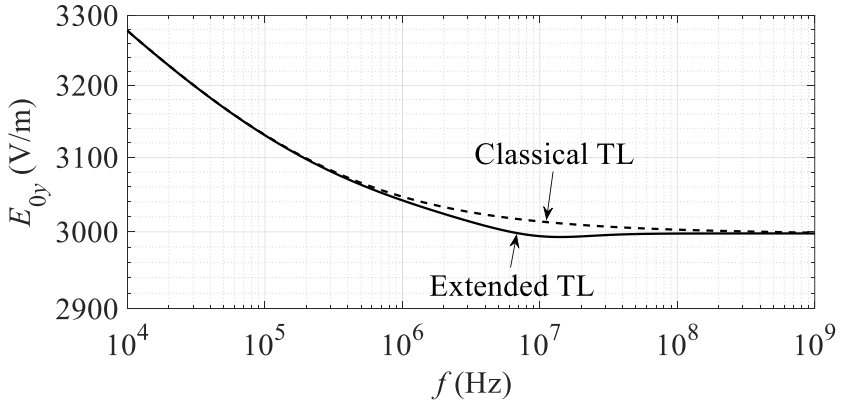

(b) Horizontal electric field

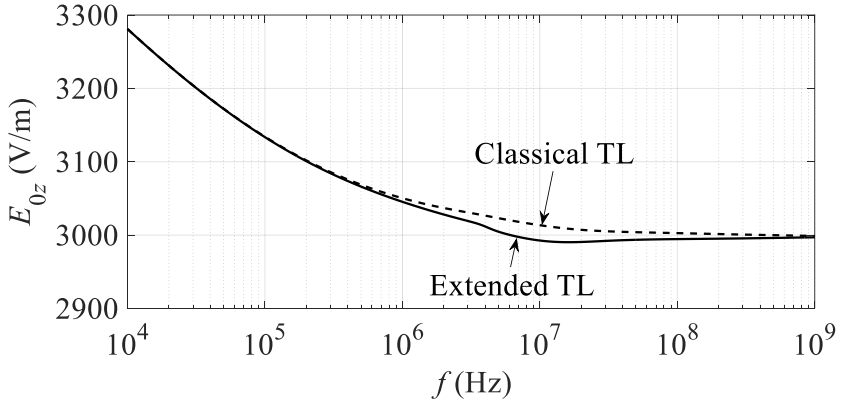

(c) Vertical electric field

Figure 4.11: Comparison of electric field components at the conductor surface by the extended and classical TL approaches at z = 9.99 m and y = 0.01 m, ρ_e = 100 Ωm, ε_r = 1

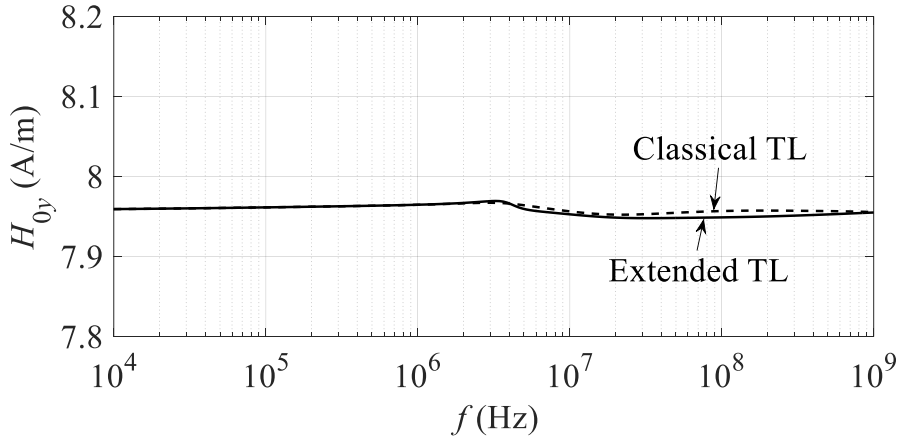

Figure 4.12: Comparison of horizontal magnetic field component by the extended and classical TL approaches at z = 9.99 m and y = 0.01 m, ρ_e = 100 Ωm, ε_r = 1

Figure 4.11 and Figure 4.12 show a comparison of electromagnetic field components evaluated by the extended and classical TL approaches. At low frequencies, the wave propagation on an overhead conductor above a lossy earth is a quasi-TEM mode and no noticeable difference between the classical TL approach and the complete field solution can be observed. However, above a frequency of about 5 MHz, a noticeable difference for E_{0x} is observed. E_{0x} calculated by the classical TL approach shows a monotonous increase as a function of frequency in Figure 4.11 (a), similarly to the monotonously increasing attenuation constant in Figure 4.10, while E_{0x} evaluated by the complete field solution shows mode transition as already explained in Section 4.3.5.1.

4.3.5.3 Discussions

In references [8], [94], Olsen stated that even a quasi-TEM mode of wave propagation at low frequencies contains a small axial field component and thus it is, strictly speaking, a TM mode with a small E_{0x} at the conductor surface. This statement is confirmed in Figure 4.9 (a) which shows non-zero values for E_{0x} even in the low frequency region, corresponding to the ohmic losses in the conductor. As the frequency increases, E_{0x} at the conductor surface shows the mode transition as already described in Section 4.3.5.1.

4.4 An overhead cable

The frequency characteristics of the earth-return impedance, admittance and wave propagation of an overhead conductor have been investigated in Section 4.3. This section focuses on mode transition from a low frequency TEM mode to high frequency Sommerfeld-Goubau propagation and associated propagation functions for a 500 kV GIB. The GIB is a typical overhead cable and the one illustrated in Figure 4.13 is used as an example in this section [95].

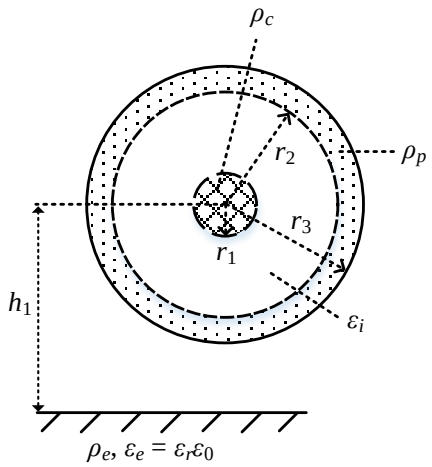

Figure 4.13: Cross-section of a 500 kV GIB, h_1 = 2.45 m, r_1 = 12.5 cm, r_2 = 46 cm, r_3 = 48 cm, ρ_c = 1.68×10^{-8} Ωm, ρ_p = 2.82×10^{-8} Ωm and SF6 gas ε_i = 1

4.4.1 Attenuation constant

Figure 4.14 shows the frequency response of the modal attenuation constants for the GIB illustrated in Figure 4.13. No difference of the coaxial mode between the extended and classical TL approaches is observed, as expected. The earth-return mode calculated by the extended TL approach shows the mode transition as explained in Section 4.3.4. However, the result by the classical TL approach increases monotonously.

It should be noted that the applicable range of the extended approach is about 100 MHz, because of the relation between the wavelength and the pipe radius. However, in order to show the mode transition clearly, the attenuation is given up to 10 GHz in Figure 4.14 and Figure 4.15.

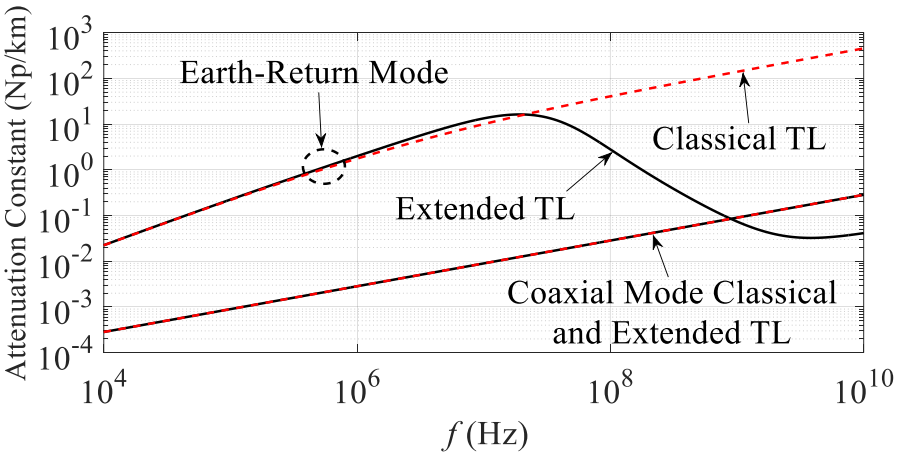

Figure 4.14: Modal attenuation constants of the GIB illustrated in Figure 4.13 by the extended and classical TL approaches, ρ_e = 100 Ωm and ε_r = 1

4.4.2 Propagation function

Figure 4.15 shows the earth-return mode propagation function H_w which is defined as:

$$H_w = e^{-\alpha_1 x} \tag{4.9}$$

where x is the distance along the conductor and α_1 is the earth-return mode attenuation constant.

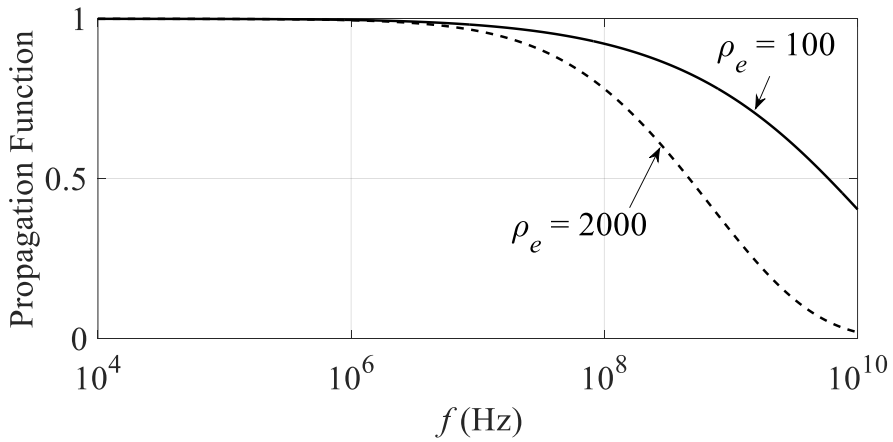

(a) Classical TL

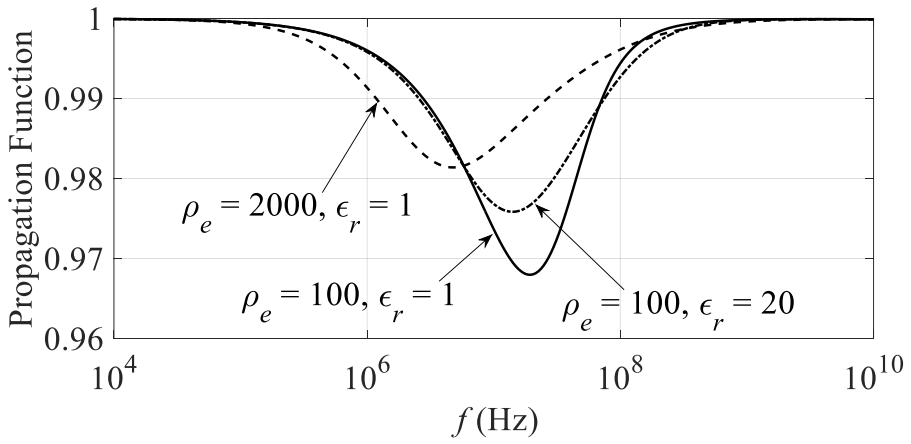

(b) Extended TL

Figure 4.15: Earth-return mode propagation function on the GIB illustrated in Figure 4.13 at distance x = 2 m from the sending end by the extended and classical TL approaches

It is clear from Figure 4.15 (a) that H_w monotonously decreases as the frequency increases in the classical TL approach, following the characteristic of the earth-return mode propagation constant in Figure 4.14. With the more accurate extended TL approach, H_w decreases until the frequency up to f_1. Then it increases until the frequency reaches f_2. f_1 and f_2 are explained in Section 4.3.4. Because of lower attenuation in the frequency region higher than f_1 as in Figure 4.14, H_w in the extended TL approach is much greater than that in the classical TL approach.

4.4.3 Transition frequency f_1

The mode transition explained in Figure 4.14 starts at the frequency f_1. The frequency can be used as an indicator of low attenuation in high frequency switching surges in a GIS. The frequency is related to conductor height h_1, earth resistivity ρ_e and relative earth permittivity ε_r, as shown in Figure 4.13. For example, f_1 in Figure 4.16 decreases as the conductor height or earth resistivity increases.

The reason for this behavior is that the mode transition is influenced dominantly by the earth-return path. When the conductor height is small, the influence of the earth-return path is stronger and the earth-return wave stays dominant up to higher frequencies and thus the transition frequency becomes higher.

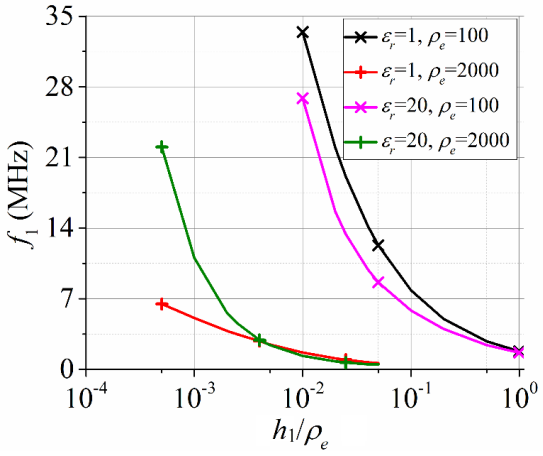

Figure 4.16: Transition frequency f_1 for the GIB illustrated in Figure 4.13

4.5 An underground cable

The wave propagation characteristics of a cable system are investigated based on different approaches and cable configurations in this section.

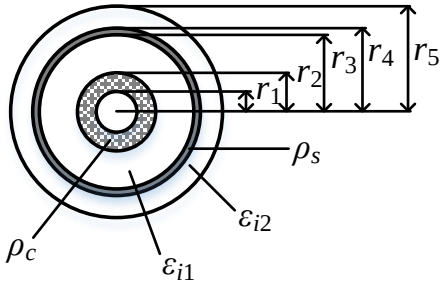

Figure 4.17: Cross-section of a single core cable

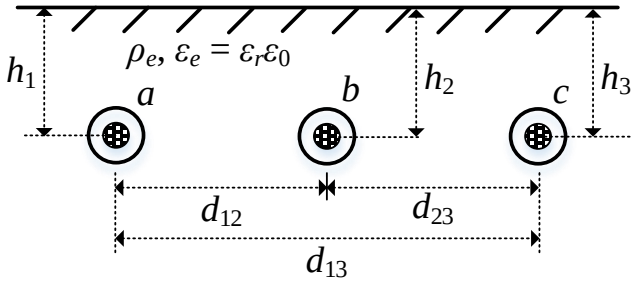

(a) Flat arrangement of Cable 1

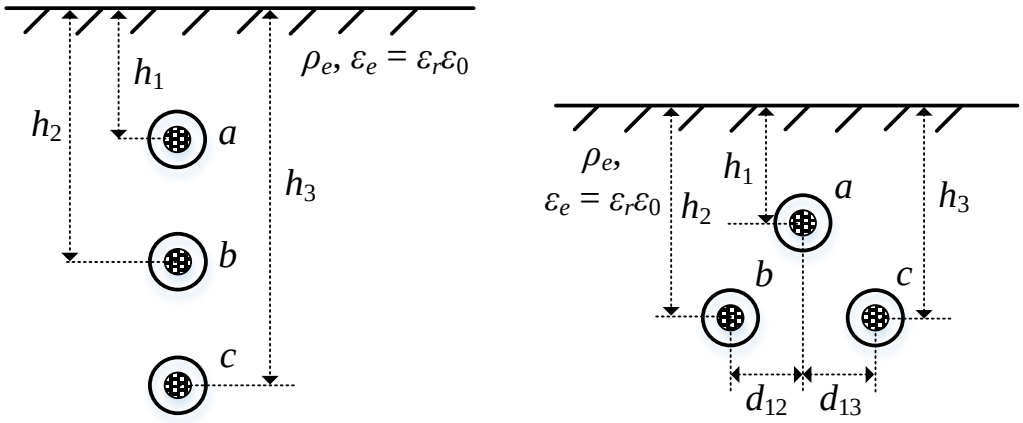

(b) Vertical arrangement of Cable 2 (c) Trefoil arrangement of Cable 3

Figure 4.18: Arrangement of three phase single core cable

The cross-section of a single core cable is shown in Figure 4.17. Three different cable arrangements are illustrated in Figure 4.18.

The parameters adopted into three cables are summarized in Table 4.2 [5], [96].

Table 4.2: Parameters of cables

	Cable 1	**Cable 2**	**Cable 3**
Voltage (kV)	132	110	150
Arrangement	Flat	Vertical	Trefoil
h_1 (m)	1	1	1.213
h_2	1	1.35	1.3
h_3	1	1.7	1.3
d_{12} (m)	0.35	0	0.05
d_{13}	0.7	0	0.05
d_{23}	0.35	0	0.1
r_1 (cm)	1.03	1.049	0
r_2	1.9	1.78	2.075
r_3	3.45	3.075	4.025
r_4	3.85	3.255	4.276
r_5	4.25	4.075	4.794
ρ_c (Ωm)	1.7×10^{-8}	1.7×10^{-8}	3.19×10^{-8}
ρ_s	2.1×10^{-7}	2.1×10^{-7}	2.228×10^{-7}
ε_{i1}	3.5	3.5	2.68
ε_{i2}	4	4	2.3

4.5.1 Series impedance

Cable 1 shown in Figure 4.17 and Figure 4.18 (a) is used to calculate the series impedance (4.3).

4.5.1.1 Self-impedance of phase - *a* sheath

Figure 4.19 shows the calculated series impedance of phase - *a* sheath by the extended TL approach. The earth resistivity and permittivity have minor influence on the resistance in high frequencies. However, a clear difference of the inductance is observed between $\rho_e = 100$ and $\rho_e = 500\,\Omega$m. Also, the earth permittivity shows minor influence on the inductance in high frequencies.

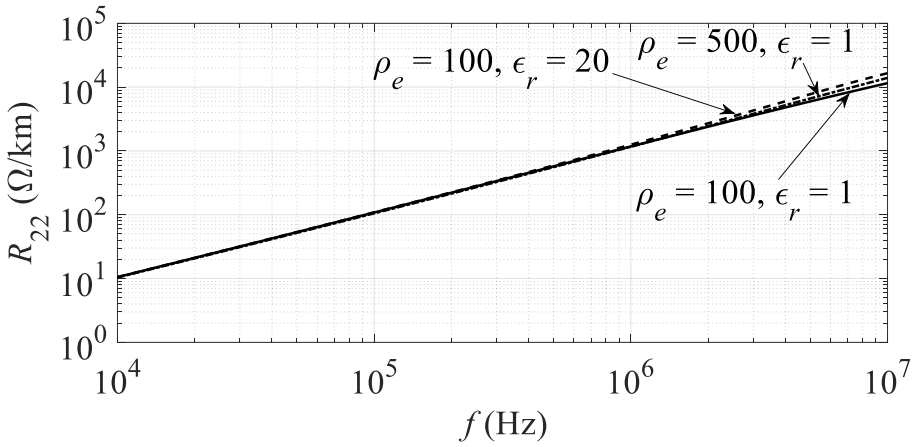

(a) Self-resistance

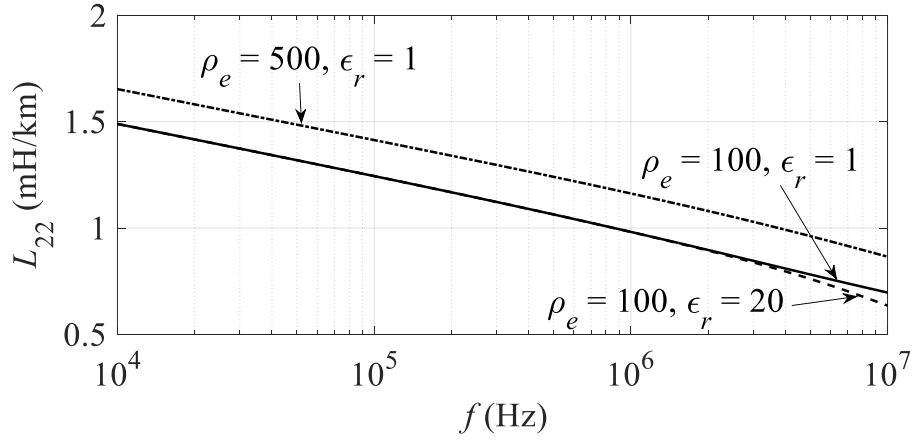

(b) Self-inductance

Figure 4.19: Self-impedance of phase - *a* sheath by the extended TL approach

The calculated series impedance of phase - *a* sheath is compared in Figure 4.20 by the extended TL approach, (3.88), MoM-SO and classical TL approach. It is clear that the results by MoM-SO agree very well with the results by the extended TL approach. No significant difference is observed at low frequency between all the methods, i.e. $f \leq 1\text{MHz}$.

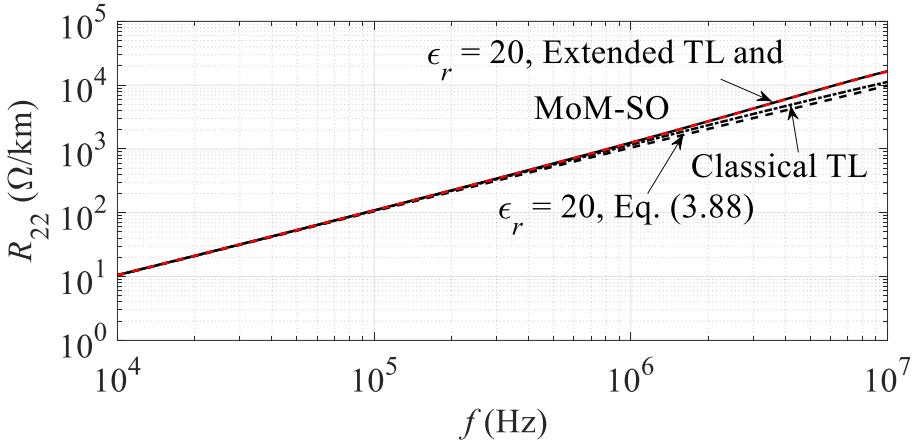

(a) Self-resistance

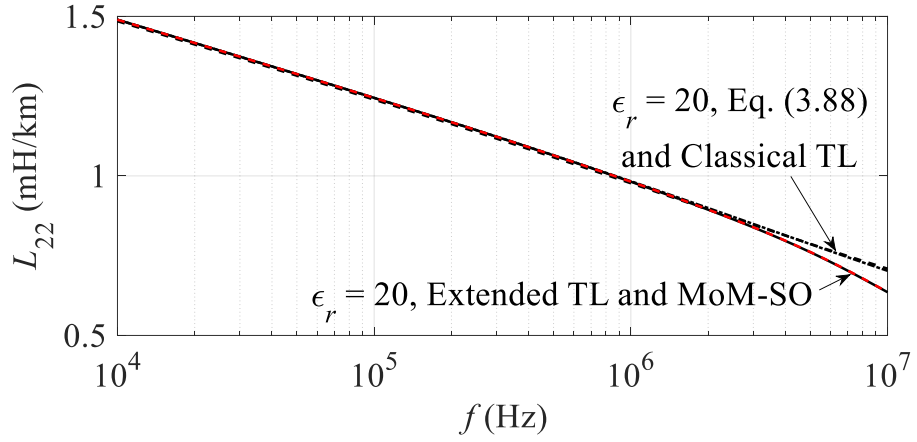

(b) Self-inductance

Figure 4.20: Self-impedance of phase - *a* sheath, ρ_e = 100 Ωm

4.5.1.2 Mutual impedance between phase - *a* and phase - *b* sheaths

Similarly to self-impedance, the earth permittivity causes a minor effect on the mutual impedance in high frequencies as shown in Figure 4.21. The earth resistivity shows a significant influence on the inductance.

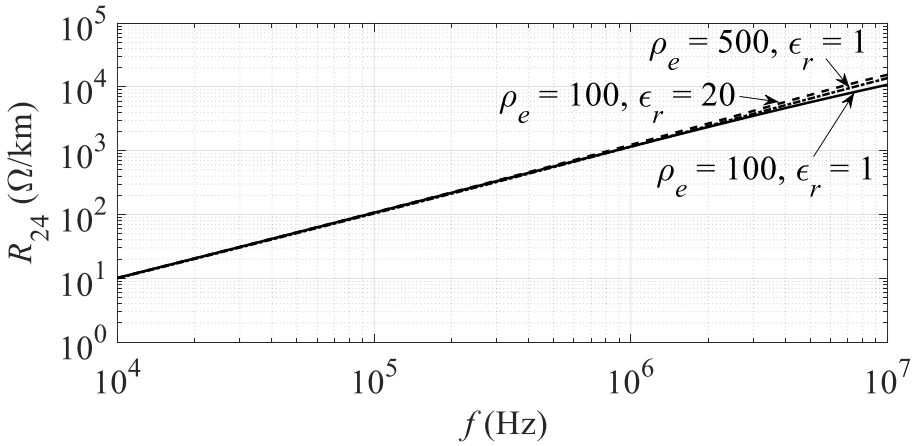

(a) Mutual resistance

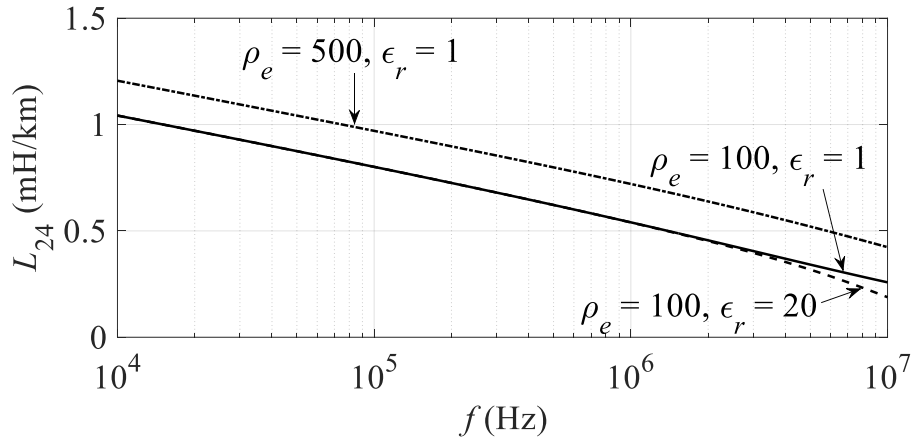

(b) Mutual inductance

Figure 4.21: Mutual impedance between phase - *a* and phase - *b* sheaths by the extended TL approach

As shown in Figure 4.22, only a minor difference is observed between different formulas in high frequencies. MoM-SO also agrees very well with the extended TL approach.

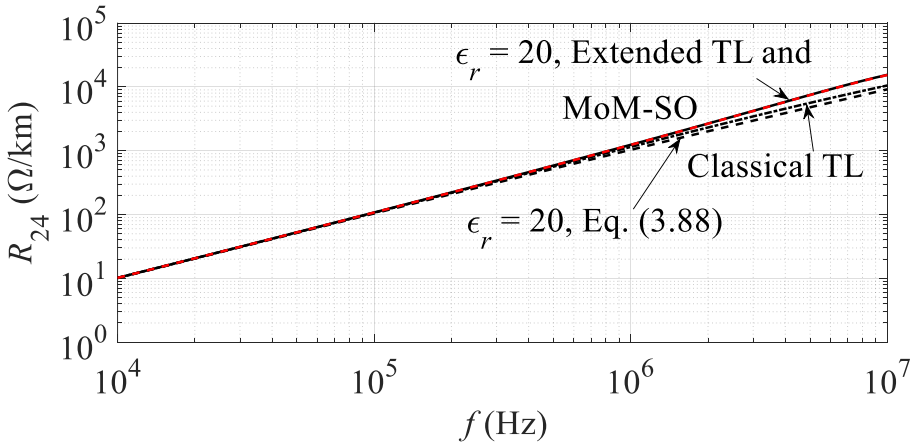

(a) Mutual resistance

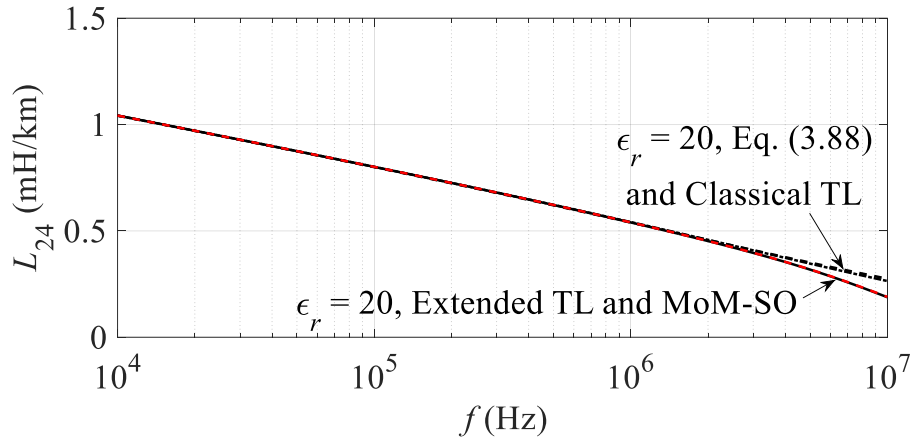

(b) Mutual inductance

Figure 4.22: Mutual impedance between phase - *a* and phase - *b* sheaths, ρ_e = 100 Ωm

4.5.2 Shunt admittance

The shunt admittance matrix (4.4) of Cable 1 is calculated and the configuration is shown in Figure 4.17 and Figure 4.18 (a).

4.5.2.1 Self-admittance of phase - *a* sheath

The self-admittance of phase - *a* sheath is calculated and shown in Figure 4.23 and Figure 4.24. The earth resistivity has more significant influence on shunt admittance than earth permittivity. By adopting the earth-return admittance, the conductance increases monotonously at high frequency. Capacitance is nearly the same as the insulator capacitance in a low frequency and it decreases as

frequency increases. The classical TL approach shows no frequency-dependent characteristics of admittance, and it is because only the insulator admittance has been adopted in (4.4). The difference between extended TL approach and (3.89) comes from the different methods of formulations.

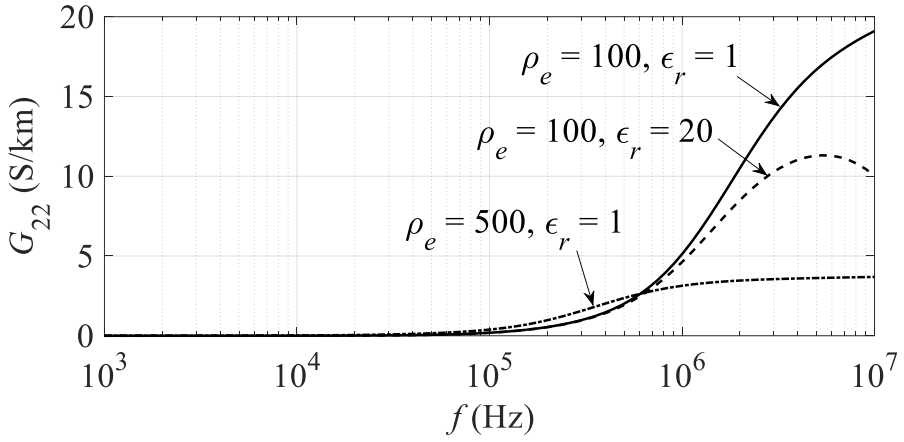

(a) Self-conductance

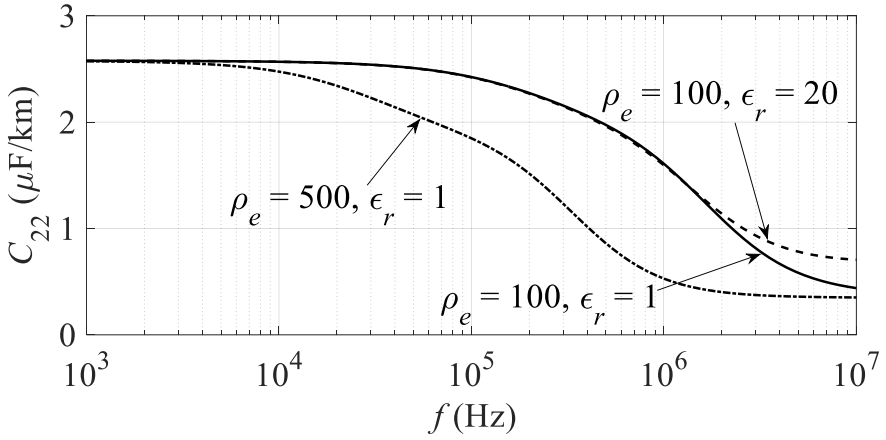

(b) Self-capacitance

Figure 4.23: Self-admittance of phase - *a* sheath by the extended TL approach

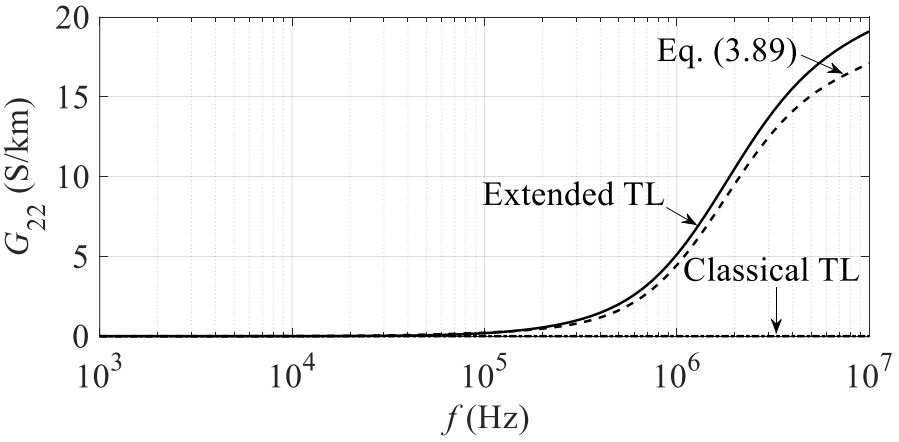

(a) Self-conductance

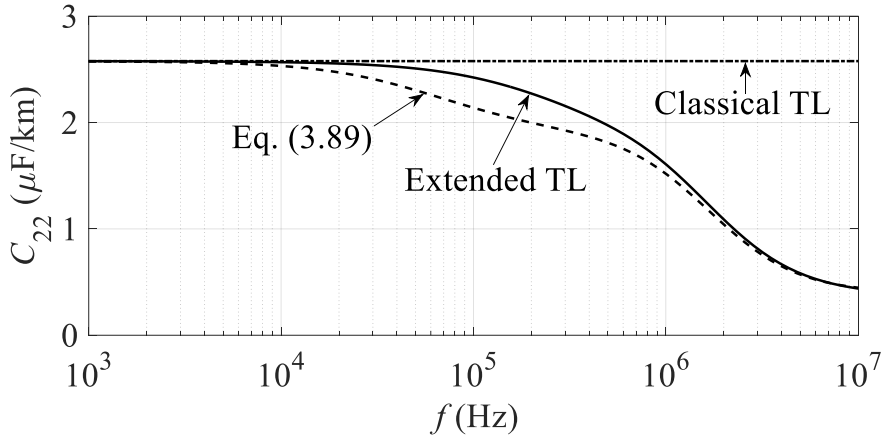

(b) Self-capacitance

Figure 4.24: Self-admittance of phase - *a* sheath, ρ_e = 100 Ωm and ε_r = 1

4.5.2.2 Mutual admittance between phase - *a* and phase - *b* sheaths

The mutual admittances between phase - *a* and phase - *b* sheaths are calculated and shown in Figure 4.25 and Figure 4.26. Similarly to the self-admittance of phase - *a* sheath, the mutual admittance is more sensitive to earth resistivity than earth permittivity. Again, the frequency-dependent characteristics of mutual admittance have been observed in high frequencies if the earth-return admittance is considered. A more noticeable difference is observed between the extended TL approach and (3.89). The classical TL approach deals with no mutual admittance as is well-known [2]-[5].

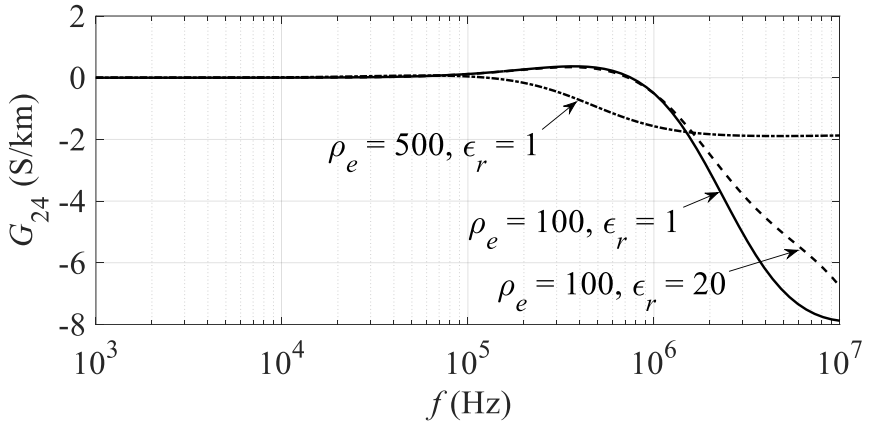

(a) Mutual conductance

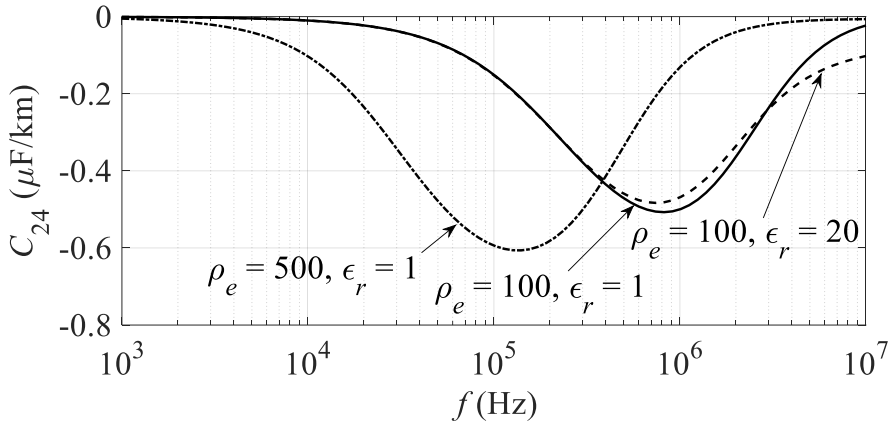

(b) Mutual capacitance

Figure 4.25: Mutual admittance between phase - *a* and phase - *b* sheaths by the extended TL approach

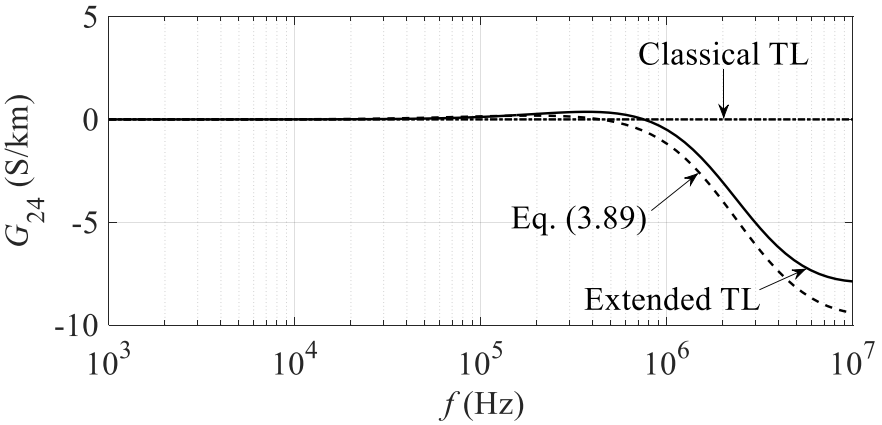

(a) Mutual conductance

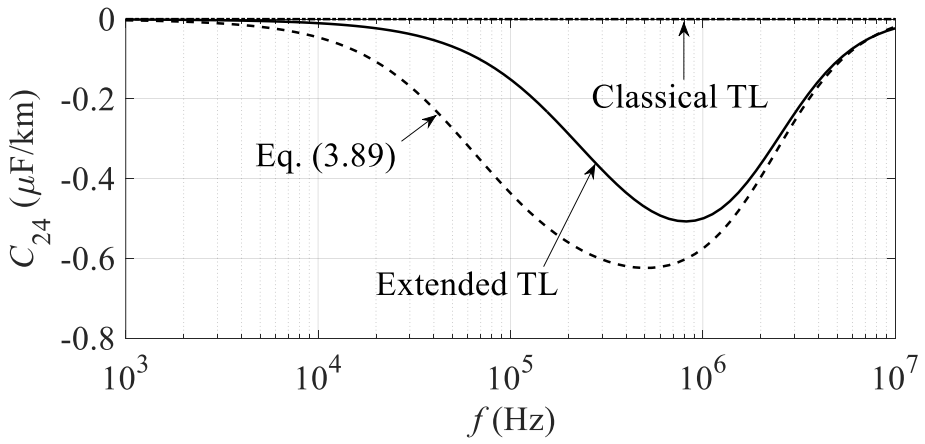

(b) Mutual capacitance

Figure 4.26: Mutual admittance between phase - *a* and phase - *b* sheaths, ρ_e = 100 Ωm and ε_r = 1

4.5.2.3 Influence of integral reference h_r

As discussed in Section 3.3.2, the quasi-TEM based earth-return potential coefficient is dependent on the integral reference h_r in (3.36). Figure 4.27 and Figure 4.28 show the calculated self and mutual admittances by adopting different earth-return potential coefficient formulas in (4.5). Formulas (3.72), (3.74) and (3.78) are derived under the condition of $h_r = -\infty$, $h_r = 0$ and $h_r = -\delta_e$, respectively. In addition, the cases of $h_r = -0.2$, -2 and -20 m are calculated in comparison with (3.72), (3.74) and (3.78). It should be noted that the results by (3.92) are the same as those by (3.74).

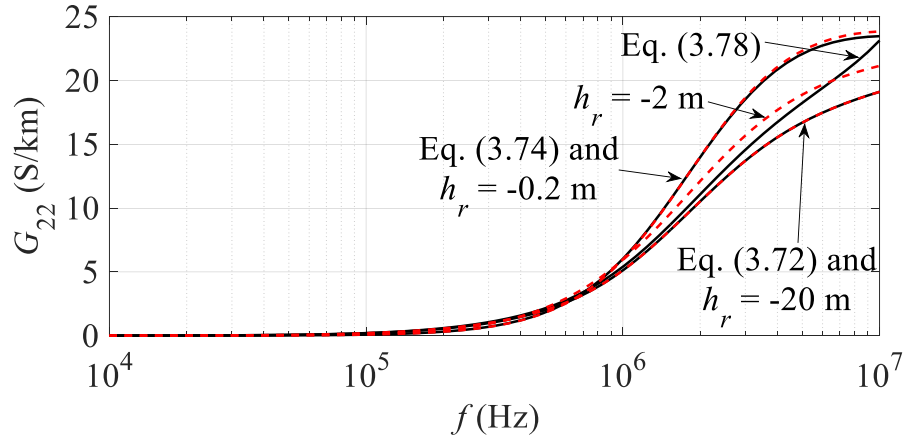

(a) Self-conductance

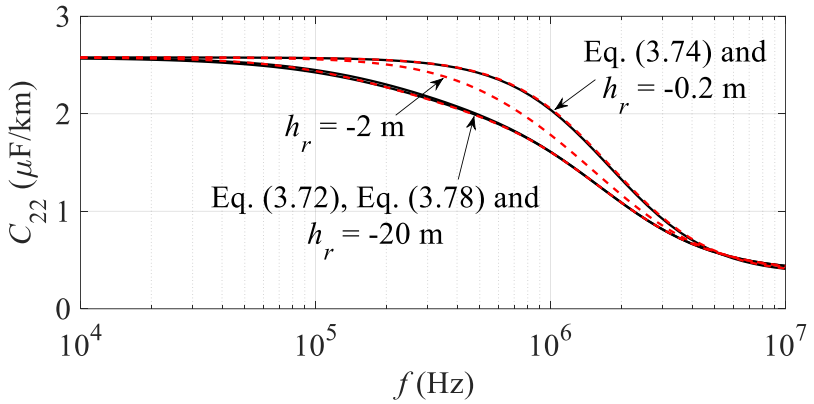

(b) Self-capacitance

Figure 4.27: Self-admittance of phase - *a* sheath, ρ_e = 100 Ωm and ε_r = 1

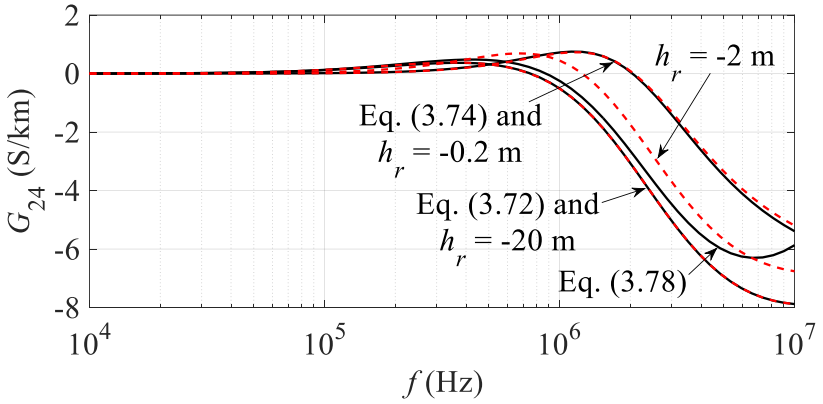

(a) Mutual conductance

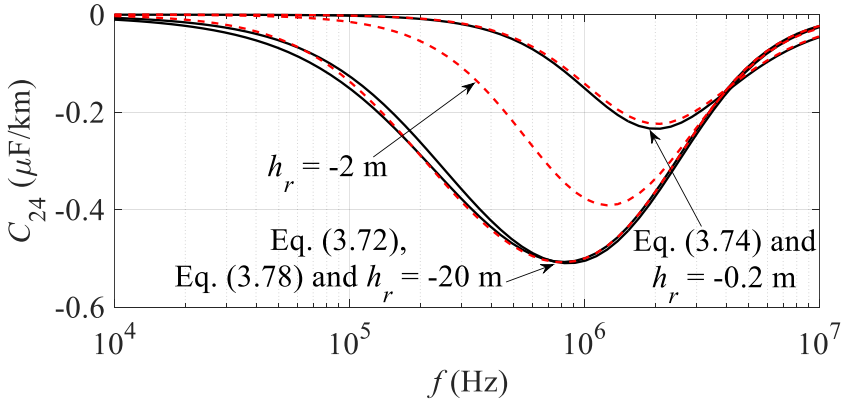

(b) Mutual capacitance

Figure 4.28: Mutual admittance between phase - *a* and phase - *b* sheaths, ρ_e = 100 Ωm and ε_r = 1

As shown in Figure 4.27 and Figure 4.28, only minor differences are observed between the proposed formulas with (3.72) and (3.78). A significant difference is observed between $h_r = 0$ and $h_r = -\infty$. This difference is explained by the penetration depth of earth in Figure 4.29. The penetration depth is ranging from 100 m to 10 m for frequencies $10\,\text{kHz} < f < 1\,\text{MHz}$. The depth is much larger than the distance between the cable and the earth surface (1 m in this case). Thus, the vertical electric field component cannot decay sufficiently at the earth surface and results in the non-negligible effect in (3.36). Moreover, it is clear that admittance converges to $h_r = -\infty$ if h_r is changed from $-0.2\,\text{m}$ to $-20\,\text{m}$.

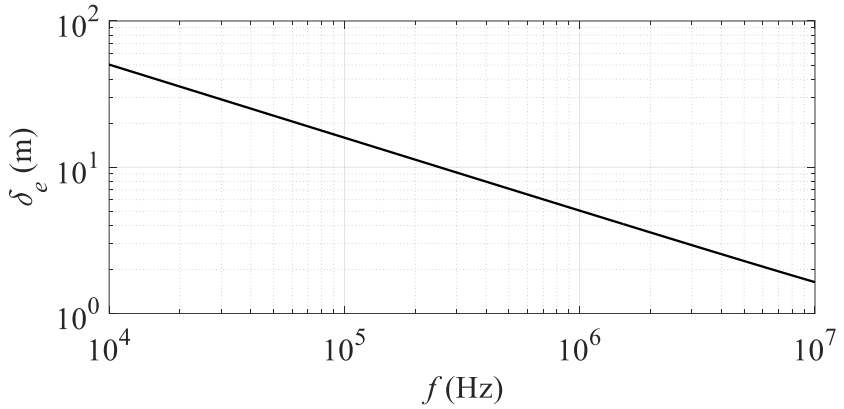

Figure 4.29: Penetration depth of earth calculated by (3.37), ρ_e = 100 Ωm and ε_r = 1

4.5.2.4 Validation of approximate earth-return potential coefficient formula

In this section, the proposed approximate earth-return potential coefficient formula (3.97) is validated in comparison with extended TL approach. As shown in Figure 4.30 and Figure 4.31, the results calculated by (3.97) agree well with extended TL approach. Therefore, (3.97) can be used as a reasonable approximation in cable transient calculations, and it avoids solving any types of Sommerfeld integrals.

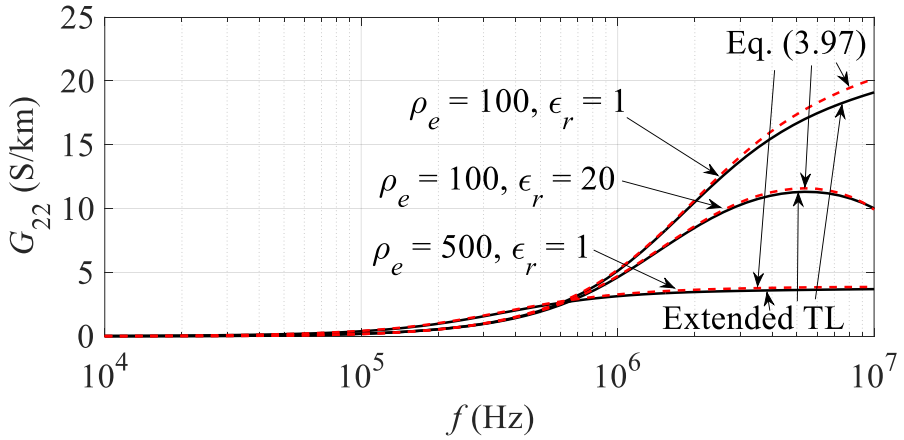

(a) Self-conductance

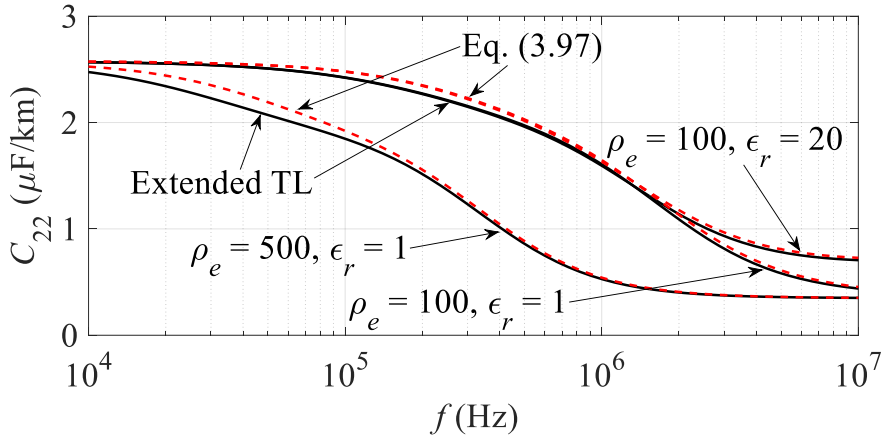

(b) Self-capacitance

Figure 4.30: Self-admittance of phase - *a* sheath by the extended TL approach and (3.97)

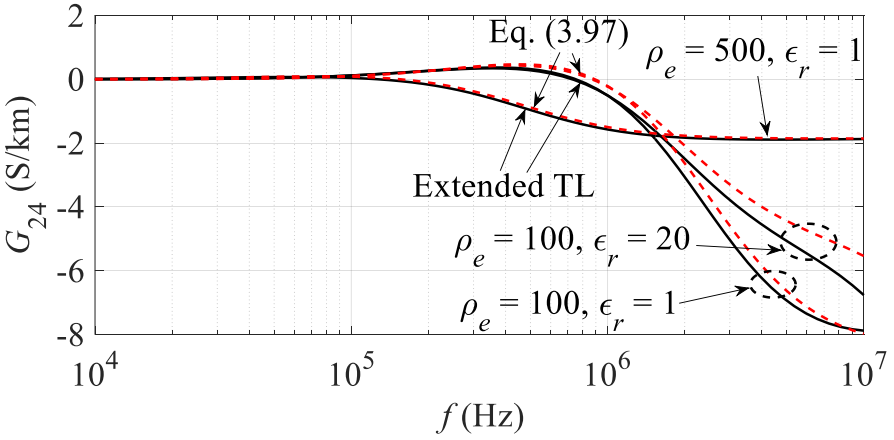

(a) Mutual conductance

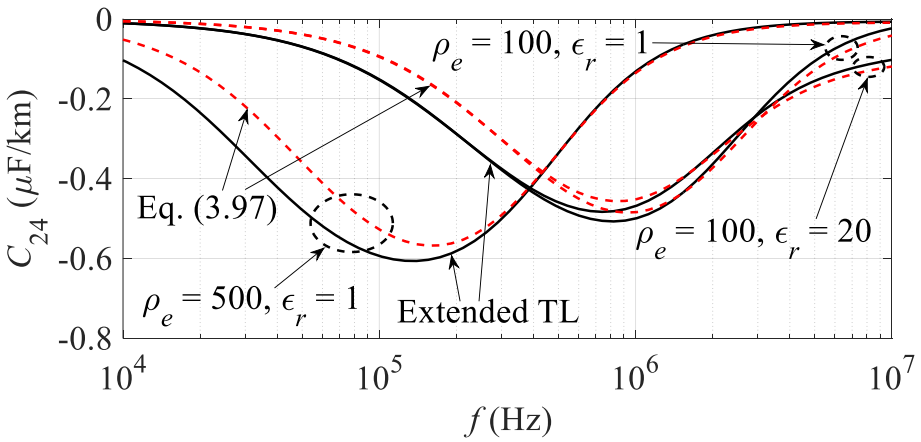

(b) Mutual capacitance

Figure 4.31: Mutual admittance between phase - *a* and phase - *b* sheaths by the extended TL approach and (3.97)

4.5.3 Propagation constants

Cable 1 illustrated in Figure 4.18 is used to calculate modal propagation characteristics. It is clear in Figure 4.32 that the attenuation constant and phase velocity of the earth-return mode and inter-sheath mode show a significant difference between the extended and classical TL approaches above 10 kHz.

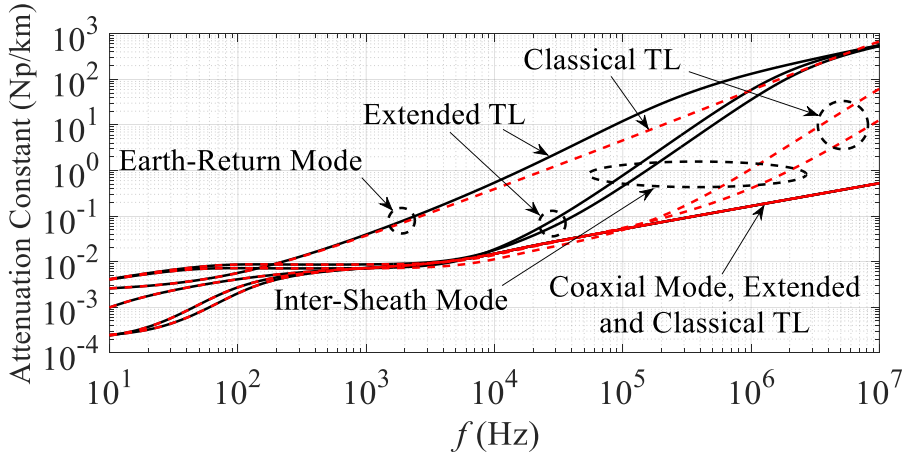

(a) Attenuation constant

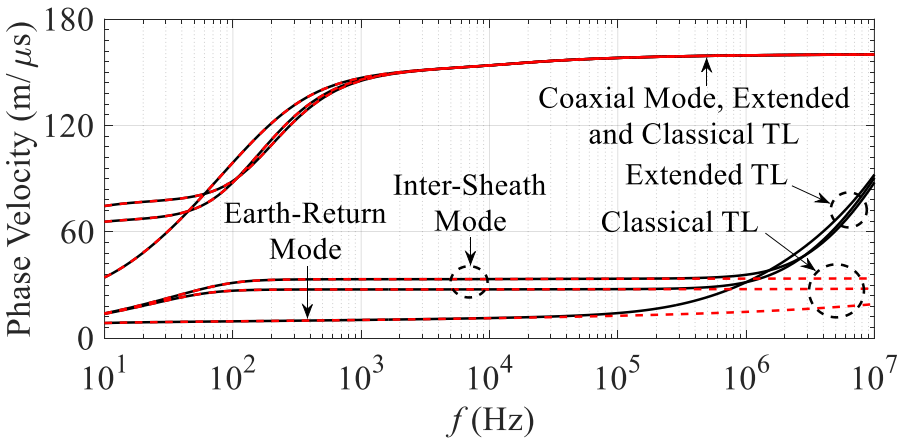

(b) Phase velocity

Figure 4.32: Modal propagation constants on Cable 1 in Figure 4.18 by the extended and classical TL approaches, $\rho_e = 100$ Ωm and $\varepsilon_r = 1$

The phase velocity of the extended TL approach increases faster as frequency increases at high frequencies, whereas the velocity evaluated by the classical TL approach is nearly constant. The higher attenuation and higher velocity at high frequencies in the extended approach are caused mostly by the earth-return admittance. The effect of earth-return impedance is minor as observed in Section 4.5.1.

Before discussing the effect of earth-return admittance, it should be noted that the capacitance C is the total capacitance of the series circuit of the cable outer insulator capacitance C_i and earth-return capacitance C_e when we neglect a conductance for simplicity, i.e.

$$C = \frac{C_i C_e}{C_i + C_e} \tag{4.10}$$

where $C_i = 2.57$ μF/km for Cable 1 shown in Figure 4.24.

As frequency approaches to zero, C_e tends to be far greater than C_i.

$$C_e \gg C_i: \ f \to 0 \tag{4.11}$$

Then, the total capacitance becomes C_i at low frequencies as observed in Figure 4.24.

When the frequency starts to increase, C_e starts to decrease. At high frequencies, C_e is far smaller than C_i.

$$C_e \ll C_i: \ f \to 10\,\text{MHz} \tag{4.12}$$

Therefore, the total capacitance decreases as frequency increases. It should be clear that the propagation velocity involved in the cable outer insulator, i.e. the earth-return mode and inter-sheath modes, becomes higher as C becomes smaller, because the phase constant becomes smaller. On the contrary, the capacitance C_i is independent of frequency, i.e. constant in the classical TL approach, and thus the velocity is kept nearly constant even at high frequencies, as explained in reference [97]. The higher attenuation in the extended one in Figure 4.32 (a) is explained similarly to the velocity considering the decreasing C and the existence of the conductance.

No significant differences are observed in Figure 4.32 between the extended and classical TL approaches at low frequencies. When the earth relative permittivity is taken to be 20, no significant differences from those with $\varepsilon_r = 1$ are observed, although the results are not shown in Figure 4.32. The coaxial mode shows no differences for all the cases, as expected.

Figure 4.33 shows the modal propagation constants calculated by Cable 2 in Figure 4.18. A significant difference is observed between extended and classical TL approaches for earth-return and inter-sheath modes above some ten kHz, similarly to that explained for Cable 1. Only minor differences are observed between Figure 4.32 and Figure 4.33, although the cable arrangement is different.

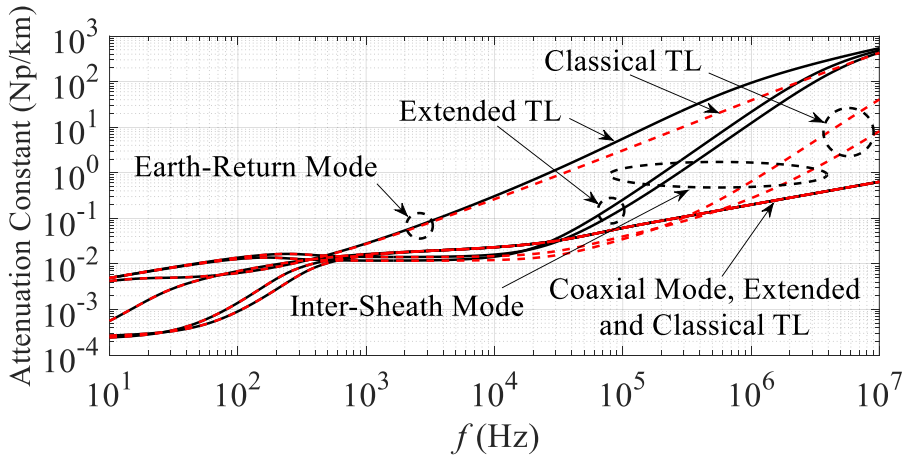

(a) Attenuation constant

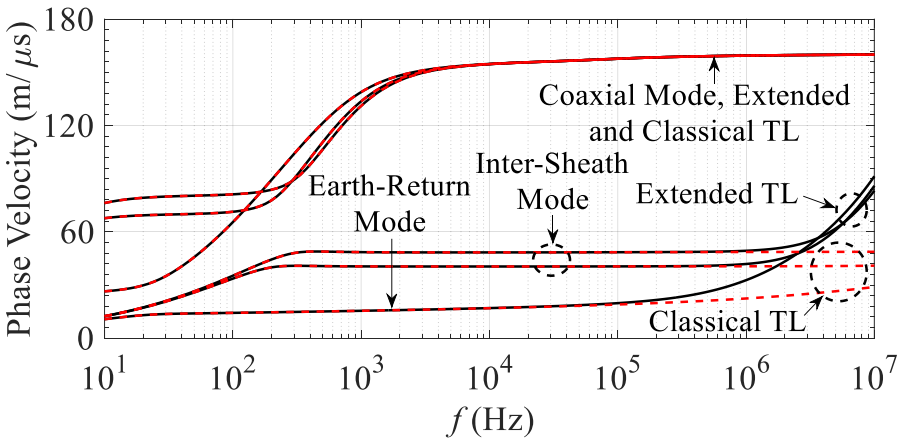

(b) Phase velocity

Figure 4.33: Modal propagation constants on Cable 2 in Figure 4.18 by the extended and classical TL approaches, $\rho_e = 100$ Ωm and $\varepsilon_r = 1$

The modal propagation constants of Cable 3 are shown in Figure 4.34. A difference of the coaxial and inter-sheath modes in comparison with those calculated by Cable 1 and 2 becomes more noticeable. This is caused by the configuration of Cable 3 being more symmetrical than Cables 1 and 2, and it makes two coaxial modes and two inter-sheath modes overlapped.

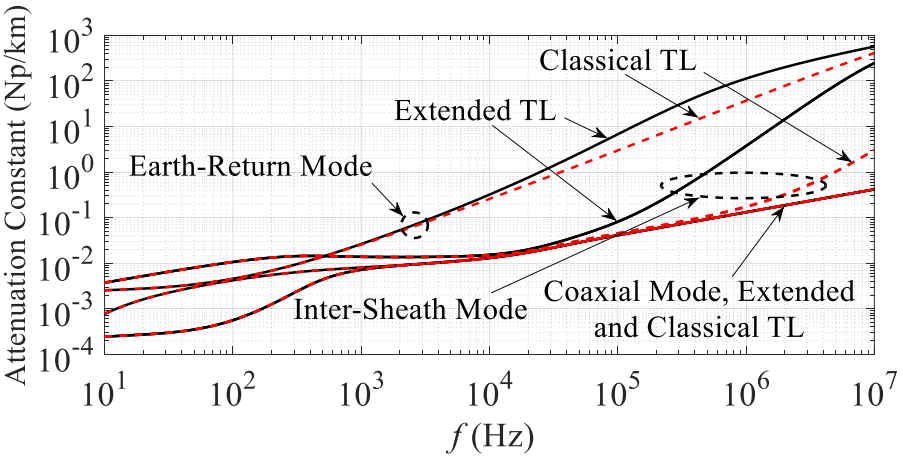

(a) Attenuation constant

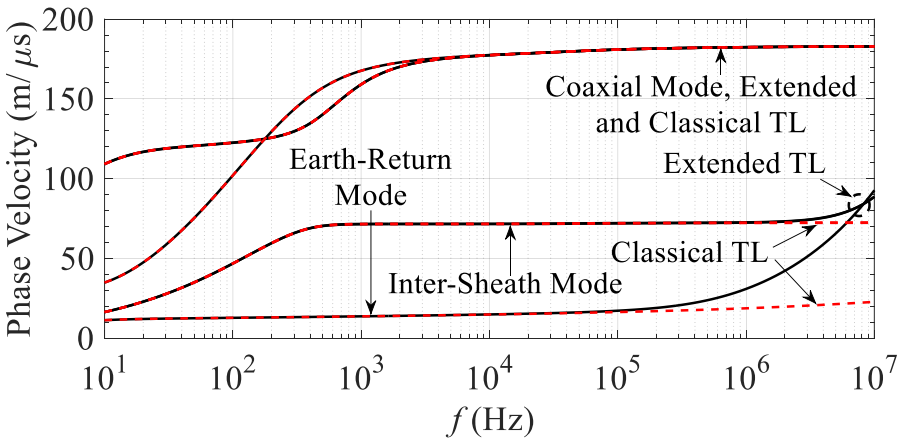

(b) Phase velocity

Figure 4.34: Modal propagation constants on Cable 3 in Figure 4.18 by the extended and classical TL approaches, $\rho_e = 100$ Ωm and $\varepsilon_r = 1$

4.6 Concluding remarks

In this chapter, the extended TL approach is explained by adopting the newly derived earth-return impedance and admittance for an overhead line, overhead cable and underground cable in Chapter 2 and Chapter 3. The classical TL approach means the existing formulas implemented into the current EMTP [1], [2].

It has been confirmed that the earth resistivity shows a minor influence on the series impedance for the overhead and underground cables. However, the earth resistivity influences significantly on the shunt admittance of the overhead and underground cables. In addition, the series impedance and shunt admittance are much less influenced by the earth permittivity.

The influence of the voltage reference on the shunt admittance is also investigated. The formula (3.74) based on the assumption the earth surface voltage being zero is significantly different from the formulas (3.78) and (3.72) based on the penetration depth of earth and infinite depth of earth. It confirms that the earth surface cannot be assumed to be the effective zero potential plane, and thus it gives an in-accurate result.

When the improved earth-return Green function of an overhead line for MoM-SO is adopted, the numerical instability observed by the original MoM-SO can be avoided. The reason of the

instability has been confirmed to be caused by the uniform current assumption in earth-return Green function.

Furthermore, because of the earth-return admittance adopted into the extended TL approach, the following characteristics of propagation constants and electromagnetic field are observed.

- Sommerfeld-Gaubau wave propagation can be observed at high frequencies for an overhead line and an overhead cable. This characteristic shows mode transition from a low frequency earth-return wave to a high frequency surface wave.
- Similar mode transition of the axial electric field component can be observed at high frequencies on an overhead conductor.
- In the surface wave propagation, the earth resistivity and permittivity have no influence on attenuation constants and axial electric field component.
- A significant difference of modal propagation constants on an underground cable is observed between the extended and classical TL approaches. The attenuation constant and phase velocity of the earth-return and inter-sheath modes increase as frequency increases. Such phenomena cannot be discussed in the classical TL approach.
- The cable configuration, such as flat, vertical or trefoil arrangement, shows minor influence on the modal propagation constants of an underground cable.
- The propagation constant of the coaxial mode on overhead and underground cables is independent from earth-return parameters.

CHAPTER 5 TRANSIENT SIMULATIONS IN TIME DOMAIN

In this Chapter, very fast transient (VFT) surges are calculated in a simple 500 kV gas-insulated bus (GIB). Based on the calculated responses using extended and classical TL approaches, the characteristics of the VFT surges and the effect of mode transition are discussed. The calculated results of the switching surges are compared with EMTP simulations in which the extended TL approach is implemented, and with measured VFT frequencies in gas-insulated substation (GIS). Next, VFTs of a full 500 kV GIS are investigated based on EMTP simulation. At first, the effect of the total length of the GIS on VFTs is investigated. Then, the effects of pipe grounding, spacers, disconnector (DS) length and circuit breaker (CB) radii are discussed. The effect of a source circuit and an operating DS are investigated. Also, theoretical formulas for the core voltage and the lowest oscillating frequency are derived in a lumped-parameter equivalent of the GIS. The oscillating frequency and a voltage waveform calculated with formulas are compared with EMTP results to confirm validity.

Also, lightning surges on an overhead distribution line are calculated by EMTP and compared with experimental results. Furthermore, transient simulations by energizing the propagation modes and a cross-bonded underground cable are also investigated by adopting extended and classical TL approaches. The differences of wave propagation and surge characteristics between extended and classical TL approaches are clarified.

5.1 Switching surges on an overhead cable

5.1.1 Step voltage response

When a source voltage defined as $E(\omega)$ in the frequency domain is applied to the sending end of an infinitely long conductor, the voltage $V_x(\omega)$ at a distance x from the sending end is given by [4]:

$$V_x(\omega) = e^{-\Gamma(\omega)x} E(\omega) = H(\omega) E(\omega) \tag{5.1}$$

where

$$\Gamma(\omega) = \sqrt{Z(\omega) Y(\omega)} \tag{5.2}$$

$Z(\omega)$ and $Y(\omega)$ are the series impedance and shunt admittance of the line, respectively.

The time response of $v_x(t)$ is calculated by numerical Fourier or Laplace transform as [71]-[73]:

$$v_x(t) = F^{-1}\left[V_x(j\omega)\right] \tag{5.3}$$

When $E(\omega)$ is given as $1/(j\omega)$, i.e. a unit step function in frequency domain, $v_x(t)$ becomes the step response of the propagation constant $\Gamma(\omega)$ in time domain. Figure 5.1 and Figure 5.2 show the calculated results of step responses on the GIB core in Figure 4.13.

A spike-like voltage is observed at the wave front of the step responses calculated by the extended TL approach, while no such voltage appears in those calculated by the classical TL approach. The spike voltage is a result of the lower attenuation observed in Figure 4.14 and Figure 4.15 calculated by the extended TL approach. In the classical TL approach, the attenuation increases monotonously, and the propagation function decreases monotonously as frequency increases as shown in Figure 4.15. Thus, the step responses show a smooth increase to reach 1 pu as time passes, where the pu base is the source voltage .

It is estimated that the spike voltage observed in Figure 5.1 and Figure 5.2 results in a sustained high frequency transient voltage because of a lower attenuation at high frequencies.

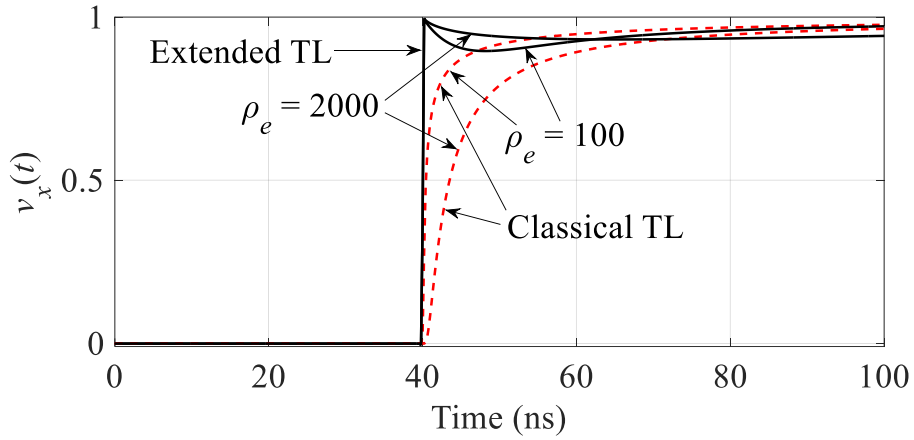

Figure 5.1: Step response on the core of GIB in Figure 4.13 by the extended and classical TL approaches at x = 12 m, ε_r = 1

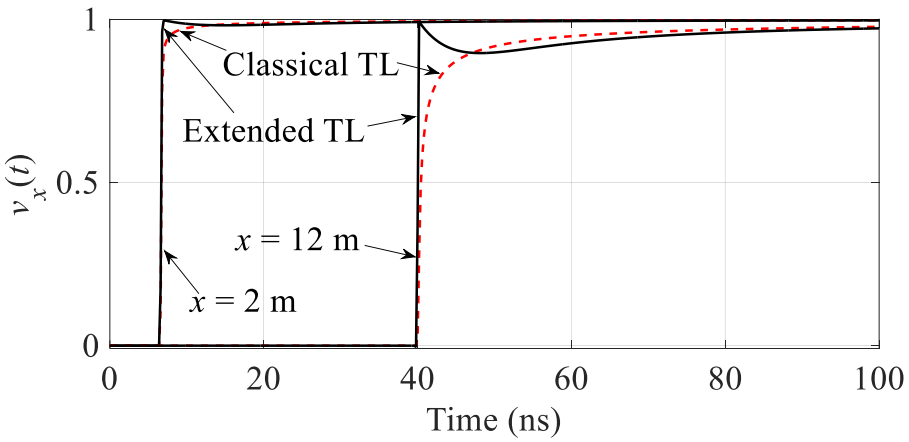

Figure 5.2: Step response on the core of GIB in Figure 4.13 by the extended and classical TL approaches at x = 2 m and 12 m, ρ_e = 100 Ωm and ε_r = 1

5.1.2 Switching surge in a simple GIB

Figure 5.3 illustrates a 12 m long GIB which is part of a 500 kV GIS [95]. The cross-section of GIB is shown in Figure 4.13.

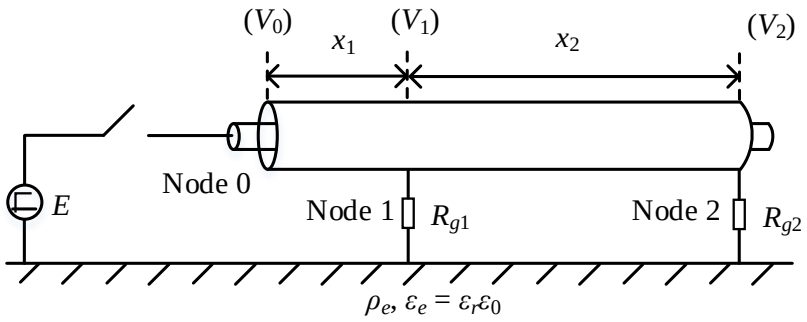

Figure 5.3: Simulation circuit for a 500 kV cascaded GIB, $R_{g1} = R_{g2}$ = 2 Ω, ρ_e = 100 Ωm, ε_r = 1, x_1 = 2 m and x_2 = 10 m

Figure 5.4 shows calculated results of the core voltage V_{2c} at the open-circuited end using extended and classical TL approaches. The calculations were made either by Laplace transform method of the frequency domain results [71]-[73], or directly in time domain using WB model in EMTP [1], [74]. Both results are almost identical, and thus only the EMTP results are presented in the following calculations.

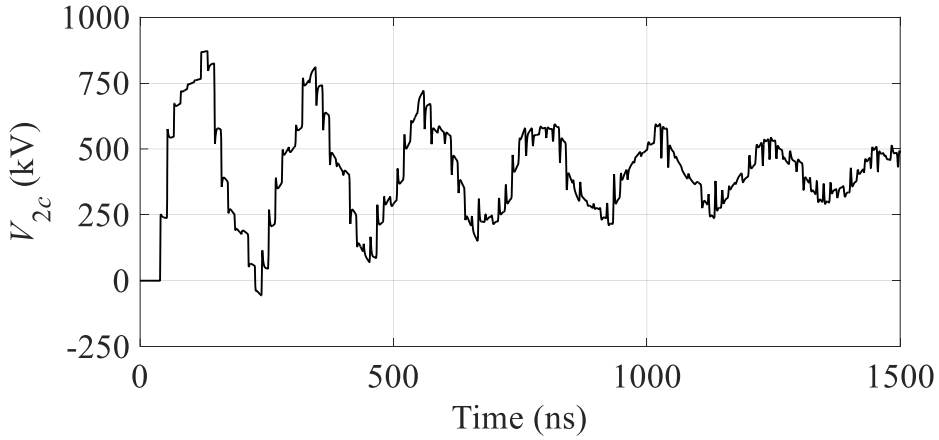

(a) Extended TL approach

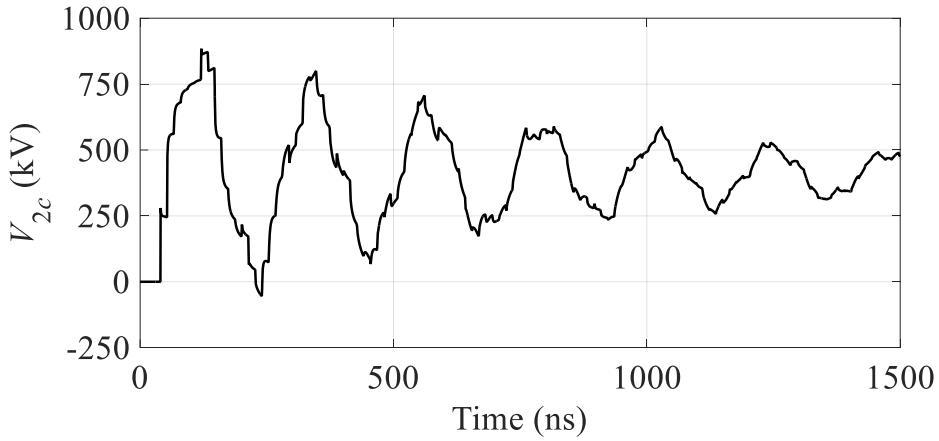

(b) Classical TL approach

Figure 5.4: Core voltage V_{2c} at the open-circuited end

The core voltage in Figure 5.4 shows a typical transient waveform on an open-circuited conductor with a dominant frequency of about 4.5 MHz. The results obtained using the extended TL approach are similar to those obtained using the classical TL approach, except for the high frequency oscillating components observed in Figure 5.4 (a), which are caused by the lower attenuation at high frequencies, and which are obviously absent in the classical TL result.

Figure 5.5 shows the transient current flowing through the grounding resistance $R_{g2} = 2\,\Omega$ of the pipe at the receiving end.

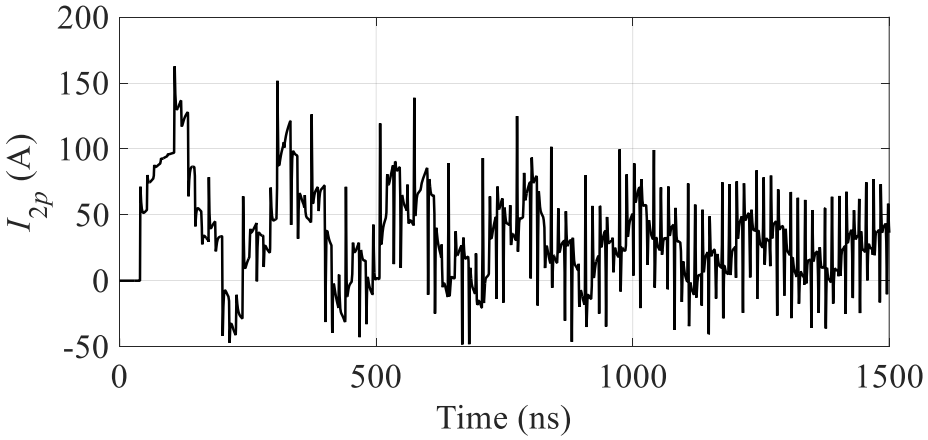

(a) Extended TL approach

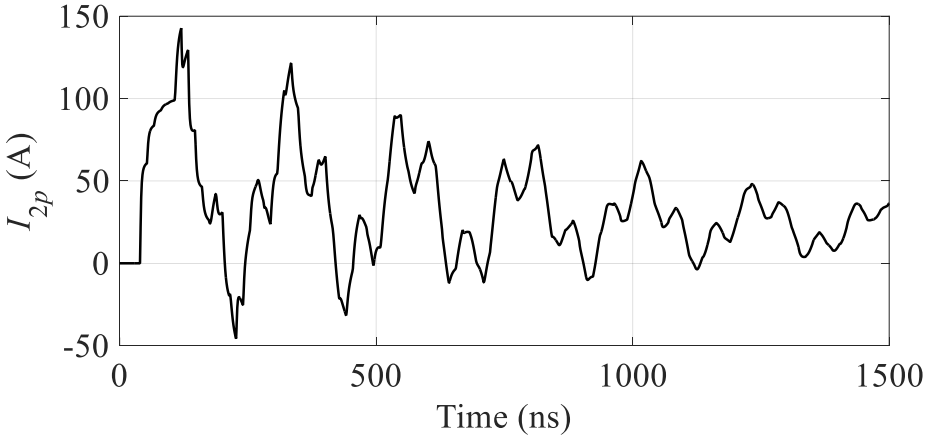

(b) Classical TL approach

Figure 5.5: Transient current I_{2p} through grounding resistance R_{g2} = 2 Ω at the pipe receiving end

In this case, more significant differences can be observed between the results obtained using the extended TL approach and those obtained using the classical TL theory. While the oscillating transient current is damped out in Figure 5.5 (b), the high frequency transient is sustained in Figure 5.5 (a). The high frequency components are caused by the lower attenuation at high frequencies. The oscillating frequencies in Figure 5.5 (b) are about 4.5 and 15 MHz with a peak-to-peak current of about 50 A after $t = 1000$ ns, while the waveform in Figure 5.5 (a) contains oscillating frequencies of about 4.5, 15 and 70 MHz with a peak current of about 150 A after $t = 1000$ ns.

The dominant transient frequency of a switching surge is approximately evaluated as a function of the conductor length x, height h (source and grounding lead wires) and the propagation velocity c of the travelling wave.

$$f = \frac{1}{T} \tag{5.4}$$

where

$$T = 2\tau \text{ to } 4\tau \tag{5.5}$$

The time delay τ is given by:

$$\tau = \frac{x}{c} \tag{5.6}$$

The above equation is valid for a short time period during a traveling wave phenomenon.

In Figure 5.3, the propagation velocities c_c and c_e for the coaxial mode (core-to-pipe) and the earth-return mode (pipe-to-earth) are nearly equal to the speed of light in the high frequency region. Therefore, the following dominant frequencies can be estimated.

$$x_a = x_1 + x_2 = 12 \text{ m}: \ f_a = \ 6 \text{ to } 12.5 \text{ MHz} \tag{5.7}$$

$$x_b = x_2 = 10 \text{ m}: \ f_b = \ 7.5 \text{ to } 15 \text{ MHz} \tag{5.8}$$

$$x_c = x_1 = 2 \text{ m}: \ f_c = \ 37 \text{ to } 75 \text{ MHz} \tag{5.9}$$

In the above equations, the calculation with x_a corresponds to the lowest frequency generated in a transient on the GIB in Figure 5.3. The calculation with x_b corresponds to the oscillating frequency generated by travelling wave reflection / refraction between nodes 1 and 2, and the case of x_c corresponds to a possible highest frequency generated by the bus length x_1 between nodes 0 to 1. In fact, a minor difference between the propagation velocities c_c and c_e is observed, although they are assumed to be the same in the above equations. If the difference is considered, much higher frequencies can be generated in a GIS [78], [81], [95].

The above frequencies correspond approximately to those observed in Figure 5.4 and Figure 5.5.

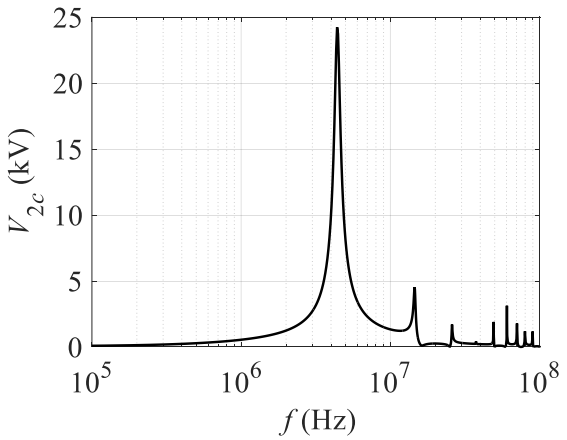

(1) Voltage in Figure 5.4

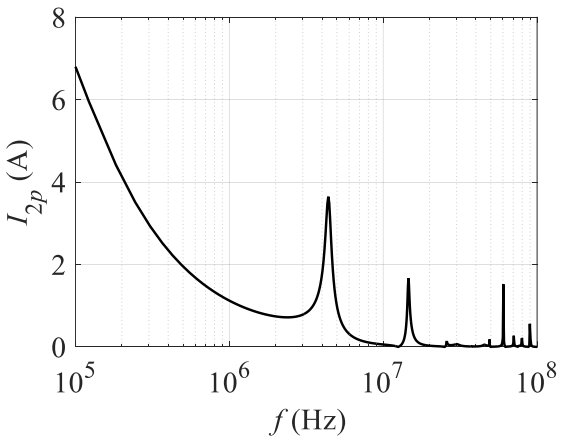

(2) Current in Figure 5.5

(a) Extended TL approach

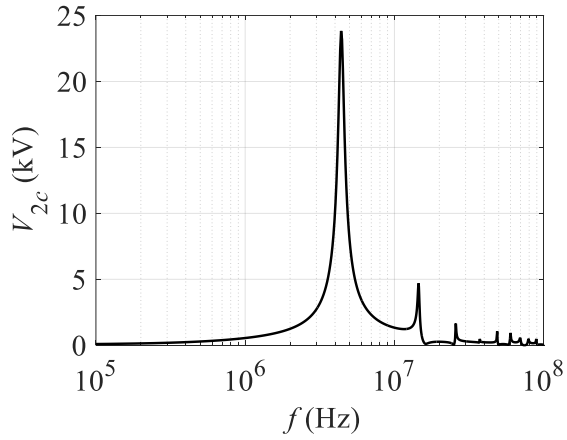

(1) Voltage in Figure 5.4

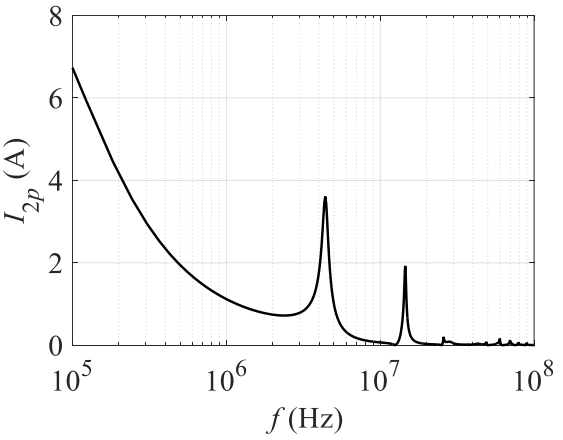

(2) Current in Figure 5.5

(b) Classical TL approach

Figure 5.6: Frequency spectra of the voltage in Figure 5.4 and current in Figure 5.5

Figure 5.6 shows the frequency spectra of the voltage and current waveforms in Figure 5.4 and Figure 5.5. It is clear from Figure 5.6 that the frequency spectra corresponding to the extended TL approach contains higher frequency components than those associated with the classical TL approach. For example, the spectrum in Figure 5.6 (a)-2 (extended TL approach) shows peaks at $f = 5$, 14 and 70 MHz, while the peaks in Figure 5.6 (b)-2 (classical TL approach) are at 5 and 14 MHz. The above observation corresponds to the less attenuation at high frequencies evaluated by the extended TL approach as explained in Section 4.4.1

5.1.3 VFTs in a 500 kV gas-insulated substation

VFTs are produced in a GIS during switching operation of a DS or a CB [75], [77]. It has been found based on many VFT measurements in laboratories and real GISs that the VFT frequencies range from some MHz to more than 100 MHz [98]-[112]. The VFT overvoltages range from 1.2 pu to 3.0 pu on the core conductor of the GISs, and 0.1 pu to 0.7 pu on the metallic enclosure (pipe). Because of very high frequency components, the VFTs in the GISs can cause EMI such as malfunctions in control circuits of the GISs [105]-[107], [109]-[112].

Modeling methods for EMTP are proposed in [95], [113]-[116]. It should be noted that most of these EMT-type simulations are performed by adopting a constant parameter (CP) line model. Although few papers investigated the electric and magnetic fields associated with VFTs by adopting the three dimensional (3D) full-Maxwell approach with FEM [108], [117] its application is limited because of large amount of computer resources. Most of those researches are focused on VFTs on the core of the GISs, because the insulation strength and high voltage testing of the core is essential for the GIS design and testing.

This section investigates VFTs based on EMTP [1] simulation results using a WB model with extended TL approach. At first, numerical instability of simulations for VFTs by adopting the classical TL approach is discussed. Then, the sensitive analysis of GIS parameters is performed and discussed. Also, a lumped-parameter equivalent circuit of GIS is proposed to derive the theoretical formulas for core voltage and the lowest oscillating frequency. The oscillating frequency shows a good agreement in comparison with EMTP results.

5.1.3.1 Model circuit and EMTP simulation

Figure 5.7 illustrates the layout of a 500 kV GIS [95]. In the figure, GIB is gas-insulated bus, DS is disconnector and CB is circuit breaker. 500 kV transmission lines are connected to BUS1 and BUS4 and lower voltage lines go out from BUS2 and BUS3 through transformers. Stray capacitances $C_1 = C_4 = 10\,\text{nF}$ are connected to BUS1 and BUS4 respectively representing 500 kV bus circuits and bushings [78], [81], [95]. Spacers are installed at both ends of the DSs. The lengths of the GIBs and DSs are 5 m, and CBs are of 7 m with additional lengths of 1 m on both sides as in Figure 5.7. The pipe of GIB1 is connected to the grounding mesh of the substation near BUS1.

The cross-section of GIB is shown in Figure 4.13. The cross-sections of all GIBs and DSs are about the same, but those of CBs are slightly larger. This section uses the same dimensions for all GIBs, DSs and CBS. Figure 5.8 illustrates a single-phase expression (core circuit configuration) of the 500 kV GIS in Figure 5.7. In fact, all the branches in Figure 5.8 is a two-phase circuit composed of the core and pipe. A branched line, for example "N2-N2b", in Figure 5.8 represents the left part of length 1m of CB1 in Figure 5.7, and "N3-N3b" represents the right part of CB1. In the following EMTP simulations, the circuit configuration is referred to Figure 5.8. A WB model of EMTP is adopted to represent GIBs, DSs and CBs as a two-conductor system composed of the core and pipe.

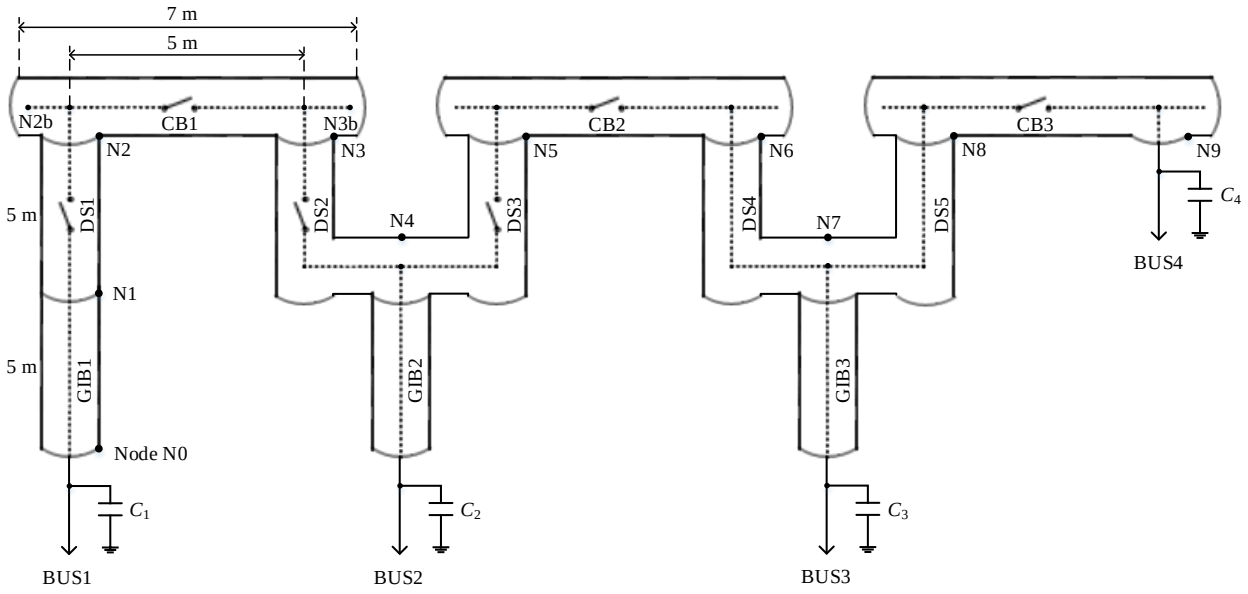

Figure 5.7: Layout of a 500 kV GIS

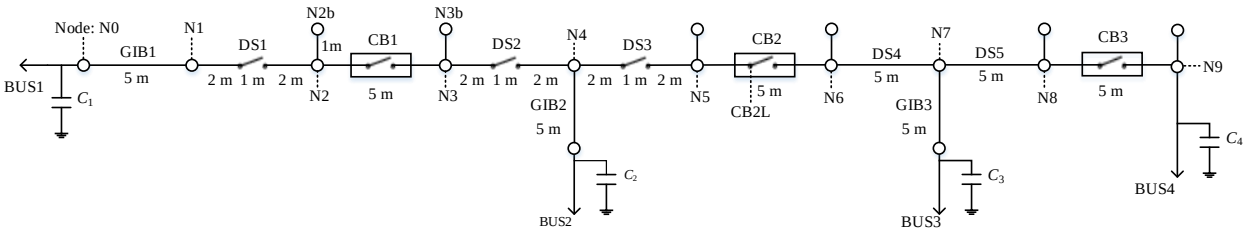

Figure 5.8: Single-phase expression (core circuit) of the 500 kV GIS in Figure 5.7

5.1.3.2 Transient simulations and discussions

5.1.3.2.1 Numerical instability of simulations for VFTs

In Figure 5.7, CB2 is kept open. DS1, CB1 and DS2 are kept closed, and charged from a 500 kV AC 60 Hz source connected to BUS1. DS3 is switched on at $t = 0$.

Figure 5.9 shows EMTP simulation results of Node1 core voltage (a) is the result by the extended TL approach and (b) by the classical TL approach. Up to 200 ns, the classical TL approach shows a similar voltage waveform to that obtained by the extended TL approach. Then it starts to diverge and shows numerical instability as is clear in Figure 5.9 (b).

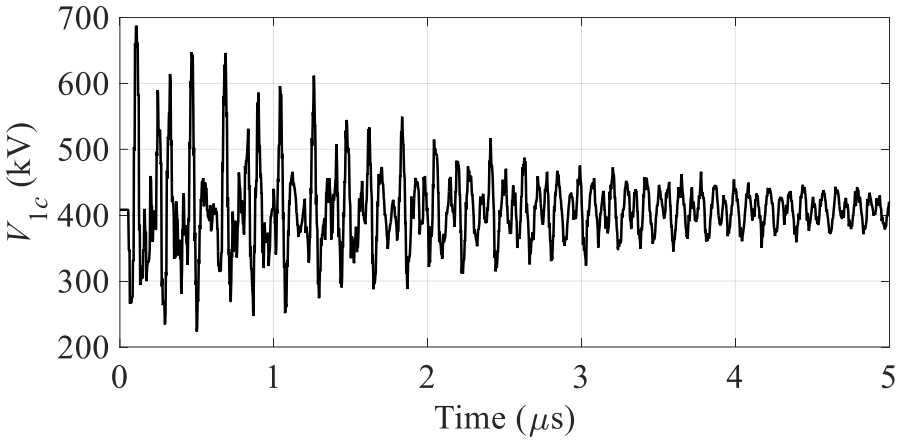

(a) Extended TL approach

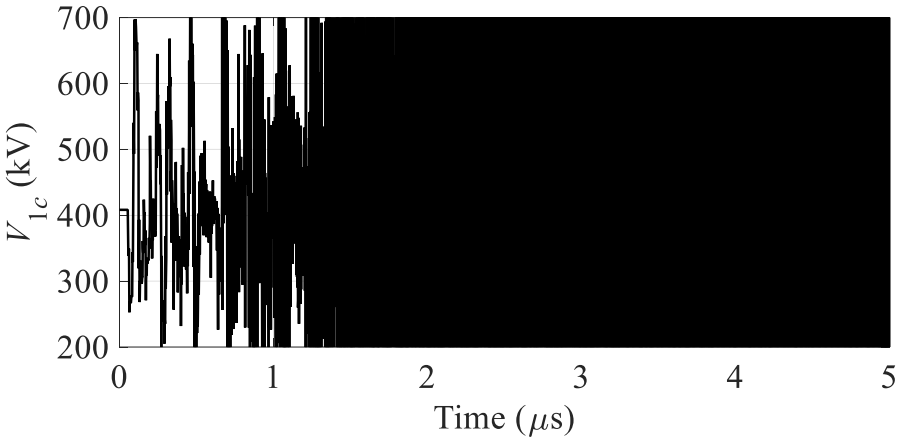

(b) Classical TL approach

Figure 5.9: Core voltage at node N1

As is well-known, the classical TL approach cannot be applied to very high frequency phenomena such as the VFT when the frequency-dependence is to be taken into account. The classical TL approach with the Carson's or Pollaczek's impedance and the space admittance cannot express the

mode transition and the surface wave propagation as explained in Section 4.3 and Section 4.4. This fact results in the numerical instability in Figure 5.9 (b). It should be pointed out that the classical TL approach gives a stable result only in the circuit configuration in Figure 5.3. When the pipe is grounded at the sending end as usual in a real substation in Figure 5.3, the classical approach results in numerical instability. Also it is to be noted that no numerical instability is observed when a perfectly conducting earth is assumed. It is noteworthy that the earth-return admittance contributes significantly to the high frequency phenomenon on an overhead line including a GIB. If the admittance is considered in an EMTP simulation of the high frequency transient, no numerical instability is observed except the one caused by a numerical instability of Pollaczek's impedance itself such as a negative inductance.

The extended TL approach shows a typical VFT waveform and converges to the steady-state voltage 408 kV. The dominant frequency of the VFT in Figure 5.9 (a) is observed to be about 10 to 15 MHz, and a higher frequency component of about 100 MHz is observed.

Figure 5.10 shows Node1 pipe voltage calculated by the extended TL approach. Since the classical TL approach results in numerical instability as explained in the above, no result are shown. Similar frequency components to those of the core voltage in Figure 5.9 (a) are also observed in the pipe voltage in Figure 5.10. Figure 5.11 shows frequency spectra of the core voltage in Figure 5.9 (a) and the pipe voltage in Figure 5.10. The frequency spectra confirm the observation of the frequencies in Figure 5.9 (a) and Figure 5.10.

In the following EMTP simulations, only extended TL approach is adopted.

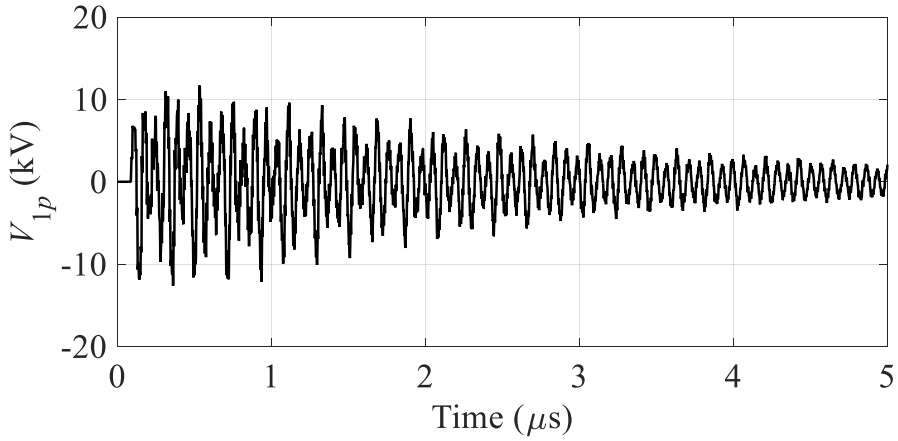

Figure 5.10: Pipe voltage at node N1 by the extended TL approach

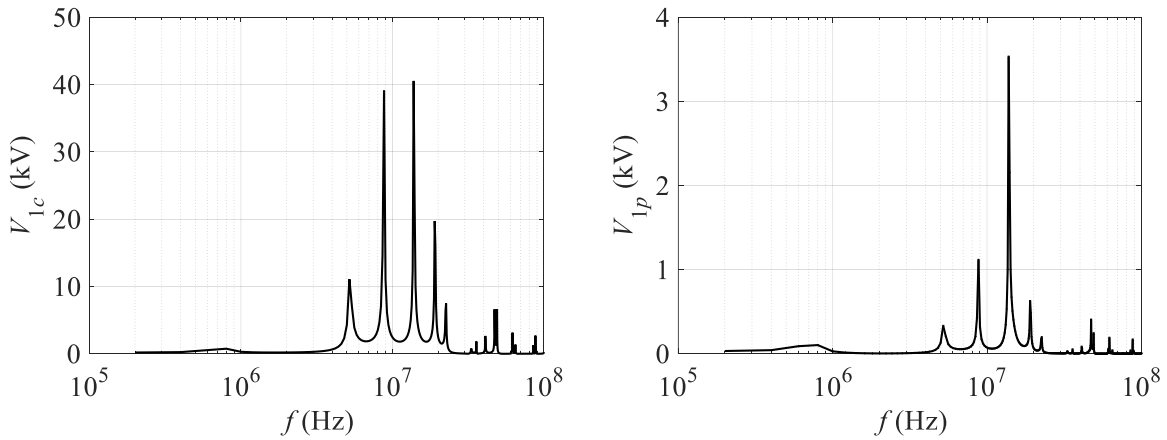

(a) Core voltage in Figure 5.9 (a) (b) Pipe voltage in Figure 5.10

Figure 5.11: Frequency spectra of core and pipe voltages at node N1

5.1.3.2.2 Effect of GIS length

The effect of total length x of a GIS composed of GIBs, GSs and CBs on VFTs is investigated for Case A1 to Case A3. To investigate the effect of x, the stray capacitances C_2 and C_3 of transformers at BUS2 and BUS3 are not considered.

Table 5.1: Effect of GIS length, $R_g = 2\ \Omega$

Case	**GIS Length x (m)**	**Condition**	**V_{cmax} (kV)**	**V_{pmax} (kV)**	**f_n (MHz)**
A1	12	CB1 open	880	-18.6	6.0
A2	27	CB1 close, DS2 close DS3 close , CB2 open	840	15.3	2.4
A3	42	CB1 close, DS2 close DS3 close , CB2 close CB3 open	811	-15.8	1.6

Table 5.1 summarizes simulation results. The left part of DS1 is in AC steady-state ($t < 0$) since BUS1 is connected to a 500 kV AC source through a source inductance $L_0 = 50\,\text{mH}$ and DS1 is switched on at $t = 0$. In all the following tables, R_g is the pipe grounding resistance. $V_{c\max}$ and $V_{p\max}$ are the maximum core and pipe voltages. f_n is the lowest natural frequency of node N1 core voltage. Figure 5.12 shows core voltages V_{1c} at node N1 for Case A1 to Case A3, and Figure

5.13 shows the frequency spectra. The maximum voltage of the core decreases as the length increases as observed in Table 5.1. The frequency becomes lower as the GIS length increases.

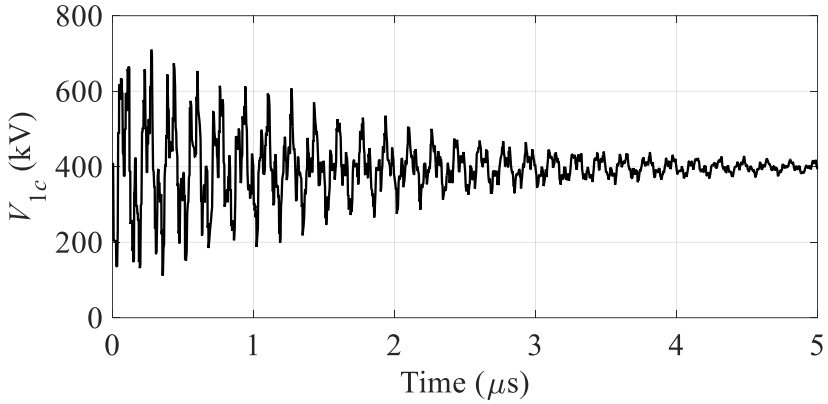

(a) Case A1

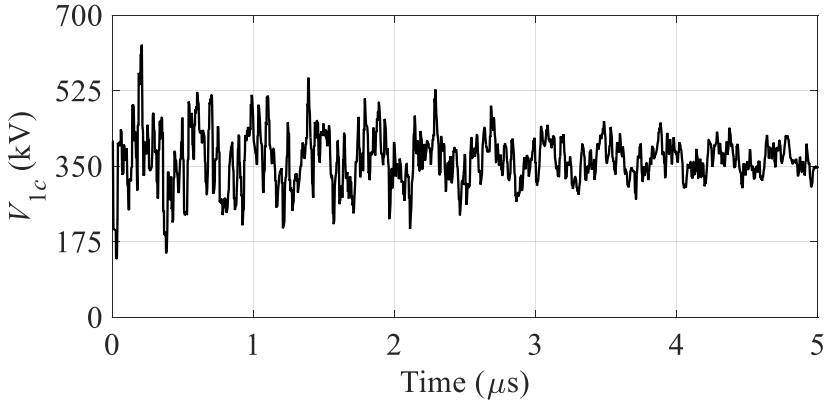

(b) Case A2

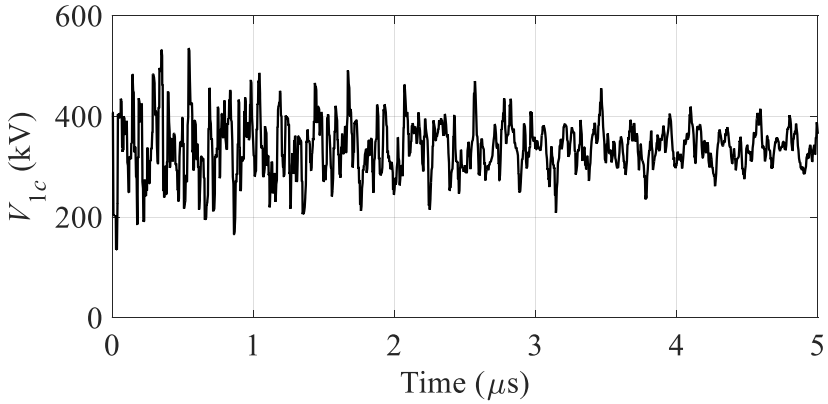

(c) Case A3

Figure 5.12: Core voltage at node N1 for Case A1 to Case A3

The lowest natural frequency is approximately evaluated by:

$$f_n = \frac{1}{4\tau} \tag{5.10}$$

where τ is the travel time in an open-circuited conductor for length given in Table 5.1.

The f_n of Case A1 to Case A3 calculated by (5.10) is summarized in Table 5.2. The lowest frequency in Figure 5.13 and Table 5.1 is close to the frequency in Table 5.2. The higher frequency components are not dependent on the GIS length, because they are produced by the terminating conditions of circuit components, such as pipe grounding and spacers. The pipe voltage shows a similar frequency spectrum to that of the core voltage, although the amplitudes are different.

Table 5.2: The lowest natural frequency f_n defined in (5.10)

Case	**τ (ns)**	**f_n (MHz)**
A1	40	6.25
A2	90	2.78
A3	140	1.78

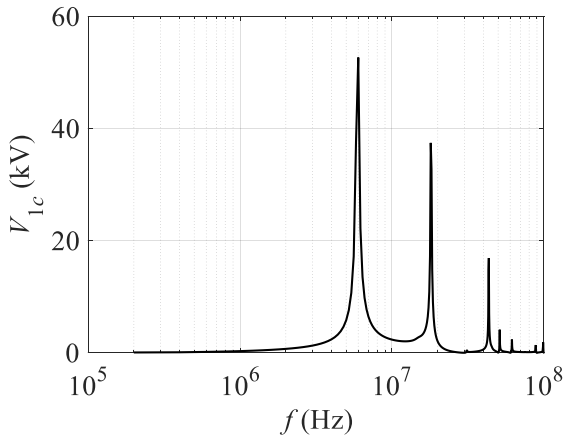

(a) Case A1

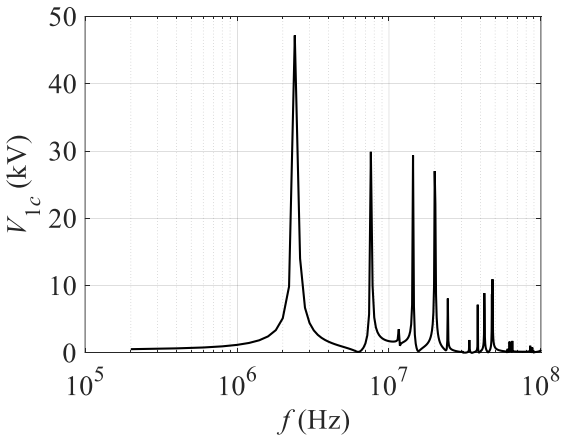

(b) Case A2

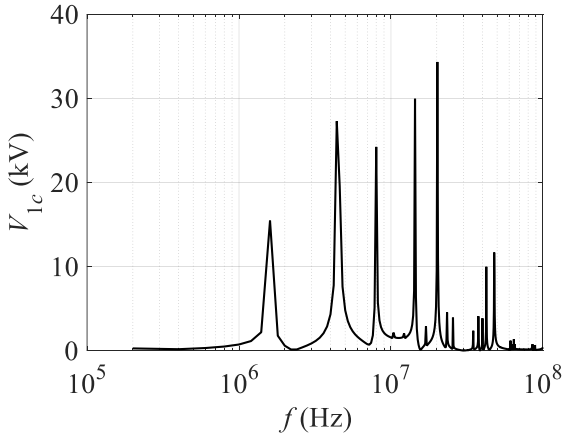

(c) Case A3

Figure 5.13: Frequency spectra of core voltages at node N1 for Case A1 to Case A3

5.1.3.2.3 Effect of transformer stray capacitances

Transformer stray capacitances have been neglected in Section 5.1.3.2.2. It is a common practice to represent an open-circuited transformer by its stray capacitance. The value of stray capacitances C_2 and C_3 of BUS2 and BUS3 transformers in Figure 5.7 are given to be 7 nF by the utility of the 500 kV GIS. The simulation results are summarized in Table 5.3. It should be noted that the steady-state and switching operations of Case A4 and Case A5 are the same as Case A2 and Case A3 except that stray capacitances C_2 and C_3 are considered.

Table 5.3: Effect of transformer stray capacitance, $R_g = 2\ \Omega$

Case	V_{cmax} **(kV)**	V_{pmax} **(kV)**	f_n **(MHz)**
A4 (A2)	573	25	1.0
A5 (A3)	438	23.5	0.8

Because of the stray capacitances, the total capacitance increases and the resultant oscillating frequency is changed. The per-unit length capacitance C' of the GIB in Figure 4.13 is:

$$C' = \frac{2\pi\varepsilon_0}{\ln\left(\frac{r_2}{r_1}\right)} = 42.7\,\text{pF/m} \tag{5.11}$$

The frequency f_n considering the stray capacitances can be roughly estimated by:

$$f_n = \frac{1}{4\sqrt{LC}} \tag{5.12}$$

where

$$L = L'x,\ L' = \frac{\mu_0}{2\pi}\ln\left(\frac{r_2}{r_1}\right),\ C = C'x + C_2 \tag{5.13}$$

From Figure 4.13, $L' = 0.2606\,\mu$H/m. For Case A4, $L = 7.0362\,\mu$H, and $C = 1.1529 + 7.0 = 8.1529$ nF. Thus, f_n in (5.12) becomes 1.044 MHz for Case A4.

In comparison with f_n of Case A2 to Case A4 in Table 5.1 and Table 5.3, the stray capacitance decreases the frequency significantly.

Figure 5.14 shows VFT waveforms of the core voltage at node N1 for Case A5 in Table 5.3. Figure 5.15 shows the frequency spectra for Case A4 and Case A5. It is clear from the comparisons of Figure 5.14 with Figure 5.12 (c), and of Figure 5.15 with Figure 5.13, that the lowest natural frequency becomes much smaller when the stray capacitance is considered. The maximum core voltage is decreased by the stray capacitance as observed in Table 5.3.

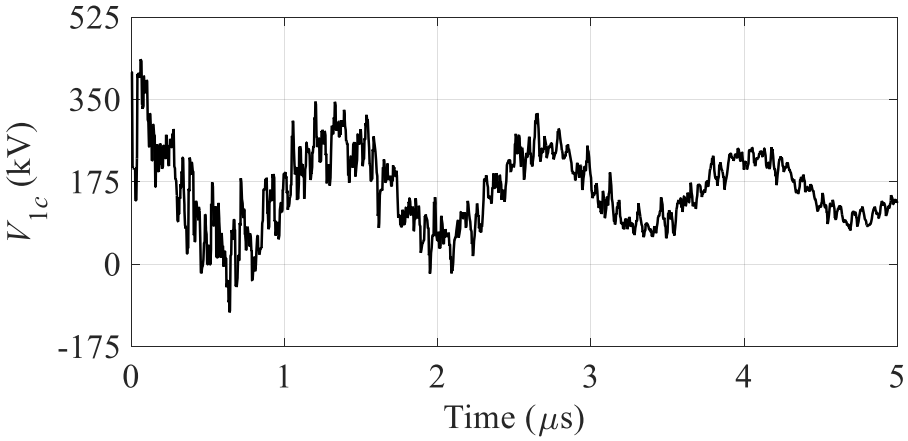

Figure 5.14: Core voltage at node N1 for Case A5

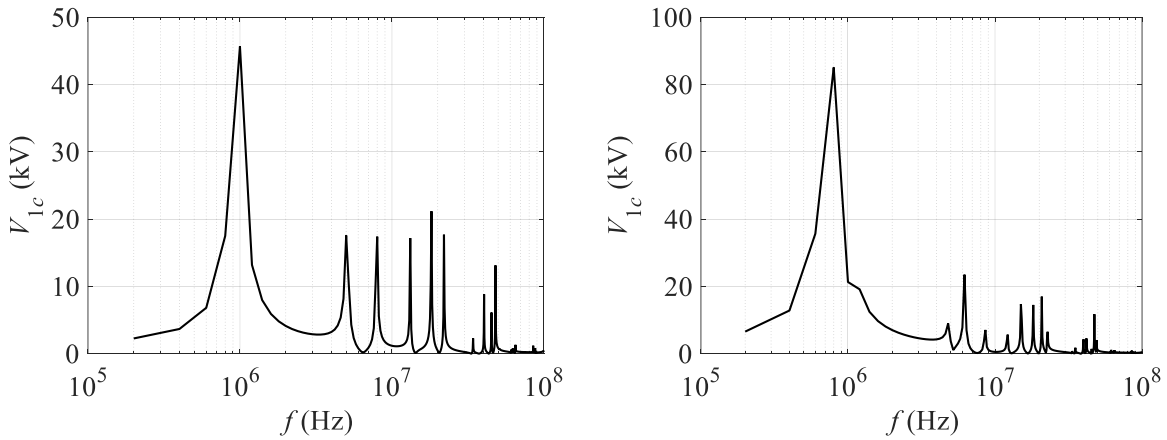

(a) Case A4 (b) Case A5

Figure 5.15: Frequency spectra of core voltages at node N1 for Case A4 and Case A5

5.1.3.2.4 Effect of pipe groundings

The simulation results are summarized in Table 5.4 and Table 5.5. The left part of DS2 or DS3 is in AC steady-state and DS2 (Case B11 to Case B14) or DS3 (Case B21 to Case B24) is switched on at $t = 0$. Figure 5.16 shows the core voltages at node N1 for Case B11 and Case B12 of Table 5.4. Figure 5.17 shows the corresponding frequency spectra. The higher R_g of Case B12 damps out the oscillating waveform in Figure 5.16 (b) much faster than that with lower R_g in Figure 5.16 (a). No significant difference in oscillating frequencies is observed between Case B11 and Case B12 in Figure 5.17, although the amplitude is much smaller in Case B12 corresponding to Figure 5.16 (b). The voltage waveform and the frequency spectrum in Case B14 are quite similar to those in Case B11. In Case B11 to Case B14, the frequency spectrum of the pipe voltage is nearly the same as that of the core voltage.

Table 5.4: Effect of R_g, DS1 close, CB1 close, DS3 close, CB2 open

Case	**R_g (Ω)**	**Number of Grounding**	**V_{cmax} (kV)**	**V_{pmax} (kV)**	**f_n (MHz)**
B11	2	4	579	22.9	1.0
B12	10	4	430	82.9	1.0
B13	0.001	4	760	0.0	1.0
B14	2	8	580	22.0	1.0

Table 5.5: Effect of R_g, DS1 close, CB1 close, DS2 close, CB2 open

Case	R_g (Ω)	Number of Grounding	V_{cmax} (kV)	V_{pmax} (kV)	f_n (MHz)
B21	2	4	690	14.9	5.0
B22	10	4	676	-52.1	5.2
B23	0.001	4	890	0	5.0
B24	2	8	685	7.8	5.0

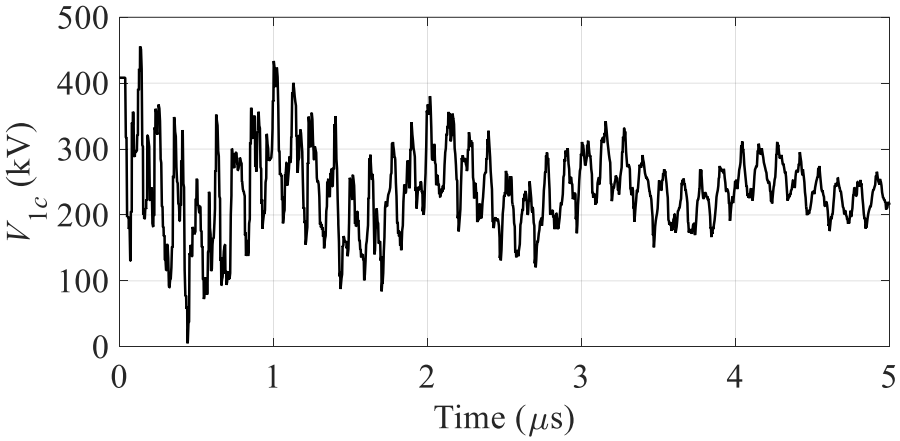

(a) Case B11

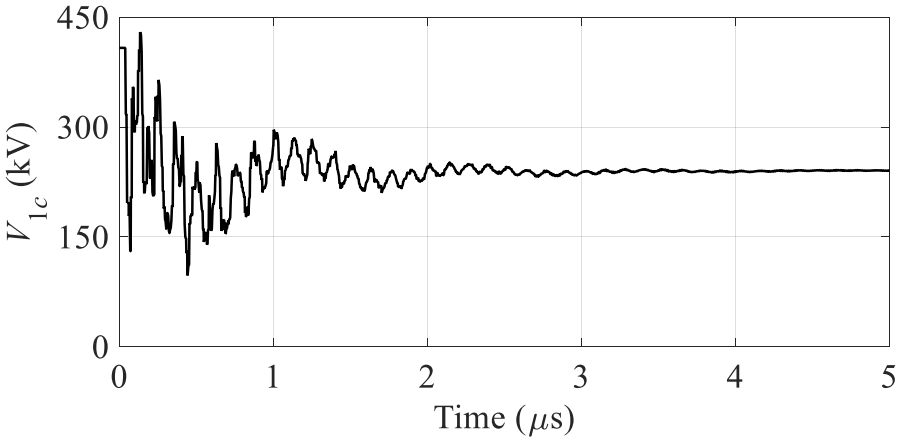

(b) Case B12

Figure 5.16: Core voltages at node N1 for Case B11 and Case B12

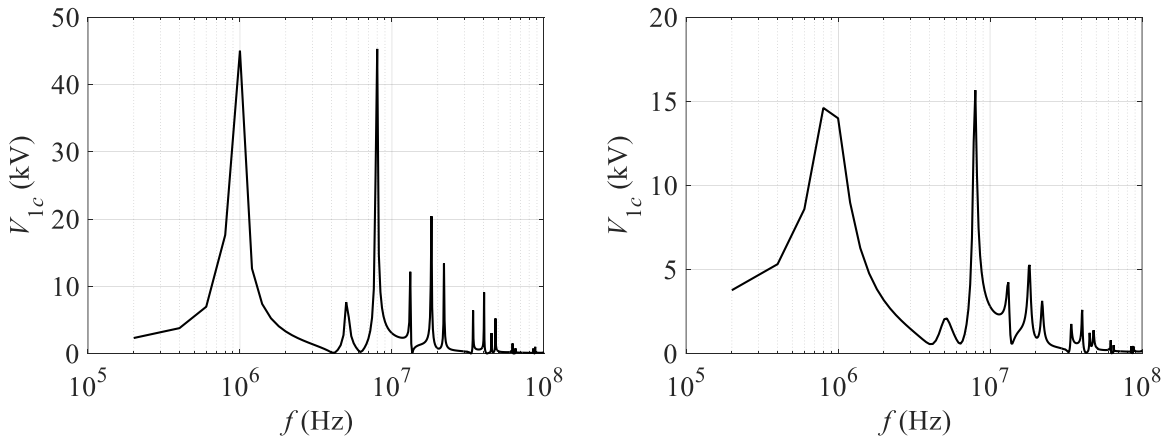

(a) Case B11 (b) Case B12

Figure 5.17: Frequency spectra of core voltages at node N1 for Case B11 and Case B12

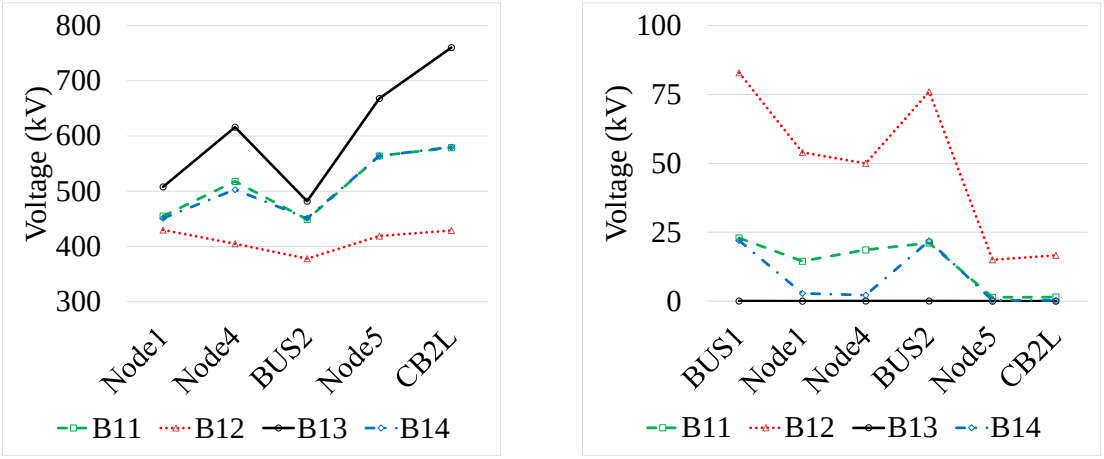

(a) Core (b) Pipe

Figure 5.18: Voltage distribution for Case B11 to Case B14

Figure 5.18 shows voltage distributions (core and pipe) along the GIS in Case B11 to Case B14. It is clear that the core voltage is the largest at the open-circuited remote end, i.e. node CB2L in Figure 5.8, and is the lowest at the node BUS2 where a stray capacitance exists, because the stray capacitance acts like a surge capacitor. The core voltage becomes higher in the lower grounding resistance case. The pipe voltage tends to decrease towards the remote end and is lower at a grounded node. The pipe voltage is the lowest when the grounding resistance is the smallest.

Although voltage distribution for Case B21 to Case B24 shows a similar trend to those in Figure 5.18, the core voltage is much higher, and the pipe voltage is smaller as in Table 5.5.

5.1.3.2.5 Effect of spacers

VFT waveforms when considering spacers, either by a CP line model or by a lumped capacitance between the core and pipe, are not much different from those neglecting the spacers [95]. The effect of spacers for Case A1 and Case A2 are summarized in Table 5.6.

Table 5.6: Effect of spacers for Case A1 and Case A2

Case	**Spacer Model**	V_{cmax} **(kV)**	V_{pmax} **(kV)**	f_n **(MHz)**
C11 (A1)	CP Line	892	23.4	5.0
C12 (A1)	Capacitance	895	-22.9	5.2
C21 (A2)	CP Line	890	-17.1	2.0
C22 (A2)	Capacitance	841	17.6	2.0

The oscillating frequency in Figure 5.19 for Case C11 and Case C12 becomes lower than that in Figure 5.13 (a) when the spacers are not considered.

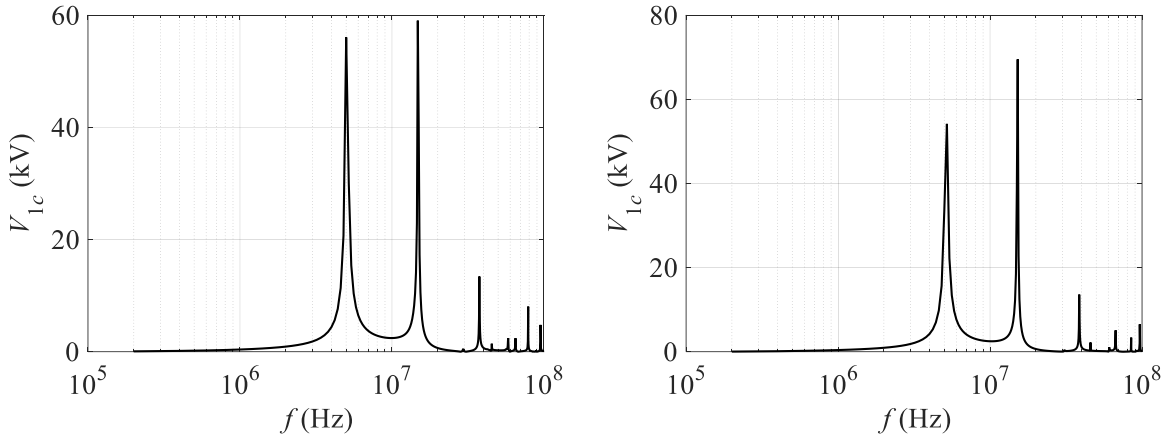

(a) Case C11 (b) Case C12

Figure 5.19: Frequency spectra of core voltages at node N1 for Case C11 and Case C12

Similar observations are made for Case C21 and Case C22, although the figure is not shown. Figure 5.19 (a) is the case of the spacer being represented by a CP line model with length 0.3 m of which the parameters are given at 10 MHz.

Surge impedance of coaxial mode:

$$Z_{oc} = 31.9\,\Omega \tag{5.14}$$

Surge impedance of earth-return mode:

$$Z_{oe} = 309.6\,\Omega \tag{5.15}$$

Propagation velocity of coaxial mode:

$$c_c = 122.4\,\mathrm{m/\mu s} \tag{5.16}$$

Propagation velocity of earth-return mode:

$$c_e = 293.1\,\mathrm{m/\mu s} \tag{5.17}$$

The lower coaxial mode impedance and velocity are caused by the spacer relative permittivity of 6. Figure 5.19 (b) is the case of the spacer being represented by a capacitance which is evaluated from the coaxial mode parameters:

$$C'_{sp} = \frac{1}{Z_{oc} c_c} = 256.1\,\mathrm{pF/m} \tag{5.18}$$

$$C_{sp} = C'_{sp}\, x_s = 76.8\,\mathrm{pF} \tag{5.19}$$

where x_s is the length of spacer.

It is clear that the oscillating frequency in Table 5.6 is decreased from that in Table 5.1 by the spacers. The effect is similar to the stray capacitance in (5.11) to (5.13). The core and pipe voltages become greater than those with neglecting spacers, because of multiple reflections and refractions of traveling waves due to the spacers.

5.1.3.2.6 Effect of other bus parameters

5.1.3.2.6.1 Length of DS3

Lengths of DSs and CBs may vary. To study such a case, the length of DS3 is decreased from 5 m in Case B11 of Table 5.4 to 3 m and then 1 m in Case D1 and Case D2 of Table 5.7. It is observed that the shorter the length, the higher the core and pipe voltages. The voltage waveforms show a

minor difference. The frequency spectra in Case D1 and Case D2 are nearly the same as that in Figure 5.17 (a) except for amplitudes.

Table 5.7: Effect of DS3 length

Case	DS3 (m)	V_{cmax} (kV)	V_{pmax} (kV)	f_n (MHz)
D1 (B11)	3	697	24.0	1.0
D2 (B11)	1	620	23.7	1.0

5.1.3.2.6.2 CB radii

The effect of a larger CB size is investigated in this section. Figure 5.20 shows the core voltage at node N1 for Case D3 in Table 5.8. The Case D3 and Case D4 correspond to Case A2 and Case A4 except the radius of CB.

Table 5.8: Effect of CB radius, CB radius: r_1 = 12.5 cm, r_2 = 64 cm and r_3 = 66 cm

Case	V_{cmax} (kV)	V_{pmax} (kV)	f_n (MHz)
D3 (A2)	846	15.4	2.4
D4 (A4)	598	24.6	1.0

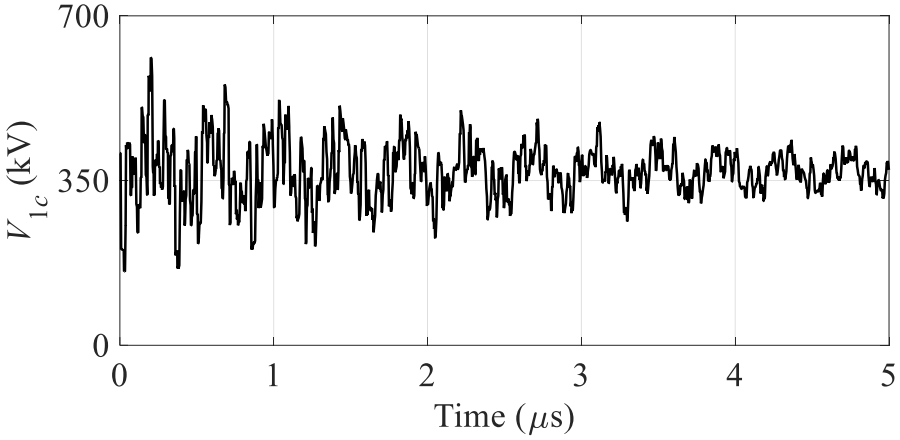

Figure 5.20: Core voltage at node N1 for Case D3

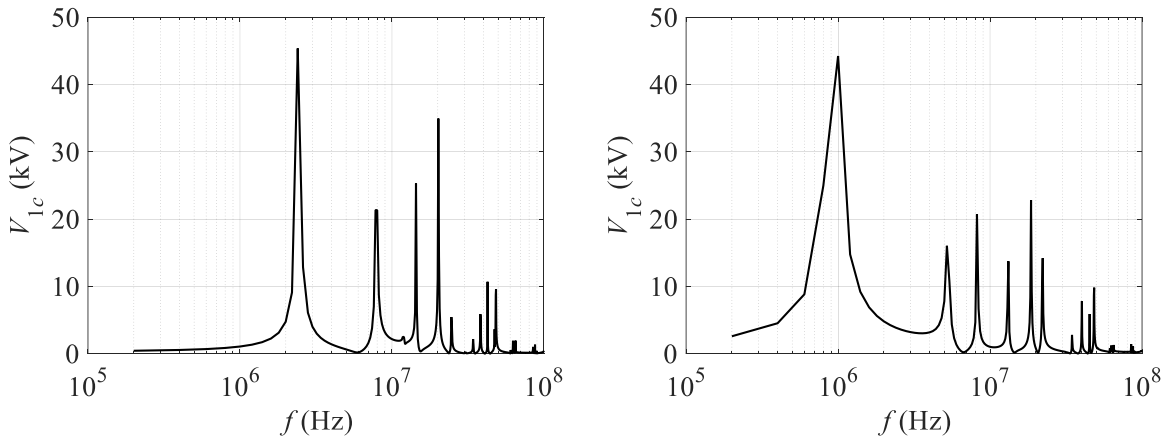

(a) Case D3 (b) Case D4

Figure 5.21: Frequency spectra of core voltages at node N1 for Case D3 and Case D4

Figure 5.21 shows the frequency spectra for Case D3 and Case D4 which are similar to that of the pipe voltage except for amplitudes. A larger ratio r_2 / r_1 results in a larger surge impedance. The change of the surge impedance from those connected to the CBs produces another traveling wave reflection and refraction. However, the overall VFT waveforms and frequency spectra in Figure 5.20 and Figure 5.21 (a) for Case D3 are not much different from those in Figure 5.12 (b) and Figure 5.13 (b) for Case A2. Similarly, Figure 5.21 (b) for Case D4 shows only a minor difference from Figure 5.15 (a) for Case A4.

5.1.3.2.7 Effect of source circuit

Stray capacitance C_1 at BUS1 in Figure 5.7 is varied from 10 nF in Case A1 to 3 and 0.5 nF in Case E1 to Case E3 of Table 5.9.

Table 5.9: Effect of source circuit parameters

Case	L_0 **(mH)**	C_1 **(nF)**	V_{cmax} **(kV)**	V_{pmax} **(kV)**	f_n **(MHz)**
E1 (A1)	50	3	835	18.0	6.2
E2 (A1)	50	0.5	818	18.7	7.6
E3 (A1)	0	0.5	885	-19.1	5.8

If no transformer exists at BUS1 and BUS4, but there are only bushings, C_1 and C_4 should be much smaller than 10 nF. For example, the stray capacitance of a 500 kV bushing is known to be about 0.5 nF. Considering this fact, the effects of C_1 and C_4 on VFTs is investigated in the Case E1 and Case E2 in this section. In a large substation, a number of incoming lines are connected to the main bus, and the source impedance of the bus becomes very small. Assuming BUS1 is an infinite bus involving only a bushing stray capacitance, EMTP simulations are performed in Case E3 with $L_0 = 0$ in comparison with that in Case E2 with $L_0 = 50\,\text{mH}$.

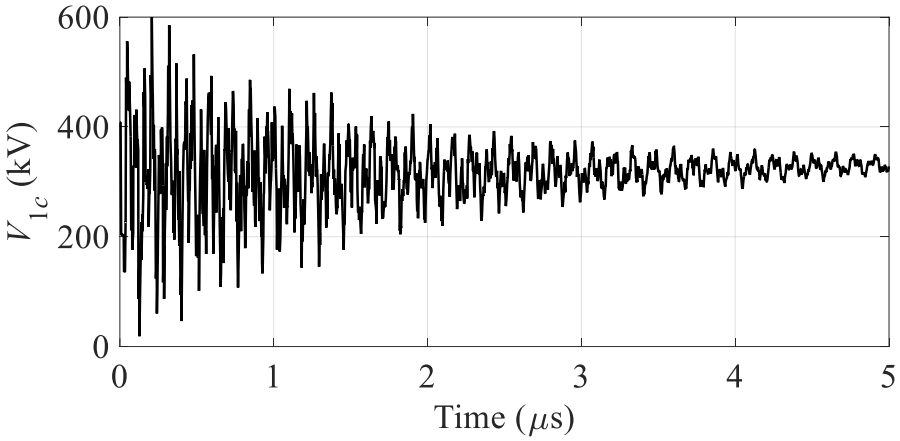

(a) Case E2

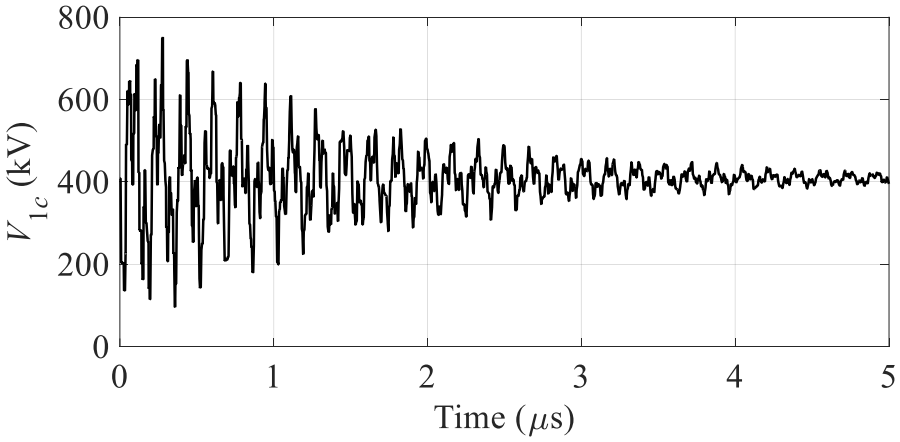

(b) Case E3

Figure 5.22: Core voltages at node N1 for Case E2 and Case E3

Figure 5.22 shows VFT waveforms at node N1 for Case E2 and Case E3. The frequency spectra are shown in Figure 5.23. It is observed that the core voltage decreases in Figure 5.22 (a) and the

lowest oscillating frequency becomes higher in Figure 5.23 (a) as capacitance C_1 becomes smaller in comparison with those in Case A1 ($C_1 = 10\,\text{nF}$) and Case E1 ($C_1 = 3\,\text{nF}$). No significant difference is observed for the pipe voltage.

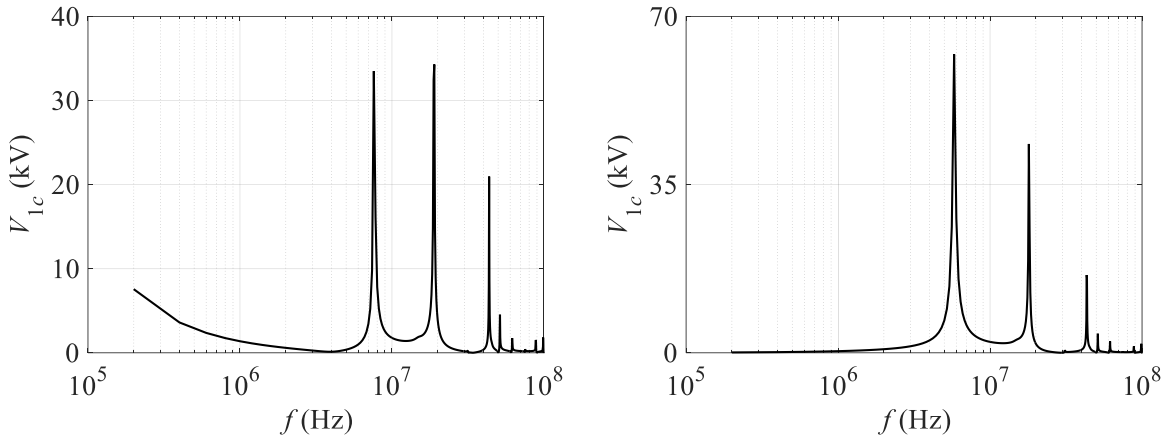

(a) Case E2 (b) Case E3

Figure 5.23: Frequency spectra of core voltages at node N1 for Case E2 and Case E3

In the Case E3, infinite source, the core and pipe voltage increase as observed in Figure 5.22 (b). The lowest frequency decreases slightly compared with that in Case E2 ($L_0 = 50\,\text{mH}$) as in Figure 5.23 (b) and Table 5.9. It should be noted that C_1 does not affect the transient response when an infinite source is used, because the impedance of the infinite source is zero.

5.1.3.2.8 Transient conditions in full circuit of Figure 5.7

It is well-known that the most severe VFT overvoltage appears when part of a GIS is charged by source voltage $+E$ and the remaining part is charged by $-E$. This is similar to the trapped charge case on transmission lines when a CB is closed.

In this section, the effect of an operating DS and source (charged) conditions in the full circuit of Figure 5.7 on VFTs are investigated. As shown in Table 5.10, the operating DS in Case F1 to Case F3 is DS1, and the left side of DS1 is charged by positive $E = 408.24\,\text{kV}$ in Case F1. In Case F2, the right side of DS1 is charged by $-E$. In Case F3, the DS1 left is charged by $+E$ and the right is charged by $-E$. In Case G1 to Case G3, an operating DS is DS3, and the charge (source) conditions in Case G1 to Case G3 are the same as those in Case F1 to Case F3.

Table 5.10: Operating DS and source conditions, all CBs close, DS2 close

Case	Operating DS	Left of DS	Right of DS	V_{cmax} (kV)	V_{pmax} (kV)	f_n (MHz)
F1	DS1	+E	0	436	23.5	0.6
F2		0	-E	-570	23.5	0.6
F3		+E	-E	-730	47.0	0.6
G1	DS3	+E	0	512	-23.9	0.6
G2		0	-E	-557	-23.8	0.6
G3		+E	-E	-705	-47.6	0.6

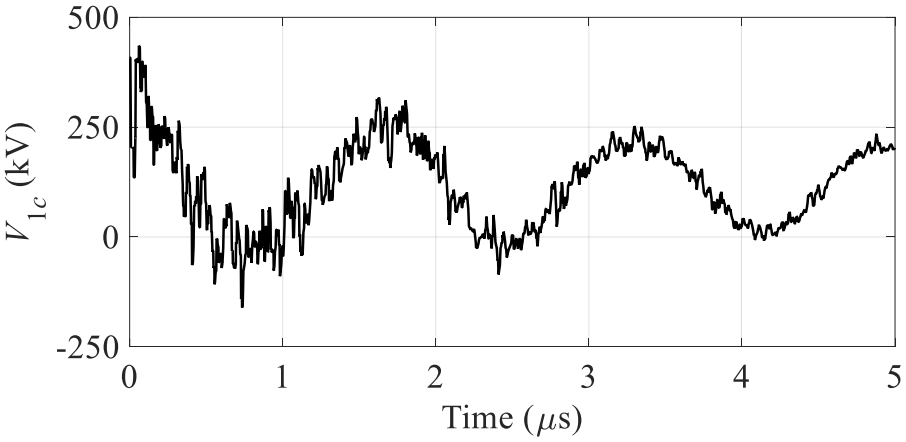

(a) Case F1

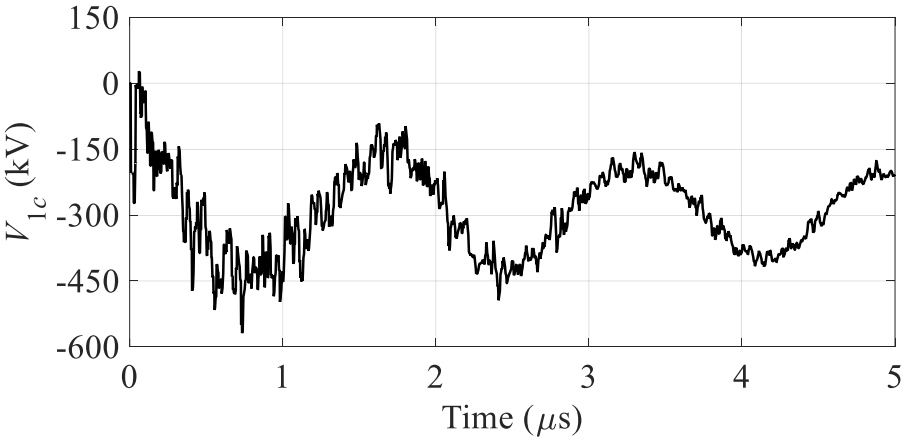

(b) Case F2

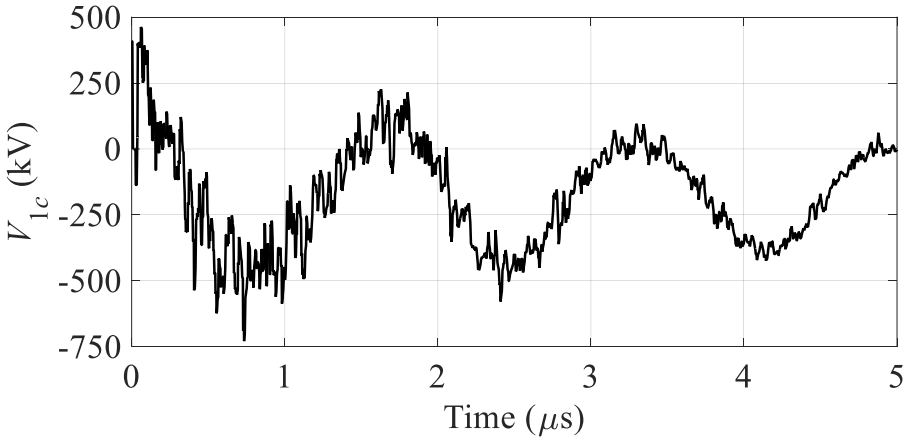

(c) Case F3

Figure 5.24: Core voltages at node N1 for Case F1 to Case F3

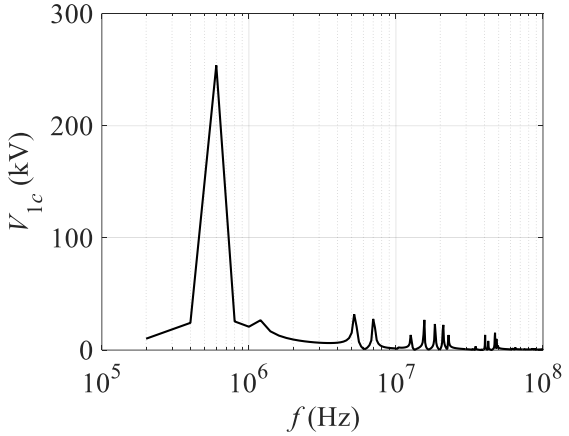

Figure 5.25: Frequency spectrum of core voltage at node N1 for Case F3

Figure 5.24 shows core voltages at node N1 for Case F1 to Case F3, and Figure 5.25 shows the frequency spectrum of the voltage for Case F3. It should be noted that the superposition law is satisfied between Cases F1 to F3 for both time domain responses in Figure 5.24 and frequency responses. Therefore, only the frequency spectrum in Case F3 is given in Figure 5.25. If the amplitudes of each spectrum in Case F1 and Case F2 are superposed, the correct amplitude in Case F3 is obtained. As is clear, Case F3 shows higher overvoltage than Case F1 and Case F2 in the overvoltage distribution along the GIS in Figure 5.26. It is observed that the pipe overvoltage distribution in Case F2 is nearly the same as that in Case F1, and the sum of the pipe overvoltage in Case F1 and Case F2 becomes nearly the same as the pipe overvoltage in Case F3. When

$C_1 = C_4 = 0.5$ nF, the core voltage becomes much larger and the pipe voltage becomes smaller than those in the case of $C_1 = C_4 = 10$ nF.

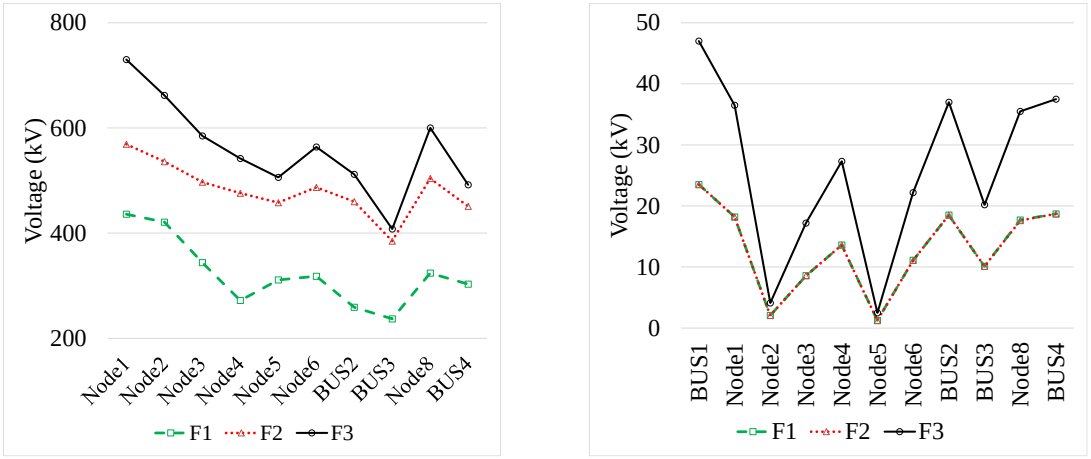

(1) Core (2) Pipe

(a) C_1 = C_4 = 10 nF

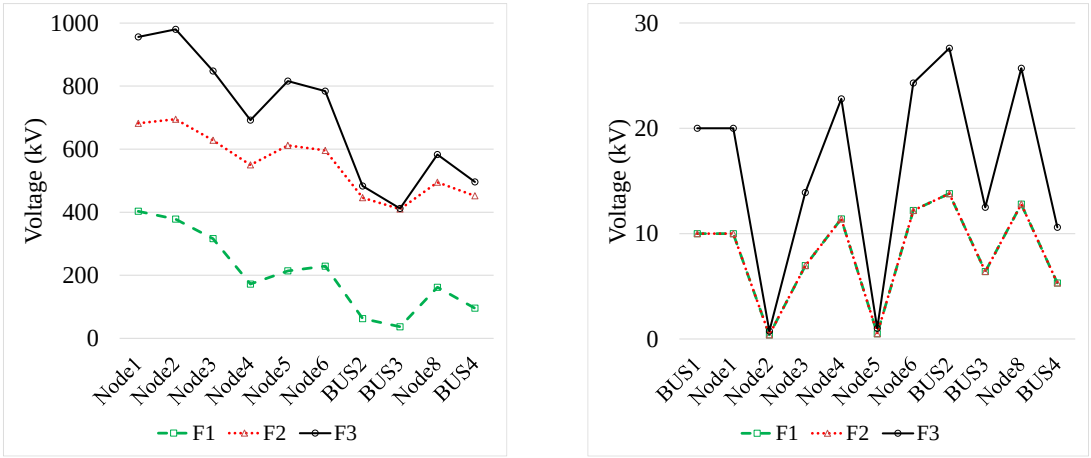

(1) Core (2) Pipe

(b) C_1 = C_4 = 0.5 nF

Figure 5.26: Maximum voltage distribution for Case F1 to Case F3

Figure 5.27 shows the voltage distribution for Case G1 to Case G3. No significant differences are observed between Case F and Case G for $C_1 = C_4 = 10$ nF. However, the core voltage in Case G is much smaller and the pipe voltage is much higher than those in Case F for $C_1 = C_4 = 0.5$ nF in Figure 5.26 (b). In other words, an operating DS influences significantly the core and pipe voltages

when C_1 is small. The voltage waveforms and frequency spectrums in Case G are similar to those in Case F.

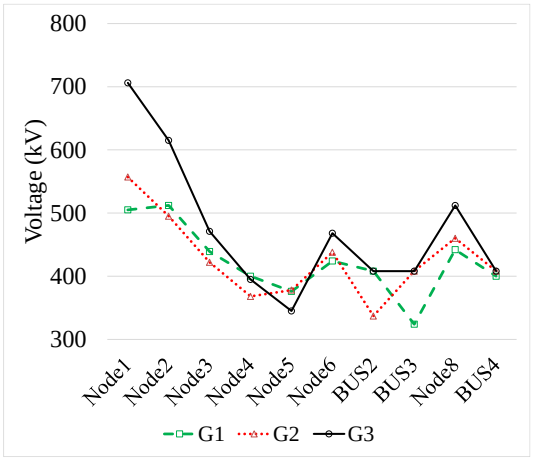

(1) Core

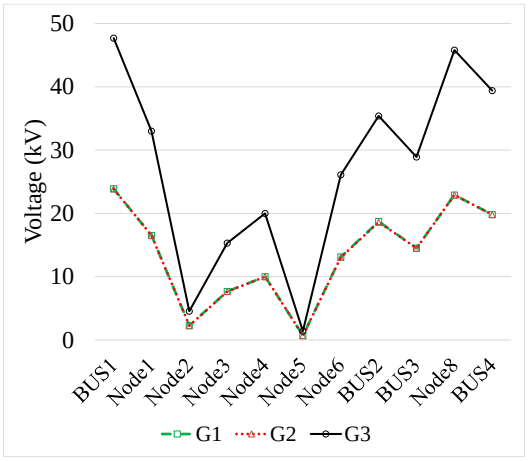

(2) Pipe

(a) $C_1 = C_4 = 10$ nF

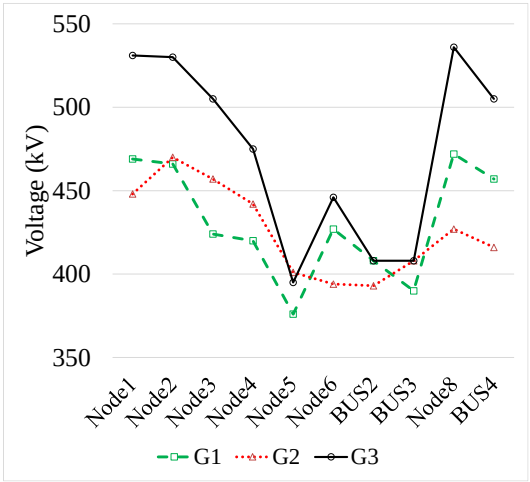

(1) Core

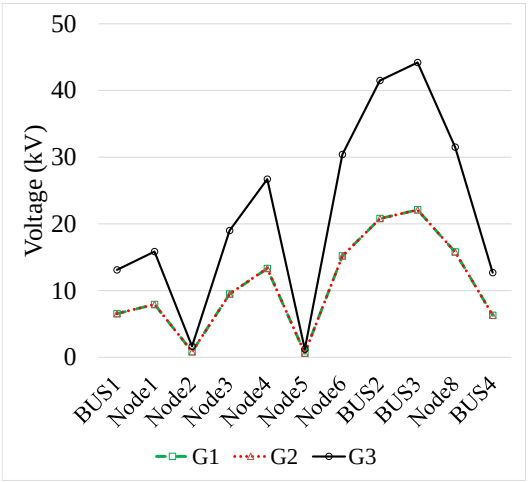

(2) Pipe

(b) $C_1 = C_4 = 0.5$ nF

Figure 5.27: Maximum voltage distribution for Case G1 to Case G3

5.1.3.2.9 Field test results at VFT frequencies

There are a number of measured results of VFT overvoltages and frequencies in GISs, switchgears and buses [99]-[112]. It should be noted that the VFT frequencies depend basically on the length of tested equipment. When only a switchgear is tested, the observed VFT frequencies are in general

very high for the short length of the switchgear. On the contrary, when a long bus, often longer than 30 m, is tested in a factory, the frequencies range from some 100 kHz to some MHz. Also, it should be reminded that most of measured VFTs in 1970s and 1980s were recorded by analog oscilloscopes and thus it was almost impossible to observe VFT frequencies higher than 10 MHz. Considering this fact, the VFT frequencies measured in real GISs [78], [79], [81], [110], [111] similar to the GIS in Fig.11, are summarized as follows:

1. High-voltage main circuits: 5 MHz to 140 MHz.
2. Metal enclosures (pipe): 2 MHz to 80 MHz.
3. Low-voltage control circuit: 2 MHz to 80 MHz.

The VFT frequencies observed in Figure 5.9 to Figure 5.11 are in the range of the above measured results.

5.1.3.3 Derivation of analytical formulas

Although the effects of various circuit parameters / conditions on VFTs are investigated by EMTP simulation, it is not easy to generalize the investigations. Analytical formulas of estimating the lowest oscillating frequency are given in (5.10) and (5.12), which approximately explains the EMTP results. Here, an analytical formula for a core voltage is derived by applying a lumped-parameter equivalent of a GIB.

5.1.3.3.1 Lumped-parameter equivalent circuit

Figure 5.28 illustrates a lumped-parameter equivalent of a GIS.

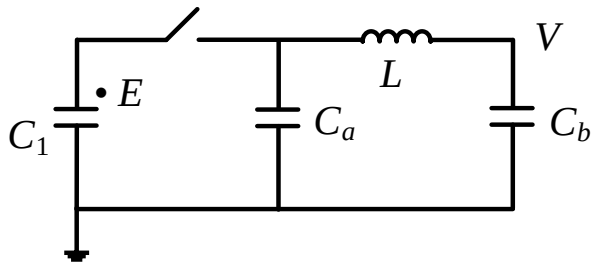

Figure 5.28: Lumped-parameter equivalent circuit of a GIS

C_1 represents the capacitance of the BUS1 circuit in Figure 5.7. C_a represents the capacitance of GIBs, DSs and CBs defined in (5.11) and stray capacitance C_2 of BUS2 transformer. Similarly,

C_b represents the GIBs and stray capacitances. L in Figure 5.28 represents the inductance of the GIBs which is estimated by (5.13).

5.1.3.3.2 Analytical formulas and calculation examples

Analytical formula of remote end voltage V in Figure 5.28 are derived as:

$$V = \frac{C_1}{C_1 + C_b + C_a}\left[1 - \cos(\omega t)\right]E \tag{5.20}$$

where DS1 operation: $C_a = C_{g1}$, $C_b = C_{g2} + C_{stray}$, Case A1 to Case A3: no C_{stray}, Case A4: $C_{stray} = C_2$ and Case A5: $C_{stray} = C_2 + C_3$.

The lowest natural frequency f_n at the remote end becomes:

$$f_n = \frac{\omega_n}{2\pi} \tag{5.21}$$

where

$$\omega_n^2 = \frac{C_1 + C_a + C_b}{LC_b\left(C_1 + C_a\right)} \tag{5.22}$$

When an infinite source E is applied, source-side capacitance C_1 causes no effect on a transient response as already explained. Then, the analytical formula becomes:

$$V = \left[1 - \cos(\omega t)\right]E,\ \omega_n = \frac{1}{\sqrt{LC_b}} \tag{5.23}$$

When the damping of a voltage waveform is to be considered, multiply $e^{-\alpha t}$ to $\cos(\omega t)$ in (5.20) and (5.23) with:

$$\alpha = \frac{R}{2L} \tag{5.24}$$

where

$$R = R_g + R'x \tag{5.25}$$

R is coaxial mode resistance, L in (5.13) and R' can be approximated by reference [118].

Table 5.11 shows calculation examples by (5.21) in comparison with EMTP results. The analytical formula in Table 5.11 agrees reasonably well with EMTP results.

Table 5.11: Frequency f_n evaluated by (5.21), L_0 = 50 mH

Case	**A1**		**A2**		**A3**		**A4**		**A5**	
C_1(nF)	10	0.5	10	0.5	10	0.5	10	0.5	10	0.5
(5.21)	6.2	6.9	2.1	3.0	1.3	2.1	0.9	2.2	0.6	1.7
EMTP	6.0	7.6	2.4	3.8	1.6	2.6	1.0	2.2	0.8	2.2

5.2 Lightning surges on a three phase overhead line

Figure 5.29 illustrates a 6.6 kV three phase overhead distribution line [119].

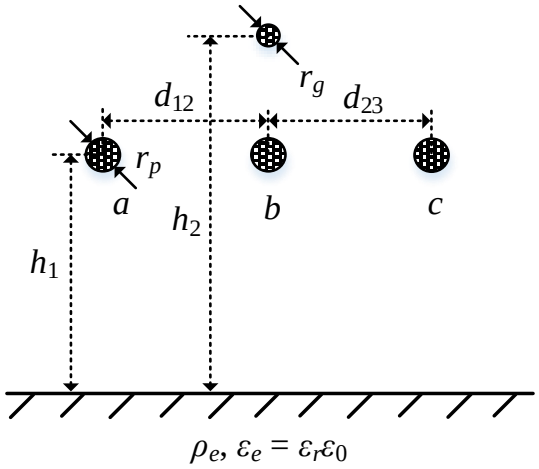

Figure 5.29: A 6.6 kV three phase overhead distribution line, h_1 = 10 m, h_2 = 11 m, $d_{12} = d_{23}$ =1 m, r_p = 0.437 cm, r_g = 0.26 cm, $\rho_p = \rho_g = 1.68\times10^{-8}$ Ωm, ρ_e = 100 Ωm and ε_r = 1

5.2.1 Lightning to a pole of a distribution line

Figure 5.30 illustrates a model circuit for lightning surge simulation in EMTP [1]. The line configuration and parameters are given in Figure 5.29. For the pole: surge impedance $Z_t = 200\,\Omega$, propagation velocity $c_t = 300\,\text{m/}\mu\text{s}$, and footing resistance $R_f = 85\,\Omega$ (10 Ω). The model circuit corresponds the test circuit in reference [119]. The pole and overhead line are modeled by CP and WB models.

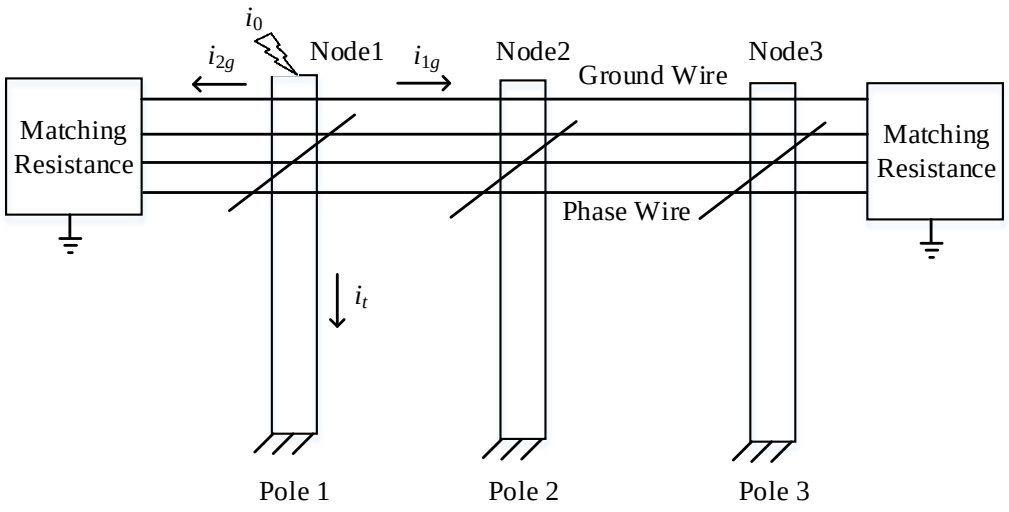

Figure 5.30: Model circuit for a step current simulation

Lightning to the first pole (Node1) is represented by a normalized current $i_0 = 1\,\text{A}$ with a step function.

Figure 5.31 shows (a) voltage surge v_{1g} at the top of the first pole (Node1), (b) voltage v_{1a} of phase - *a* at Node1 and (c) currents i_t, i_{1g} and i_{2g}. No significant difference is observed in the calculated results by the extended and classical TL approaches in Figure 5.31. A difference of few volts at the initial part of induced voltage v_{1a} is observed.

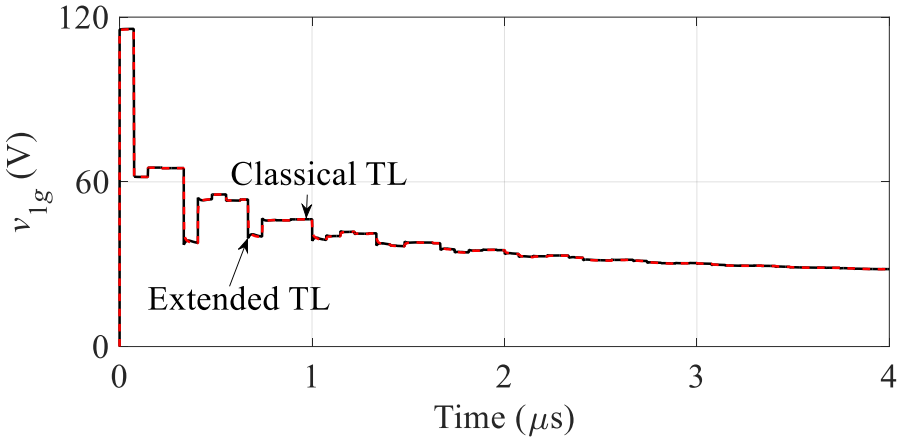

(a) Ground wire (pole top) voltage

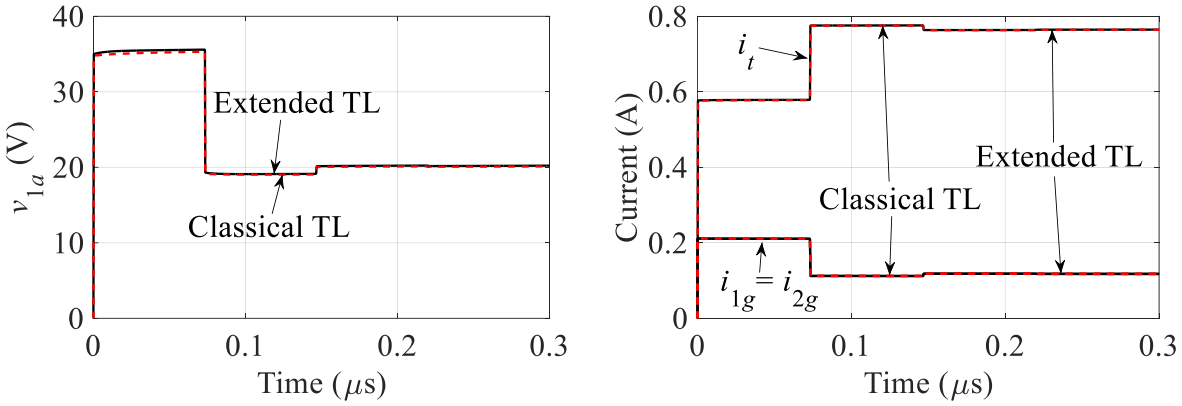

(b) Induced voltage to phase - *a* (c) Currents

Figure 5.31: Step surge voltages and currents at Node1

5.2.2 Lightning to a pole next to a customer

In reality, the lightning current is not a step function, but it is an impulse wave with front time T_f and tail T_t. Figure 5.32 illustrates a test circuit when a lightning impulse current with rise time $T_f = 1\,\mu s$ and wave tail $T_t = 20\,\mu s$ is applied to the pole in Figure 5.32. The right-hand side of the pole is connected to a customer house with home appliances [119].

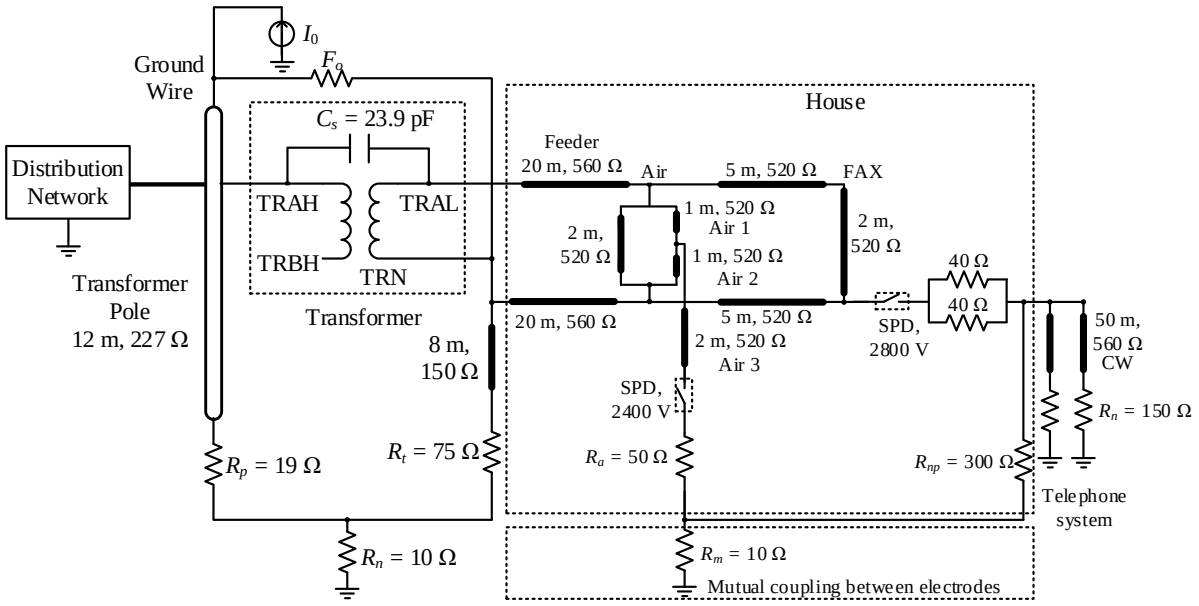

Figure 5.32: Test circuit of lightning and its path to house, F_o: flashover between the pole and transformer neutral wire

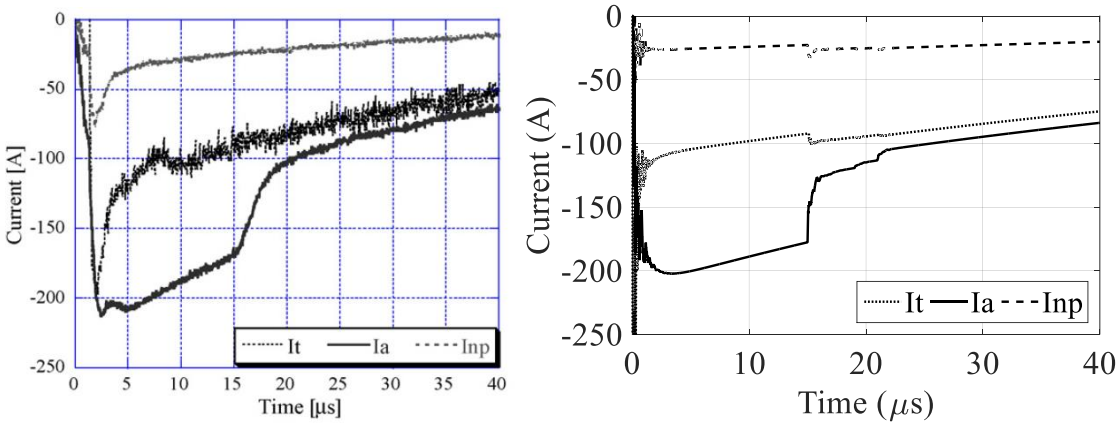

(a) Test results [119] (b) EMTP simulation result

Figure 5.33: Comparison of lightning surge by test and simulation results

Figure 5.33 shows the experimental and EMTP simulation results. The currents flowing through the grounding resistance R_t, R_a and R_{np} reach $i_{t\max} = 200$ A, $i_{a\max} = 220$ A and $i_{np\max} = 75$ A, respectively. The results agree reasonably well with the test results [119].

Because the frequency components involved in the transients are lower than 1 MHz, no significant difference is observed between the extended and classical TL approaches as observed in Figure 5.33 (b). The EMTP simulation results show a reasonable agreement with the measured results. Also, a higher accuracy than the simulation results in reference [119] is observed.

5.3 Switching surges on an underground cable

5.3.1 Energization of propagation modes

Figure 5.34 illustrates simulation circuits for cable energization corresponds to the coaxial, inter-sheath and earth-return modes. Cable 1 in Figure 4.18 (a) is adopted in this section.

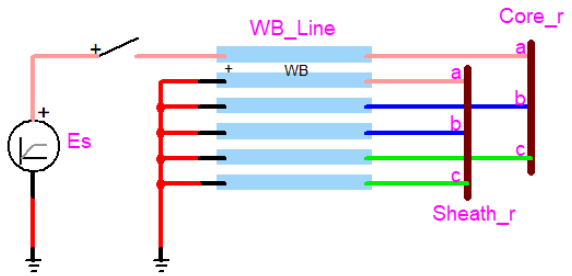

(a) Coaxial mode

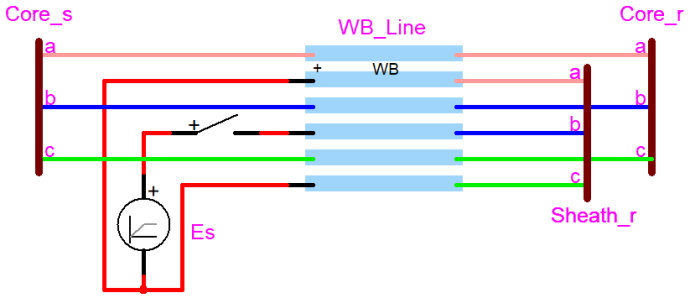

(b) Inter-sheath mode

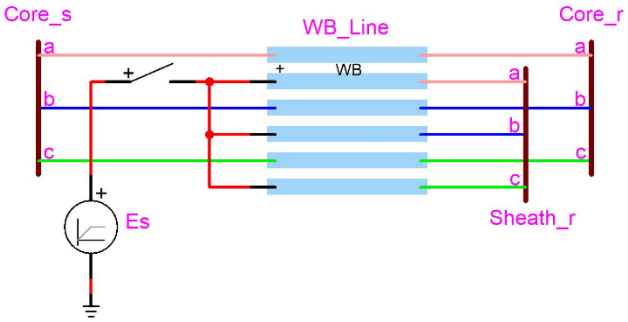

(c) Earth-retun mode

Figure 5.34 Simulation circuits for energization of modes with cable length *x*

5.3.1.1 Coaxial mode

Simulation results for coaxial mode energization by extended and classical TL approaches are shown in Figure 5.35 when a step voltage source $E_s = 1\,\text{kV}$ is applied to the circuit in Figure 5.34 (a). As expected, no difference is observed between extended and classical TL approaches.

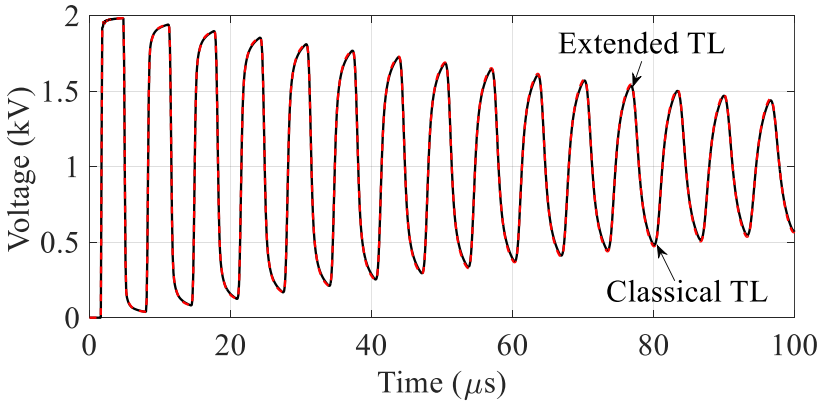

Figure 5.35: Phase - *a* core voltage at the receiving end for coaxial mode energization with *x* = 263 m

5.3.1.2 Inter-sheath mode

Figure 5.36 shows transient sheath voltages of phase - *b* when a step voltage source $E_s = 1\,\text{kV}$ is applied to the circuit in Figure 5.34 (b). Because of the higher attenuation of the inter-sheath mode (see Figure 4.32 (a)), the transient sheath voltages by the extended TL approach are damped faster than those by the classical one. Thus, the waveforms by the extended one are smoothly converging to the steady-state voltage 0.667 kV, i.e. $2E_s/3$ determined by the inter-sheath mode circuit in Figure 5.34 (b). In the case of $\rho_e = 100\,\Omega\text{m}$, the time delay τ is estimated in Figure 5.36 (a) as $\tau = 6.3\,\mu\text{s}$ and $\tau' = 7.8\,\mu\text{s}$, where τ and τ' are extended and classical approaches, respectively.

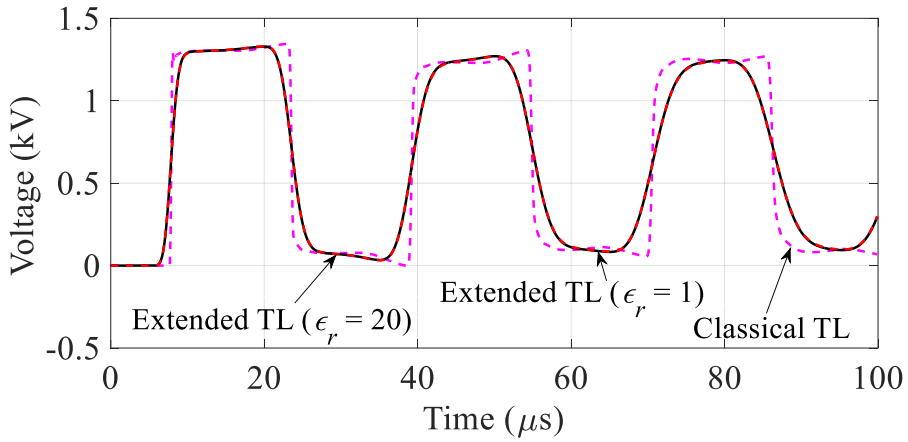

(a) ρ_e = 100 Ωm

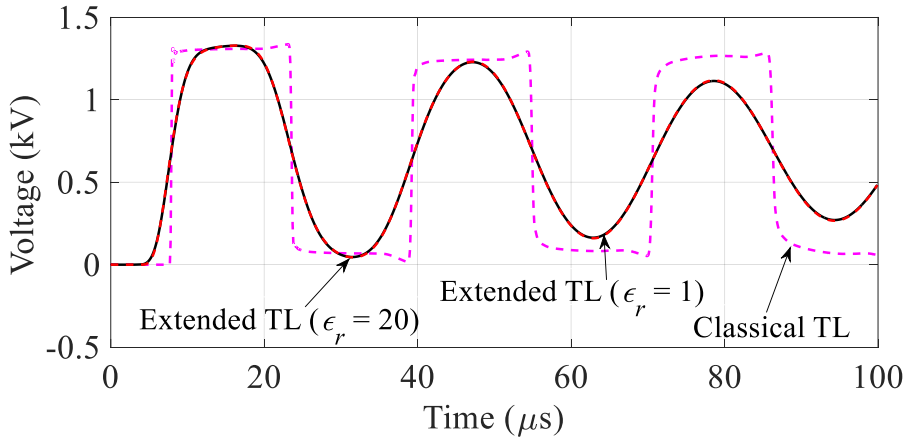

(b) ρ_e = 500 Ωm

Figure 5.36: Phase - *b* sheath voltage at the receiving end for inter-sheath mode energization with *x* = 263 m

Since the cable length is $x = 263\,\text{m}$, the propagation velocity c becomes $c = 41.7\,\text{m/μs}$ and $c' = 33.7\,\text{m/μs}$, where c and c' are extended and classical approaches, respectively. The velocity corresponds to the value at about $f = 2\,\text{MHz}$ in Figure 4.32 (b).

In the case of $\rho_e = 500\,\Omega\text{m}$ in Figure 5.36 (b), the higher attenuation and faster propagation velocity are clearly observed in comparison with Figure 5.36 (a). Also, no significant differences between $\varepsilon_r = 1$ and 20 are observed.

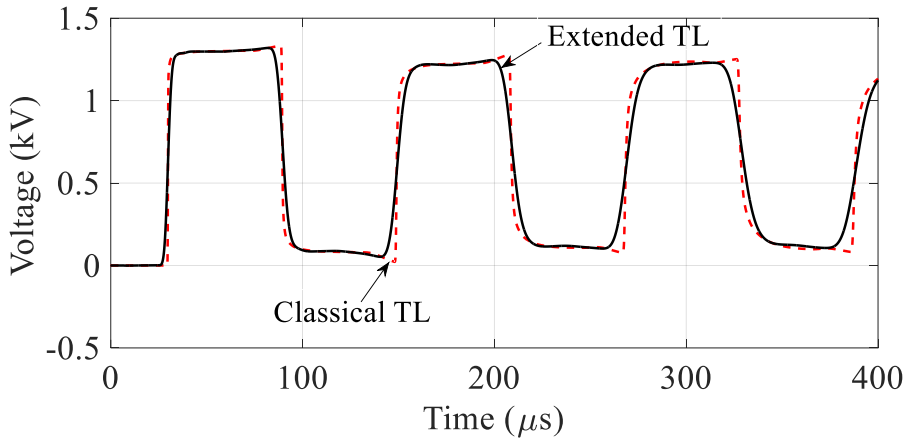

Figure 5.37: Phase - *b* sheath voltage at the receiving end for inter-sheath mode energization with ρ_e = 100 Ωm, ε_r = 1 and x = 1 km

Figure 5.37 shows the simulation results with the length $x = 1\,\text{km}$ and $\rho_e = 100\,\Omega\text{m}$. A noticeable difference is observed between the results by the extended and classical TL approaches especially at the time when a travelling wave arrives at the receiving end. In this case $\tau = 27.9\,\mu\text{s}$, $\tau' = 29.6$ μs, $c = 35.9\,\text{m/μs}$ and $c' = 33.7\,\text{m/μs}$.

5.3.1.3 Earth-return mode

Figure 5.38 (a) shows phase - *a* sheath voltage at the receiving end for the observation time 250 μs, when a step voltage source $E_s = 1\,\text{kV}$ is applied to the three phase sheaths which are short-circuited at the sending end as shown in Figure 5.34 (c).

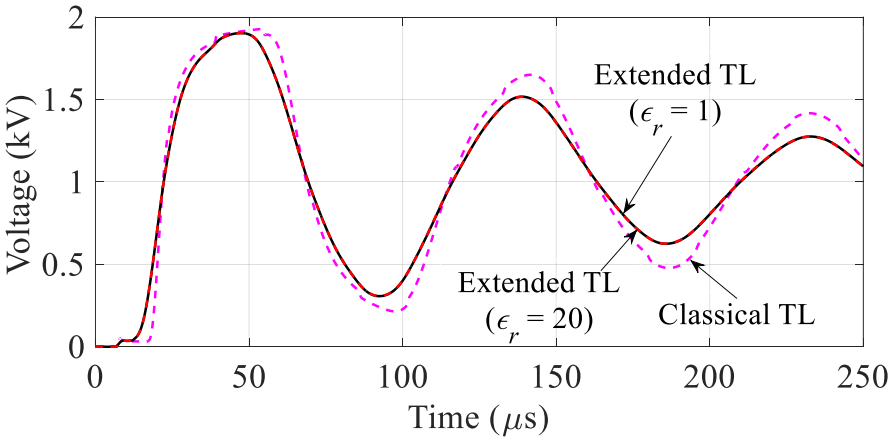

(a) Phase - *a* with *t* = 250 µs

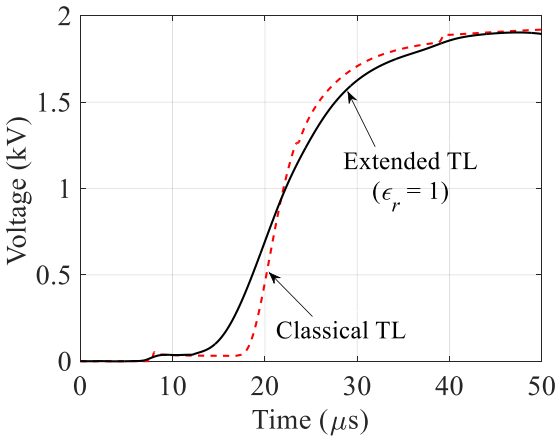

(b) Phase - *a* = Phase - *c* with *t* = 50 µs

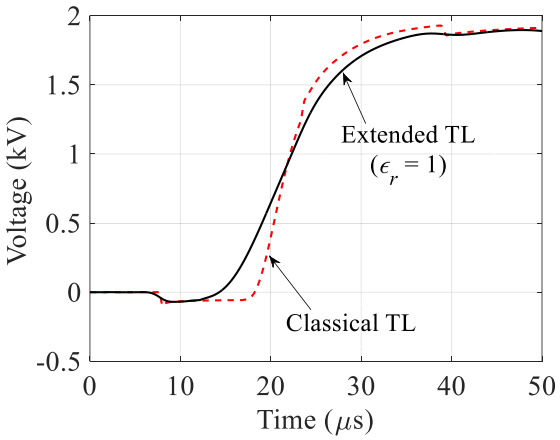

(c) Phase - *b* with *t* = 50 µs

Figure 5.38: Sheath voltages at the receiving end for earth-return mode energization with ρ_e = 100 Ωm and *x* = 263 m

Similarly, to the inter-sheath mode energization in the previous section, the sheath voltage calculated by the extended approach is more attenuated than that by the classical one, and reaches the steady-state voltage E_s, much faster. A similar observation can be made on the propagation velocity in the inter-sheath mode case in the previous section. It should be noted that a small voltage less than 100 V appears at around 6 µs, before the earth-return wave arrives at the receiving end after 10 µs. Figure 5.38 (b) and (c) show phase - *a* and phase - *b* sheath voltages at the receiving end for the observation time of 50 µs. It is clear in Figure 5.38 (b) that the phase - *a* and phase - *c* voltages are the same with the positive polarity, while that of phase - *b* in Figure 5.38 (c) is twice

of the phase - *a* voltage with the negative polarity. The velocity corresponds to that given in previous section, i.e. the inter-sheath mode. It is well-known in the field of surge measurement that the earth-return mode cannot be completed by short-circuiting the three phases at the sending end. A typical field test on a 500 kV transmission line is described in reference [120]. About 28% of the earth-return mode voltage was measured on phases at the receiving end as the inter-phase mode voltage. In Figure 5.38 (b), about 5% of the earth-return mode voltage appears on the phases - *a* and - *c*, and about 10% appears on phase - *b* (middle phase) with the negative polarity in Figure 5.38 (c). Because of the more balanced impedances in the cable in Figure 4.18 (a), the result is reasonable compared with 28% in the 500 kV un-transposed vertical twin circuit line. If a complete earth-return mode is necessary, the three phase sheaths at the receiving end should be short-circuited. The velocity of the earth-return mode in Figure 5.38 is observed as $c = 19.6\,\text{m/}\mu\text{s}$ and $c' = 14.7\,\text{m/}\mu\text{s}$. These velocities correspond to those at about $f = 300$ to 400 kHz in Figure 4.32 (b).

5.3.2 Energization of a cross-bonded cable

In this section, switching surges on a cross-bonded cable are investigated.

5.3.2.1 Sheath bonding methods

The sheath of a single core cable for ac service acts as a secondary of a transformer. The current in the conductor induces a voltage in the sheath. When the sheaths of cables are bonded to each other, the induced voltage causes current to flow in the completed circuit [5]. This current causes losses in the sheath. Various methods of bonding may be used, and must perform the following functions [5]:

- Limit sheath voltages as required by the sheath sectionalizing joints.
- Reduce or eliminate the sheath losses.
- Maintain a continuous sheath circuit to permit fault-current return, and adequate lightning and switching surge protection.

To satisfy these requirements either fully or partially, the cable sheaths are divided into a number of sections by means of sheath sectionalizing joints. The length of these sections is determined by the permissible sheath voltage levels for normal and fault conditions.

5.3.2.1.1 Single point bonding

Figure 5.39 shows a typical configuration of single point bonding. It is the simplest form of bonding consists in arranging for the sheaths of the three cables to be connected and grounded at one point only along their length. At all other points, a voltage will appear from sheath to ground that will be a maximum at the farthest point from the ground bond. The sheaths must therefore be adequately insulated from ground. Since there is no closed sheath circuit, except through the sheath voltage limiter (leakage current), current does not normally flow longitudinally along the sheaths and no sheath circulating current loss occurs (sheath eddy loss will still be present). This is typically suitable for cable sections less than 500 m, or one drum length.

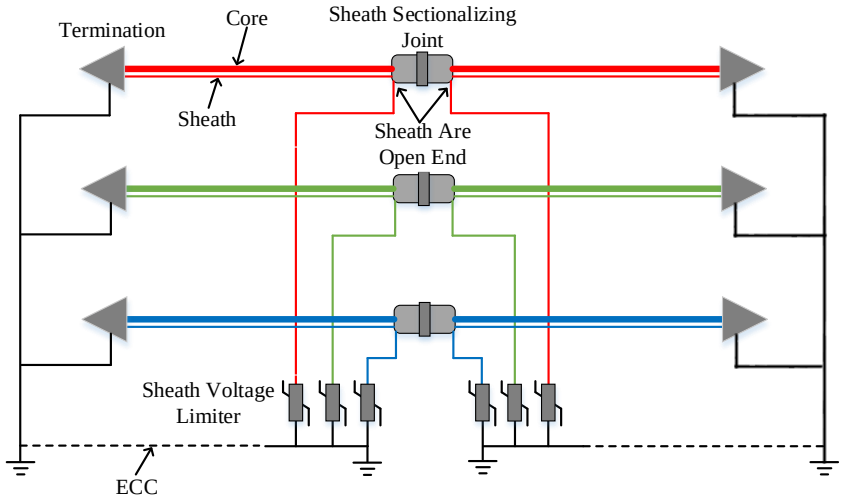

Figure 5.39: Single point bonding (two sections) with ECC and SVL [5]

The functions of earth continuity cable (ECC) and sheath voltage limiter (SVL) can be also clarified [5]. During a ground fault on the power system, the zero-sequence current carried by the cable conductors returns by whatever external paths are available. Since a single point bonded cable sheath is grounded at one position only, it cannot, except in the case of a cable fault, carry any of the returning current. This being so, unless some parallel external conductor is available or is provided to serve as an alternative path, the return current can flow only by way of the ground itself. Accordingly, it is recommended that a single point bonded cable installation be provided with a parallel earth continuity cable that is grounded at both ends of the route. The size of this conductor must be adequate to carry the full expected fault current for the cable system.

Also, the SVLs, which protect sheath insulators and cable jackets, are designed to limit [5]:

– Transient voltages associated with lightning.

– Switching surges.

– Fault initiation.

The use of SVLs is intended to reduce the problems of failures of sheath insulators and cable jackets encountered in the installations. For the single point bonding, the SVLs are connected between the un-bonded ends of the cable sheaths and ground.

5.3.2.1.2 Cross bonding

Cross bonding consists essentially in sectionalizing the sheaths into minor sections and cross connecting them so as to approximately neutralize the total induced voltage in three consecutive sections (three equal length sections), as shown in Figure 5.40.

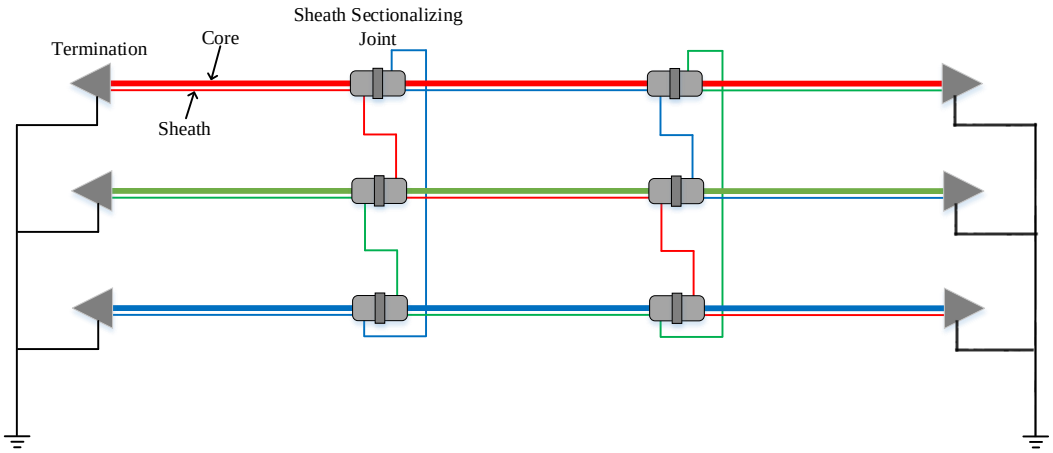

Figure 5.40: Cross bonding without core transposition, a major section [5]

Unlike the single point bonding, the sheath circuit on the left circuit is connected to the sheath circuit of a different phase cable on right side as shown in Figure 5.40. The main advantage of cross bonding is that the induced sheath currents are limited during the normal load operation, and the sheaths form a continuous path from end to end of the cable circuit and are grounded at both ends [5]. Because the sheath current can flow during ground faults, thus ECC can be removed and give economic advantage. Also, the sheath becomes a more effective screening conductor for ground faults, hence, the voltage induced in parallel cables is less during ground faults in a cross bonded system than a single point bonded system.

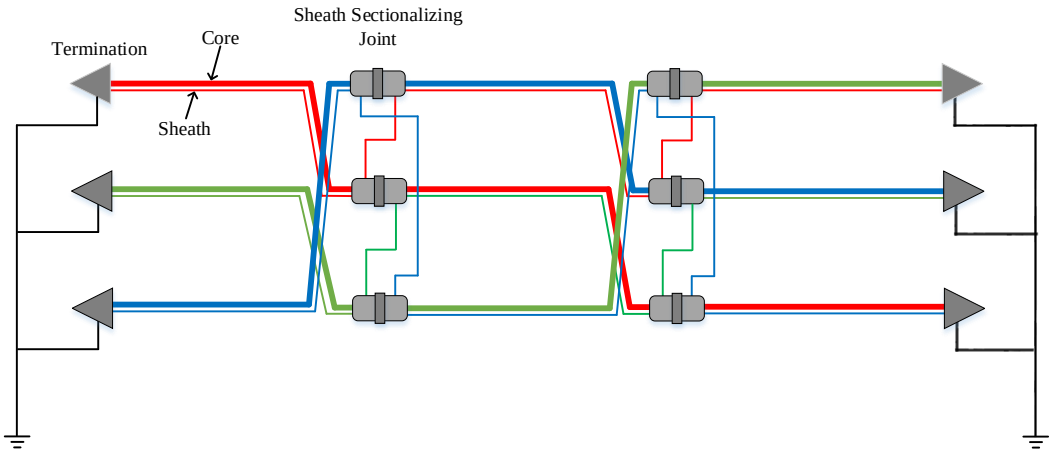

Figure 5.41: Cross bonding with core transposition, a major section [5]

With un-transposed cables, it is impossible to achieve an exact balance of induced sheath voltages unless the cables are laid in trefoil. When the cable cores are transposed at each joint position, as shown in Figure 5.41, the induced sheath voltages will be neutralized irrespective of cable formation. However, the main difficulty of cable with core transposition is that how to do the cable crossing, and still obtain distance between the cables to ensure proper heat dissipation. In case the cables are closer to each other at the point of crossing there is introduced a bottleneck for the ampacity of the line.

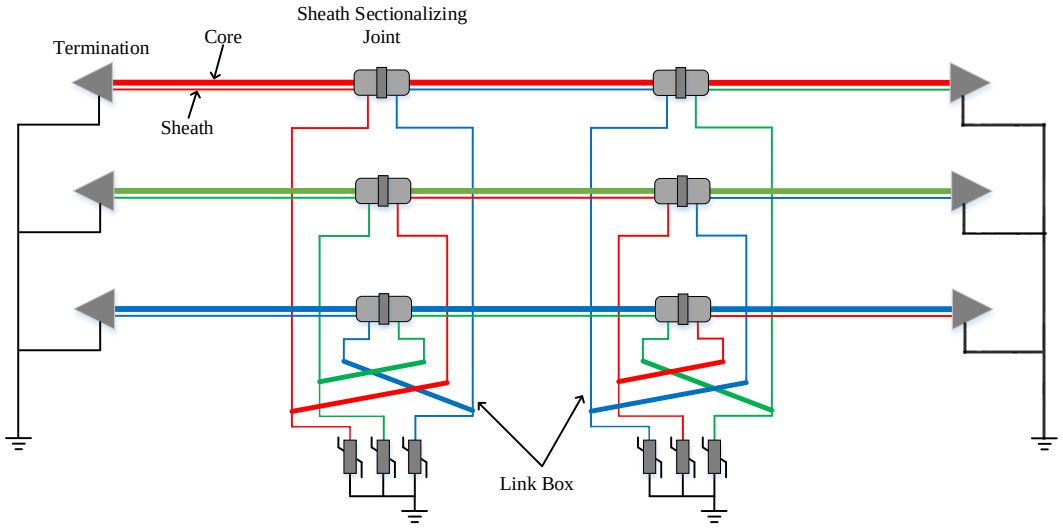

Figure 5.42: Cross bonding without core transposition, a major section with link box and SVLs [5]

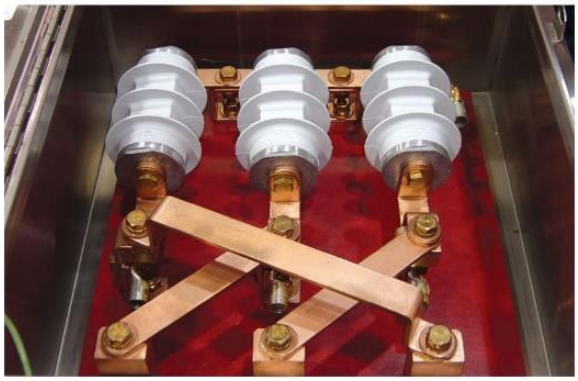

Figure 5.43: Link box with cross bonding connection and SVLs [96]

Although the continuous sheath voltage is suppressed by the small sheath current and the balanced sheath voltage, the minor section sheath voltage cannot be suppressed by the cross bonding [5]. Thus, in order to against the minor section sheath voltage, the SVLs are installed at sheath sectionalizing joint via link box, as shown in Figure 5.42. Figure 5.43 shows a structure of a typical link box, and SVLs are normally arranged by a star connection.

5.3.2.2 Energization of a major section

Figure 5.44 illustrates a field test circuit on a 110 kV cross-bonded cable [5], [121]. Cable 2 is adopted and the geometry is shown in Figure 4.18. A 7.3 kV impulse voltage with wave front duration $T_f \approx 0$ and wave tail $T_t = 40\,\mu s$ is applied to the middle phase - core at the sending end. Figure 5.45 shows the measured results (re-drawn from photos [121] recorded by an analog oscilloscope) and Figure 5.46 is EMTP simulation results of three measured points shown in Figure 5.44 by the extended and classical TL approaches.

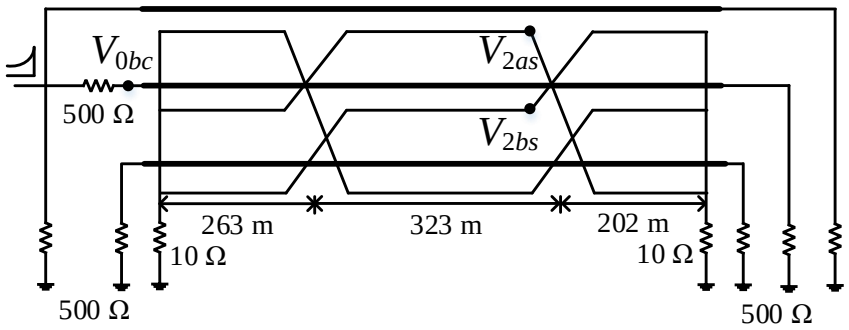

Figure 5.44: Test circuit for Cable 2 with a major section shown in Figure 5.40, ρ_e = 100 Ωm and ε_r = 1

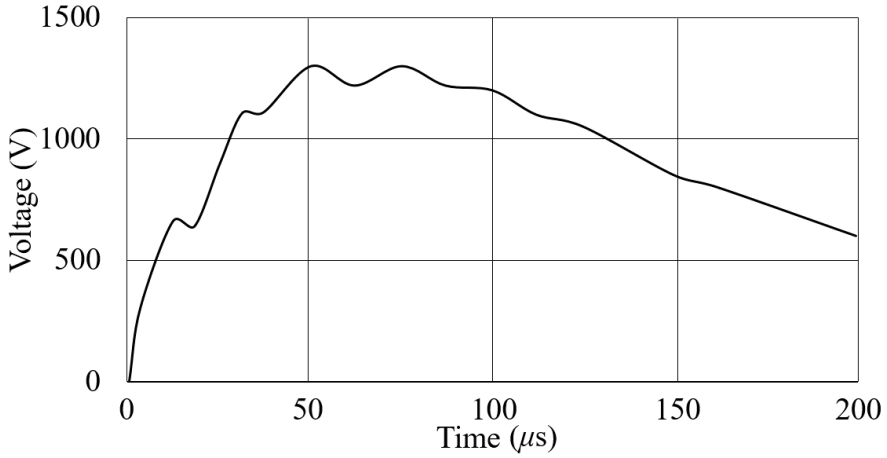

(a) V_{0bc}

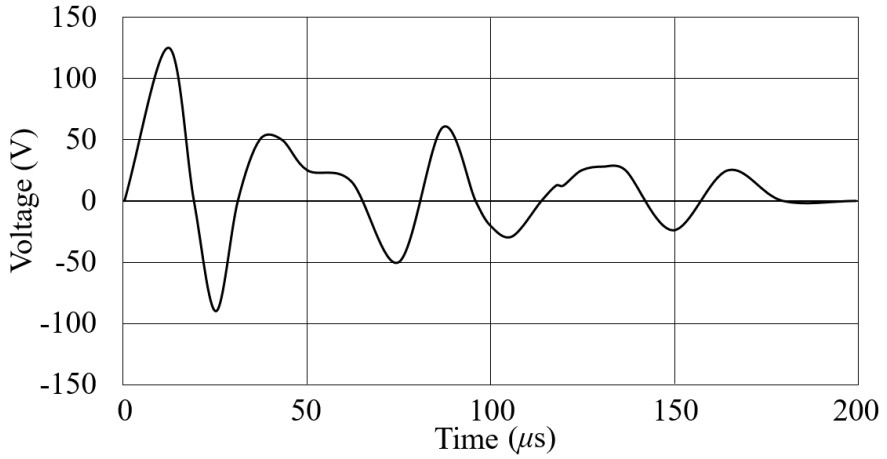

(b) V_{2as}

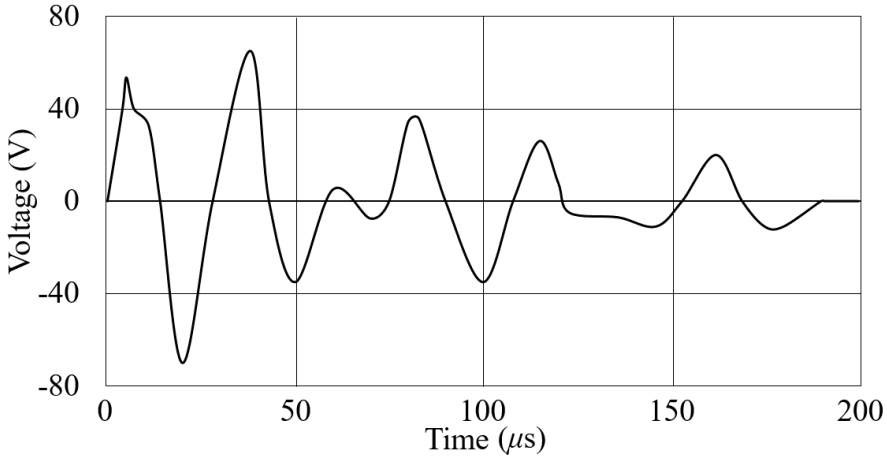

(c) V_{2bs}

Figure 5.45: Field test results on the cable in Figure 5.44

The simulation results in Figure 5.46 show reasonable agreement with the field test results. However, more high frequency components are observed in the waveforms calculated by the classical TL approach, but not observed in extended TL approach and field test results. Note that it was a common practice to use a damping circuit to eliminate noise when surges were measured by the analog oscilloscope.

Because the shortest length of a minor section is 202 m, the highest transient frequency due to the minor section is estimated to be about 200 kHz. In this frequency region, no significant influence of the proposed approach compared with the classical approach is expected, as in Figure 4.33. Thus, this measured result does not achieve the purpose of demonstrating the advantages of the proposed approach versus the classical approach. It is required to perform different experiments and corresponding measurements in the future.

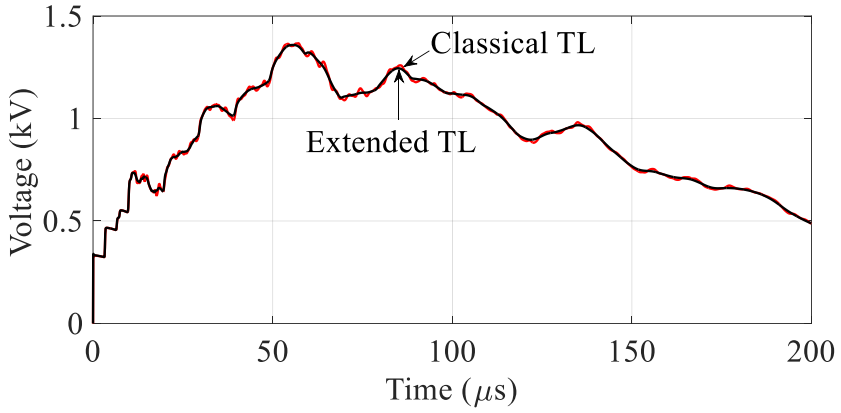

(a) V_{0bc}

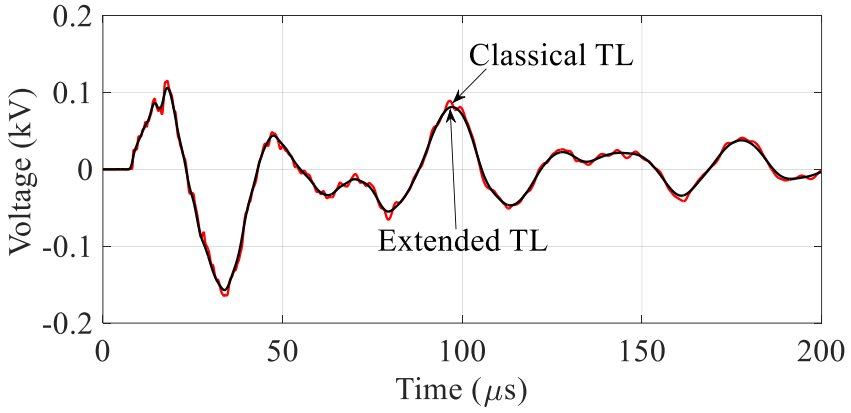

(b) V_{2as}

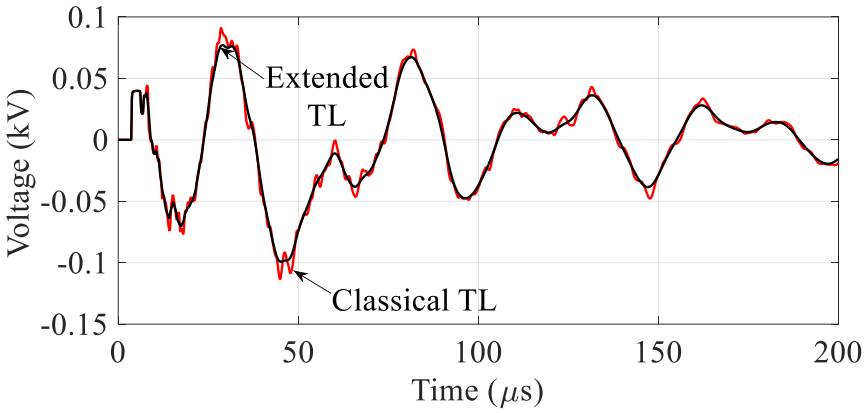

(c) V_{2bs}

Figure 5.46: EMTP simulation results on the cable in Figure 5.44

5.3.2.3 Energization of three cascaded major sections

Three major sections of Figure 5.44 are cascaded. The three phase sheaths are short-circuited and grounded at the sending end, and at the end of each major section by $R_g = 10\,\Omega$. A 110 kV AC source is sequentially applied to the sending end of cable with closing time: phases - *a* $t = 0$, - *b*: $t = 0.1$ and - *c*: $t = 0.2$ ms. Figure 5.47 shows the three phase core and sheath voltages at the receiving end of the cable. As expected, no differences in the core voltages are observed between classical and extended TL approaches. Because of sequential energization, the sheath voltage involves various modes. A noticeable difference between classical and extended approaches is observed. Extended approach shows a higher damping as explained in the previous sections.

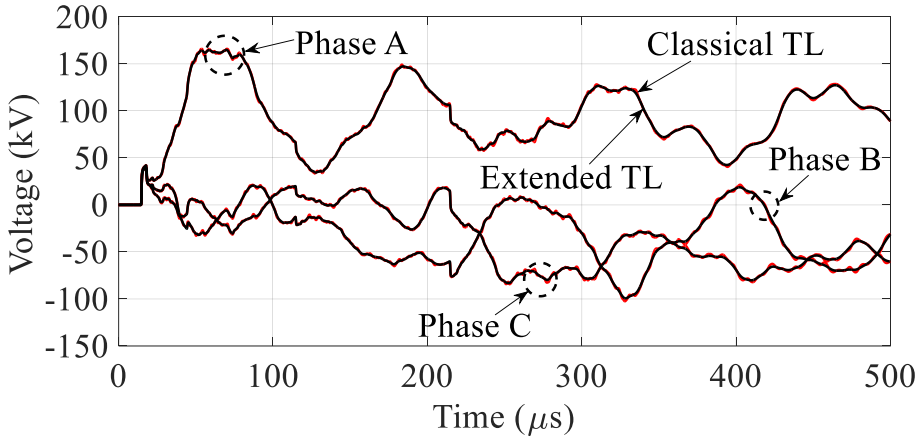

(a) Three phase core voltages at the receiving end

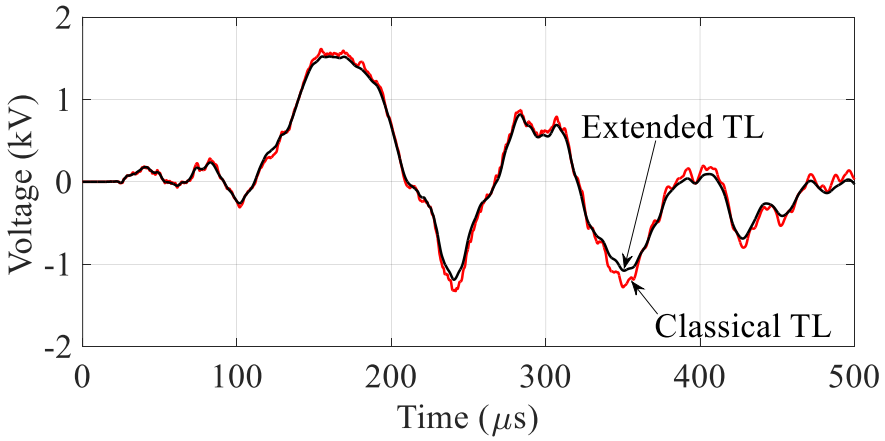

(b) Sheath voltage at the receiving end

Figure 5.47: Core and sheath voltages at the receiving end of the cross-bonded cable in Figure 5.44, ρ_e = 100 Ωm and ε_r = 1

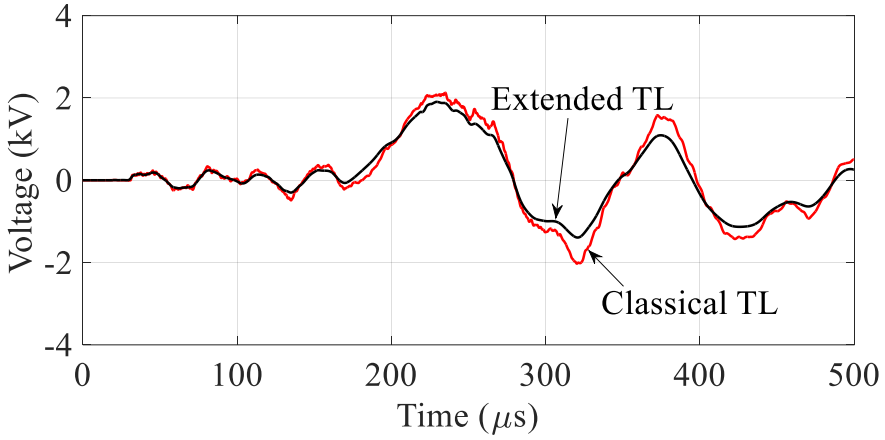

Figure 5.48: Sheath voltage at the receiving end of the cross-bonded cable in Figure 4.18 (a), ρ_e = 100 Ωm and ε_r = 1

Figure 5.48 shows the sheath voltage at the receiving end if the Cable 1 shown in Figure 4.18 is adopted. The differences between classical and extended TL approaches are more visible in the flat cable than that in the vertical one shown in Figure 5.47.

5.4 Concluding remarks

In this chapter, transient simulations are performed and investigated for a simple GIB, a full 500 kV GIS, a three phase distribution line and a three phase single core cable system.

For a simple GIB transient simulation, the lower attenuation of extended TL approach at high frequencies results in a spike-like voltage. Also, the high frequency components in the transient waveform cannot be quickly damped. Such behavior cannot be observed in the classical TL approach.

By adopting the extended TL approach, very fast transients in a full 500 kV gas-insulated substation is investigated and the following conclusions can be made.

- The classical TL approach may show numerical instability for VFT simulations in GISs.
- The VFT oscillating frequency decreases as the GIS total length increases. The frequency is decreased easily by less than a half by stray capacitances of transformers and bushings in the GIS, because those are far greater than the bus capacitance.
- The pipe grounding reduces the pipe voltage significantly, but the core voltage tends to increase as the grounding resistance becomes smaller. The grounding causes only minor influence on the oscillating frequency.
- The position of an operating DS causes a very significant effect on the VFT overvoltages and oscillating frequency. The distance to the open-circuited remote end from the DS is short, the overvoltage and frequency become very high. The DS charging condition is less influential than the position of an operating DS.
- The effect of spacers is similar to that of a transformer stray capacitance, but the effect is less noticeable for the smaller capacitance of the spacers.
- The analytical formulas show a satisfactory agreement with EMTP results, and are expected to be useful to a rough estimate of the VFT characteristics.
- Measured switching surges in GISs show frequency components from some MHz up to 140 MHz, which agree with those calculated by the extended TL approach.

Moreover, lightning surges on an overhead distribution line are calculated by EMTP and compared with the experimental results. Due to low frequency components, there is no significant difference between extended and classical TL approaches.

Transient simulations on underground cables including a field test are also performed and investigated.

- A significant difference of waveforms for inter-sheath and earth-return modes is observed between the extended and classical TL approaches.
- No difference is observed for waveforms of the coaxial mode on a cable between two approaches.
- Earth resistivity shows important effect on the transient waveforms of inter-sheath and earth-return modes. The effect of earth permittivity is negligible.
- The cable arrangement shows minor influence on core and sheath voltages.
- The extended TL approach is validated with a 110 kV cross-bonded cable.
- It is confirmed that the extended TL approach results in higher damping and smooth convergence to the steady-state compared with those calculated by classical TL approach.

CHAPTER 6 CONCLUSIONS

6.1 Summary of thesis

The main objective of this thesis is to derive new and generalized earth-return impedance and admittance formulas for an overhead line and an underground cable. Then, the wave propagation characteristics in frequency domain and transient simulations in time domain are performed and investigated by adopting the newly proposed formulas. The most important remarks of this thesis are summarized in the following categories.

- Formulation of electromagnetic field components and derivation of earth-return impedance and admittance formulas

In this thesis, complete electromagnetic field components radiated from an overhead line and an underground cable are formulated. Based on the proposed electromagnetic field components, new and generalized earth-return impedance and admittance formulas of the overhead line and the underground cable are derived. Because the proposed formulas are based on the complete field solution, no pre-condition is made except the thin wire assumption of a conductor. Since the complete field solution involves numerical complexity, quasi-TEM based earth-return impedance and admittance formulas are also proposed. Furthermore, approximate earth-return impedance and admittance formulas of the underground cable are given. The formulas with a closed form include no Sommerfeld integrals, and thus the numerical calculation of complex integrals, which often result in numerical instability, is avoided.

Also, the derived earth-return impedance and admittance formulas are discussed in comparison with existing formulas. The existing formulas of impedance and admittance can be deduced from the generalized formulation by considering the same assumption of initial and boundary conditions. Moreover, the inaccuracies of all the existing formulas are made clear.

A modified earth-return Green function of MoM-SO for overhead lines and cables is also derived. It is clear that the numerical instability of current MoM-SO can be eliminated by adopting the derived earth-return Green function.

- Definition of extended TL approach and classical TL approach

By adopting the complete earth-return impedance and admittance, an extended TL approach is proposed. The method implemented into the current EMTP is called as “classical TL approach”.

– Investigations of wave propagation characteristics in frequency domain

The frequency dependent characteristics of the series impedance, shunt admittance and propagation constants on an overhead line, an overhead cable and an underground cable are studied. It should be noted that the earth resistivity shows important influence on the shunt admittance composed of the earth-return admittance.

For an overhead line / cable, it is shown that the attenuation by the classical TL approach monotonously increases as a function of frequency, while the extended TL approach shows mode transition from a low frequency quasi-TEM (earth-return wave) propagation mode to a high frequency Sommerfeld-Goubau (surface wave) propagation mode. At high frequencies, the attenuation evaluated by the extended TL approach is much lower than the one found from the classical TL approach. The lower attenuation at high frequencies results in a larger amplitude for the propagation function.

Based on the investigations on an overhead line, the axial electric field shows a significant frequency dependence. The axial electric field at the conductor surface is much smaller than that near the earth surface at low frequencies. At frequencies above some MHz, it starts to decrease similarly to that near the earth surface, and then it increases as frequency increases in the high frequency region. This characteristic is found to be very similar to that of the attenuation constant known as “mode transition”. This effect cannot be observed in the classical TL approach.

By adopting the extended TL approach, it is shown that the attenuation and the propagation velocity of an underground cable are higher than those calculated by the classical TL approach, and the reason is the frequency-dependence of the earth-return admittance. The configuration of the cable shows less influence on wave propagation characteristics.

– Investigations of transient simulations in time domain

The studies of transient simulations in EMTP are based on extended and classical TL approaches.

A 500 kV GIS has been adopted to perform an analysis of switching surges. A spike-like voltage has been observed at every wave-front of switching surges if the extended TL approach is adopted. Also, high frequency components appear in the surge waveforms calculated by the extended TL

approach. However, surge waveforms calculated by the classical TL approach show lower frequency components, because higher frequency components are dumped out by the higher attenuation. Moreover, the classical approach shows often numerical instability in VFT simulations in GISs.

Next, VFTs studies based a full 500 kV GIS model are presented. It should be noted that only the extended TL approach is used to model the system in EMTP. Based on the investigations, the VFT oscillating frequency is significantly proportional to the GIS length and transformer stray capacitances. For example, the frequency decreases as the GIS total length increases. Also, the grounding of the GIB pipe has less influence on the oscillating frequency of the VFT. It should be noted that the VFT waveforms and oscillating frequency are strongly dependent on the conditions of operating DS. The spacers show minor influence on the VFT.

A lightning surge on a 6.6 kV overhead distribution line is also investigated. However, no significant differences have been observed between the extended and classical TL approaches. The reason comes from the lower frequency components involved in the transients.

Energization surges of propagation modes and cross-bonded cable by adopting the extended and classical TL approaches are also studied. The transient responses of the earth-return and inter-sheath modes evaluated by the extended TL approach show higher damping than the responses by the classical TL approach. A difference of the sheath voltage due to a sequential energization on a cross-bonded cable is also observed between the extended and classical approaches. It is made clear that the earth-return admittance adopted in the extended TL approach causes a noticeable difference.

6.2 Future works

Considering the general scope of this thesis, the following future works are summarized.

- Investigation of series impedance and shunt admittance for non-homogenous line / cable

In the derived formulas of an overhead line and an underground cable, the line/cable length is assumed to be infinite. Also, the conductors are parallel with each other. Thus, the accurate evaluation of parameters for the line and cable with finite length and non-parallel configuration require further studies on the impedance/admittance formulas, wave propagation characteristics and transient responses.

– Numerical electromagnetic method for the calculation of the shunt admittance

The proposed formulas of the shunt admittance are based on the analytical solution. It neglects the proximity effects for the shunt admittance. Therefore, it may be important to produce a numerical electromagnetic method for the calculation of the shunt admittance.

– Further validations with field test results

For any newly proposed model, a comparison with field test results is the best way to validate its availability and feasibility. In this thesis, the extended TL approach is validated by existing methods such as existing analytical formulas and MoM-SO method. However, the extended TL approach should be validated in comparison with field test results in the future.

BIBLIOGRAPHY

[1] J. Mahseredjian, S. Dennetière, L. Dubé, B. Khodabakhchian and L. Gérin-Lajoie, "On a new approach for the simulation of transients in power systems," Electric Power Systems Research, vol. 77, no. 11, pp. 1514-1520, 2007.

[2] A. Ametani (Editor), Numerical Analysis of Power System Transients and Dynamics, IET, Power & Energy Monogram Series 78, 2015.

[3] A. Ametani, "A general formulation of impedance and admittance of cables," IEEE Trans. Power Apparatus and Systems, vol. 99, no. 3, pp. 902-910, 1980.

[4] A. Ametani, N. Nagaoka, Y. Baba, T. Ohno and K. Yamabuki, Power System Transients Theory and Applications, New York: CRC Press, 2016.

[5] A. Ametani, T. Ohno and N. Nagaoka, Cable System Transients: Theory, Modeling and Simulation, Wiley-IEEE Press, 2015.

[6] J. R. Carson, "Wave propagation in overhead wires with ground return," The Bell System Technical Journal, vol. 5, no. 4, pp. 539-554, 1926.

[7] F. Pollaczek, "Uber das feld einer unendlich langen wechselstrom durchlossenen einfachleitung," Electrische Nachrichtentechnik, vol. 3, pp. 339-359, 1926.

[8] R. G. Olsen and T. A. Pankaskie, "On the exact, Carson and image theories for wires at or above the earth's interface," IEEE Trans. Power Apparatus and Systems, vol. 102, no. 4, pp. 769-778, 1983.

[9] E. D. Sunde, Earth Conduction Effects in Transmission Systems, New York: Dover, 1968.

[10] C. H. Stoyer, "Electromagnetic fields of dipoles in stratified media," IEEE Trans. Antennas and Propagation, vol. 25, no. 4, pp. 547-552, 1977.

[11] L. M. Wedepohl and R. G. Wasley, "Wave propagation in multiconductor overhead lines - calculation of series impedance for multilayer earth," Proc. IEE, vol. 113, no. 4, pp. 627-632, 1966.

[12] I. S. Moghram, "Effects of earth stratification on impedances of power transmission lines," International Trans. Electrical Energy Systems, vol. 8, no. 6, pp. 445-449, 1998.

[13] L. Wedepohl and D. Wilcox, "Transient analysis of underground power - transmission systems," Proc. IEE, vol. 120, no. 2, pp. 253-260, 1973.

[14] D. Tsiamitros, G. Papagiannis, D. Labridis and P. Dokopoulos, "Earth return path impedances of underground cables for the two - layer earth case," IEEE Trans. Power Delivery, vol. 20, no. 3, pp. 2174-2181, 2005.

[15] D. Tsiamitros, G. Papagiannis and P. Dokopoulos, "Earth return impedances of conductor arrangements in multilayer soils - part I: theoretical model," IEEE Trans. Power Delivery, vol. 23, no. 4, pp. 2392-2400, 2008.

[16] D. A. Tsiamitros, G. C. Christoforidis, G. K. Papagiannis, D. P. Labridis and P. S. Dokopoulos, "Earth conduction effects in systems of overhead and underground conductors in multilayered soils," Proc. IEE - Generation, Transmission and Distribution, vol. 153, no. 3, pp. 291-299, 2006.

[17] W.H. Wise, "Propagation of high frequency currents in ground return circuits," Proc. IRE, vol. 22, no. 4, pp. 522-527, 1934.

[18] W. H. Wise, "Potential coefficients for ground return circuits," The Bell System Technical Journal, vol. 27, no. 2, pp. 365-371, 1948.

[19] M. Nakagawa, A. Ametani, and K. Iwamoto, "Further studies on wave propagation in overhead lines with earth return: impedance of stratified earth," Proc. IEE, vol. 120, no. 12, pp. 1521-1528, 1973.

[20] M. Nakagawa, "Admittance correction effects of a single overhead line," IEEE Trans. Power Apparatus and Systems, vol. 100, no. 3, pp. 1154-1161, 1981.

[21] M. Nakagawa, " Further studies on wave propagation along overhead transmission lines: effects of admittance correction," IEEE Trans. Power Apparatus and Systems, vol. 100, no. 7, pp. 3626-3633, 1981.

[22] A. Ametani, N. Nagaoka and R. Koide, "Wave propagation characteristics on an on overhead conductor above snow," Electrical Engineering in Japan, vol. 134, no. 3, pp. 26-33, 2001.

[23] T. Papadopoulos, G. Papagiannis, and D. Labridis, "Wave propagation characteristics of overhead conductors above imperfect stratified earth for a wide frequency range," IEEE Trans. Magnetics, vol. 45, no. 3, pp. 1064-1067, 2009.

[24] T. Papadopoulos, G. Papagiannis, and D. Labridis, "A generalized model for the calculation of the impedances and admittances of overhead power lines above stratified earth," Electric Power Systems Research, vol. 80, no. 9, pp. 1160-1170, 2010.

[25] A. Ametani, Y. Miyamoto, and J. Mahseredjian, "Derivation of an earth - return impedance of an overhead multi - conductor considering displacement currents," IEEJ Trans. Power and Energy, vol. 134, no. 11, pp. 936-940, 2014.

[26] A. Ametani, Y. Miyamoto, Y. Baba, and N. Nagaoka, "Wave propagation on an overhead multiconductor in a high - frequency region," IEEE Trans. Electromagnetic Compatibility, vol. 56, no. 6, pp. 1638-1648, 2014.

[27] A. Ametani, "Stratified earth effects on wave propagation - frequency dependent parameters," IEEE Trans. Power Apparatus and Systems, vol. 93, no. 5, pp. 1233-1239, 1974.

[28] A. H. Kikuchi, "Wave propagation on the ground return circuit in high frequency regions," IEE Japan Journal, vol. 75, no. 805, pp. 1176-1187, 1955.

[29] A. H. Kikuchi, "Electromagnetic fields on infinite wire at high frequencies above plane earth," IEE Japan Journal, vol. 77, no. 825, pp. 721-733, 1957.

[30] J. R. Wait, "The electromagnetic fields of a horizontal dipole in the presence of a conducting half - space," Canadian Journal of Physics, vol. 39, no. 7, pp. 1017-1028, 1961.

[31] J. R. Wait, "Theory of wave propagation along a thin wire parallel to an interface," Radio Science, vol. 7, no. 6, pp. 675-679, 1972.

[32] J. R. Wait, "Tutorial note on the general transmission line theory for a thin wire above the ground," IEEE Trans. Electromagnetic Compatibility, vol. 33, no. 1, pp. 65-67, 1991.

[33] G. Bridges, O. A. Atta and L. Shafai, "Solution of discrete modes for wave propagation along multiple conductors structures above a dissipative earth," Canadian Journal of Physics, vol. 66, no. 5, pp. 428-438, 1988.

[34] G. Bridges and L. Shafai, "Plane wave coupling to multiple conductor transmission lines above a lossy earth," IEEE Trans. Electromagnetic Compatibility, vol. 31, no. 1, pp. 21-33, 1989.

[35] L. M. Wedepohl and A. E. Efthymiadis, "Wave propagation in transmission lines over lossy ground - a new, complete field solution," Proc. IEE, vol. 125, no. 6, pp. 505-510, 1978.

[36] A. E. Efthymiadis and L. M. Wedepohl, "Propagation characteristics of infinitely - long single - conductor lines by the complete field solution method," Proc. IEE, vol. 125, no. 6, pp. 511-517, 1978.

[37] M. D'Amore and M. Sarto, "Simulation models of a dissipative transmission line above a lossy ground for a wide - frequency range - part I: single conductor configuration," IEEE Trans. Electromagnetic Compatibility, vol. 38, no. 2, pp. 127-138, 1996.

[38] M. D'Amore and M. Sarto, "Simulation models of a dissipative transmission line above a lossy ground for a wide - frequency range - part II: multiconductor configuration," IEEE Trans. Electromagnetic Compatibility, vol. 38, no. 2, pp. 139-149, 1996.

[39] P. Pettersson, "Propagation of waves on a wire above a lossy ground - different formulations with approximations," IEEE Trans. Power Delivery, vol. 14, no. 3, pp. 1173-1179, 1999.

[40] R. G. Olsen, E. F. Kuester and D. C. Chang, "Modal theory of long horizontal wire structures above the earth: 2, properties of discrete modes," Radio Science, vol. 13, no. 4, pp. 615-623, 1978.

[41] R. G. Olsen, J. L. Young and D. C. Chang, "Electromagnetic wave propagation on a thin wire above earth," IEEE Trans. Antennas and Propagation, vol. 48, no. 9, pp. 1413-1419, 2000.

[42] E. F. Kuester and D. C. Chang, "Modal theory of long horizontal wire structures above the earth: 1, excitation," Radio Science, vol. 13, no. 3, pp. 605-613, 1978.

[43] L. M. Wedepohl and D. J. Wilcox, "Transient analysis of underground power - transmission systems: system - model and wave - propagation characteristics," Proc. IEE, vol. 120, no. 2, pp. 253-260, 1973.

[44] T. Papadopoulos, D. Tsiamitros and G. Papagiannis, "Impedances and admittance of underground cables for the homogeneous earth case," IEEE Trans. Power Delivery, vol. 25, no. 2, pp. 961-969, 2010.

[45] T. Papadopoulos, D. Tsiamitros and G. Papagiannis, "Earth return admittances and impedances of underground cables in non-homogeneous earth," Proc. IEE - Generation, Transmission and Distribution, vol. 5, no. 2, pp. 161-171, 2011.

[46] T. Papadopoulos, D. Tsiamitros and G. Papagiannis, "Analytical study of the frequency-dependent earth conduction effects on underground power cables," Proc. IEE - Generation, Transmission and Distribution, vol. 7, no. 3, pp. 276-287, 2013

[47] O. Saad, G. Gaba, and M. Giroux, "A closed - form approximation for ground return impedance of underground cables," IEEE Trans. Power Delivery, vol. 11, no. 3, pp. 1536-1545, 1996.

[48] N. Theethayi, Y. Baba, F. Rachidi, and R. Thottappillil, "On the choice between transmission line equations and full - wave Maxwell's equations for transient analysis of buried wires," IEEE Trans. Electromagnetic Compatibility, vol. 50, no. 2, pp. 347-357, 2008.

[49] N. Theethayi, R. Thottappillil, M. Paolone, C. A. Nucci and D. Labridis, "External impedance and admittance of buried horizontal wires of transient studies using transmission line anlysis," IEEE Trans. Dielectrics and Electrical Insulation, vol. 14, no. 3, pp. 751-761, 2007.

[50] E. Petrache, F. Rachidi, M. Paolone, C. Nucci, V. A. Rakov, and M. A. Uman, "Lightning - induced voltages on buried cables - part I: theory, " IEEE Trans. Electromagnetic Compatibility, vol. 47, no. 3, pp. 498-508, 2005.

[51] F. A. Uribe, J. L. Naredo, P. Moreno and L. Guardado, "Algorithmic evaluation of underground cable earth impedances," IEEE Trans. Power Delivery, vol. 19, no. 1, pp. 316-322, 2004.

[52] X. Legrand, A. Xemard, G. Fleury, P. Auriol and C. A. Nucci, "A quasi - Monte Carlo integration method applied to the computation of the Pollaczek integral," IEEE Trans. Power Delivery, vol. 23, no. 3, pp. 1527-1534, 2008.

[53] F. A. Uribe and A. Ramirez, "Alternative series - based solution to approximate Pollaczek's integral," IEEE Trans. Power Delivery, vol. 27, no. 4, pp. 2425-2427, 2012.

[54] J. R. Wait, "Electromagnetic wave propagation along a buried insulated wire," Canadian Journal of Physics, vol. 50, no. 20, pp. 2402-2409, 1972.

[55] J. R. Wait, "Excitation of currents on a buried insulated cable," Journal of Applied Physics, vol. 49, no. 2, pp. 876-880, 1978.

[56] G. Bridges, "Fields generated by bare and insulated cables buried in a lossy half - space," IEEE Trans. Geoscience and Remote Sensing, vol. 30, no. 1, pp. 140-146, 1992.

[57] G. Bridges, "Transient plane wave coupling to bare and insulated cables buried in a lossy half-space," IEEE Trans. Electromagnetic Compatibility, vol. 37, no. 1, pp. 62-70, 1995.

[58] B. Zhang, J. Zou, X. Du, J. Lee and M. N. Ju, "Ground admittance of an underground insulated conductor and its characteristic in lightning induced disturbance problems, " IEEE Trans. Electromagnetic Compatibility, vol. 59, no. 3, pp. 894-901, 2017.

[59] A. Magalhaes, J. Silva, A. Lima and M. Correia de Barros, "Validation limits of Quasi - TEM approximation for buried bare and insulated cables," IEEE Trans. Electromagnetic Compatibility, vol. 57, no. 6, pp. 1690-1697, 2015.

[60] A. Magalhaes, M. Correia de Barros and A. Lima, "Earth return admittance effect on underground cable system modelling," IEEE Trans. Power Delivery, vol. 33, no. 2, pp. 662-670, 2018.

[61] R. J. Pogorzelski and D. C. Chang, "On the validity of the thin wire approximation in analysis of wave propagation along a wire over a ground," Radio Science, vol. 12, no. 5, pp. 699-707, 1977.

[62] CIGRE WG C4.501, "Guideline for Numerical Electromagnetic Analysis Method and its Application to Surge Phenomena," CIGRE, 2013.

[63] A. Pagnetti, A. Xemard, F. Paladian and C. A. Nucci, "Evaluation of the impact of proximity effect in the calculation of the internal impedance of the cylindrical conductors," in 30th General Assembly and Scientific Symposium, Istanbul, 2011.

[64] U. R. Patel, B. Gustavsen and P. Triverio, "An equivalent surface current approach for the computation of the series impedance of power cables with inclusion of skin and proximity effects," IEEE Trans. Power Delivery, vol. 28, no. 4, pp. 2474-2482, 2013.

[65] U. R. Patel, B. Gustavsen and P. Triverio, "Proximity - aware calculation of cable series impedance for systems of solid and hollow conductors," IEEE Trans. Power Delivery, vol. 28, no. 5, pp. 2101-2109, 2014.

[66] U. R. Patel and P. Triverio, "MoM - SO: A complete method for computing the impedance of cable systems including skin, proximity, and ground return effects," IEEE Trans. Power Delivery, vol. 30, no. 5, pp. 2110-2118, 2015.

[67] U. R. Patel and P. Triverio, "Accurate impedance calculation for underground and submarine power cables using MoM-SO and a multilayer ground model," IEEE Trans. Power Delivery, vol. 31, no. 3, pp. 1233-1241, 2016.

[68] B. Gustavsen, J. Sletbak and T. Henriksen, "Simulation of transient sheath overvoltages in the presence of proximity effects," IEEE Trans. Power Delivery, vol. 10, no. 2, pp. 1066-1075, 1995.

[69] B. Gustavsen, A. Bruaset, J. J. Bremnes and A. Hassel, "A finite-element approach for calculating electrical parameters of umbilical cables," IEEE Trans. Power Delivery, vol. 24, no. 4, pp. 2375-2384, 2009.

[70] S. Habib and B. Kordi, "Calculation of multiconductor underground cables high - frequency per - unit - length parameters using electromagnetic modal analysis," IEEE Trans. Power Delivery, vol. 28, no. 1, pp. 276-284, 2013.

[71] A. Ametani and K. Imanishi, "Development of exponential Fourier transform and its application to electrical transients," Proc. IEE, vol. 126, no. 1, pp. 51-56, 1979.

[72] N. Nagaoka and A. Ametani, "A development of a generalized frequency - domain transient program - FTP," IEEE Trans. Power Delivery, vol. 3, no. 4, pp. 1996-2004, 1988.

[73] P. Moreno and A. Ramirez, "Implementation of the numerical Laplace transform: a review," IEEE Trans. Power Delivery, vol. 23, no. 4, pp. 2599-2609, 2008.

[74] I. Kocar and J. Mahseredjian, "Accurate frequency dependent cable model for electromagnetic transients," IEEE Trans. Power Delivery, vol. 31, no. 3, pp. 1281-1288, 2016.

[75] IEC 60071-1, "Insulation Co-ordination Part 1: Definitions, Principles and Rules", IEC, 2006.

[76] IEC TR60071-4, "Insulation Co-ordination Part 4: Computational Guide to Insulation Co-ordination and Modeling of Electrical Networks," IEC, 2004.

[77] CIGRE WG D1.03, "Very Fast Transient Overvoltages (VFTO) in Gas - Insulated Substations," CIGRE, 2012.

[78] IEEJ WG, "Surge Phenomena Induced to Low - Voltage Circuits in Gas - Insulated Substations," IEEJ Technical Report, No. 273, 1988 (in Japanese).

[79] J. Meppelink, K. J. Diederich, K. Feser and W. R. Pfaff, "Very fast transients in GIS," IEEE Trans. Power Delivery, vol. 4, no. 1, pp. 223-233, 1989.

[80] C. M. Wiggins, D. E. Thomas, F. S. Nickel, T. M. Salas and S. E. Wright, "Transient electromagnetic interference in substations," IEEE Trans. Power Delivery, vol. 9, no. 4, pp. 1869-1884, 1994.

[81] ETRA WG, "Technology of Countermeasures against Surges in Protection and Control Systems in Japanese Utilities," Technical Report, vol. 57, no. 3, 2001 (in Japanese).

[82] T. Matsumoto, Y. Kurosawa, M. Usui, K. Yamashita and T. Tanaka, "Experience of numerical protective relays operating an environment with high - frequency switching surge in Japan," IEEE Trans. Power Delivery, vol. 20, no. 1, pp. 88-93, 2006.

[83] CIGRE WG C4.208, "EMC within Power Plants and Substations," CIGRE, 2013.

[84] IEC 61000-1, "Electromagnetic Compatibility (EMC) Part 1: General", IEC, 1992.

[85] J. A. Stratton, Electromagnetic Theory, New York: McGraw-Hill, 1941.

[86] A. Ametani, Y. Miyamoto and J. Mahseredjian, "Derivation of an earth - return impedance of an overhead multi - conductor considering displacement currents," IEEJ Trans. Power and Energy, vol. 134, no. 11, pp. 936-940, 2014.

[87] M. Abramowitz and I. A. Stegun, Handbook of Mathematical Functions with Formulas, Graphs, and Mathematical Tables, National Bureau of Standards, 1964.

[88] F. M. Tesche, M. Ianoz and T. Karlsson, EMC Analysis Methods and Computational Models, New York: John Wiley & Sons, INC., 1997.

[89] C. A. Nucci, F. Rachidi and M. Rubinstein, "Derivation of telegrapher's equations and field - to - transmission line interaction," WIT Trans. State - of - the - Art in Science and Engineering, vol. 29, pp. 1-20, 2008.

[90] F. Rachidi and S. V. Tkachenko, Electromagnetic Field Interaction with Transmission Lines: From Classical Theory to HF Radiation Effects, WIT Press, 2008.

[91] C. A. Nucci and F. Rachidi, Interaction of Electromagnetic Fields with Electrical Networks Generated by Lightning, Chapter 8 of The Lightning Flash: Physical and Engineering Aspects, IEE Press, London, 2003.

[92] F. Rachidi, "A review of field - to - transmission line coupling models with special emphasis to lightning - induced voltages on overhead lines," IEEE Trans. Electromagnetic Compatibility, vol. 54, no. 4, pp. 898-911, 2012.

[93] J. Chiba, "Studies in overhead wire - Goubau line above ground," IEEE Trans. Microwave Theory and Techniques, vol. 25, no. 2, pp. 83-93, 1977.

[94] R.G. Olsen, J.L. Young and D.C. Chang, "Electromagnetic wave propagation on a thin wire above earth," IEEE Trans. Antennas and Propagation, vol. 48, no. 9, pp. 1413-1419, 2000.

[95] A. Ametani, T. Goto, N. Nagaoka and H. Omura, "Induced surge characteristics on a control cable in a gas - insulated substation due to switching operation," IEEJ Trans. Power and Energy, vol. 127, no. 12, pp. 1306-1312, 2007.

[96] U. S. Gudmundsdottir, Modelling of Long High Voltage AC Cables in Transmission Systems, Aalborg: Aalborg University, 2010.

[97] A. Ametani, "Wave propagation characteristics of cables," IEEE Trans. Power Apparatus and Systems, vol. 99, no. 2, pp. 499-505, 1980.

[98] A. Ametani, "Surge propagation characteristics on a gas - insulated cables," IEEJ Trans. Power and Energy, Vol. 101, no. 8, pp. 491-497, 1981.

[99] H. Murase, I. Oshima, H. Aoyagi and I. Miwa, "Measurement of transient voltages induced by disconnect switch operation," IEEE Trans. Power Apparatus and Systems, vol. 104, no. 1, pp. 157-165, 1985.

[100] S. Ogawa, E. Haginomori, S. Nishiwaki, T. Yoshida and K. Terasaka, "Estimation of restriking transient overvoltage on disconnecting switch for GIS," IEEE Trans. Power Delivery, vol. 1, no. 2, pp. 95-102, 1986.

[101] J. Ozawa, T. Yamagiwa, M. Hosokawa, S. Takeuchi and H. Kozawa, "Suppression of fast transient overvoltage during gas disconnector switching in GIS," IEEE Trans. Power Delivery, vol. 1, no. 4, pp. 194-201, 1986.

[102] S. A. Boggs, F. Y. Chu and N. Fujimoto, Gas - Insulated Substations, Technology and Practice, New York: Pergamon Press, 1986.

[103] K. Nojima, S. Nishiwaki, H. Okubo and S. Yanabu, "Measurement of surge current and voltage waveforms using optical - transmission techniques," Proc. IEE, vol. 134, no. 6, pp. 415-422, 1987.

[104] N. Fujimoto and S. Boggs, "Characteristics of GIS disconnector - induced short rise time transients incident on externally connected power system components," IEEE Trans. Power Delivery, vol. 3, no. 3, pp. 961-970, 1988.

[105] S. Yanabu, H. Murase, H. Aoyagi, H. Okubo and Y. Kawaguchi, "Estimation of fast transient overvoltage in gas - insulated substation," IEEE Trans. Power Delivery, vol. 4, no. 4 , pp. 1875-1822, 1990.

[106] S. Nishiwaki, K. Nojima, S. Tatara, M. Kosakada, N. Tanabe and S. Yanabu, "Electromagnetic interference with electronic apparatus by switching surges in GIS - cable system," IEEE Trans. Power Delivery, vol. 10, no. 2, pp. 739-746, 1995.

[107] A. Ametani, H. Motoyama, K. Ohkawara, H. Yamakawa and N. Suga, "Electromagnetic disturbances of control circuits in power stations and substations experimented in Japan," Proc. IEE - Generation, Transmission and Distribution, vol. 3, no. 9, pp. 801-815, 2009.

[108] J. Smajic, W. Holaus, J. Kostovic and U. Riechert, "3D full - Maxwell simulations of very fast transients in GIS," IEEE Trans. Magnetics, vol. 47, no. 5, pp. 1514-1517, 2011.

[109] C. Li, J. He, J. Hu, R. Zeng and J. Yuan, "Switching transient of 1000 - kV UHV system considering detailed substation structure," IEEE Trans. Power Delivery, vol. 27, no. 1, pp. 112-122, 2012.

[110] G. Yue, W. Liu, W. Chen, Y. Guan and Z. Li, "Development of full frequency bandwidth measurement of VFTO in UHV GIS," IEEE Trans. Power Delivery, vol. 28, no. 4, pp. 2550-2557, 2013.

[111] S. Burow, U. Straumann, W. Kohler and S. Tenbohlen, "New methods of damping very fast transient overvoltages in Gas - Insulated Switchgear," IEEE Trans. Power Delivery, vol. 29, no. 5, pp. 2332-2339, 2014.

[112] J. G. R. Filho, J. A. Teixeira Jr, M. R. Sans and M. L. B. Martinez, "Very fast transient overvoltage waveshapes in a 500 - kV gas insulated switchgear setup," IEEE Electrical Insulation Magazine, vol. 32, no. 3, pp. 17-23, 2016.

[113] Z. Haznadar, S. Carsimamovic and R. Mahmutcehajic, "More accurate modeling of gas - insulated substation components in digital simulations of very fast electromagnetic transients," IEEE Trans. Power Delivery, vol.7, pp. 434-441, 1992.

[114] D. Povh, H. Scmitt, O. Volker and R. Witzmann, "Modeling and analysis guidelines for very fast transinets," IEEE Trans. Power Delivery, vol.11, no. 4, pp. 2028-2035, 1996.

[115] M. M. Rao, M.J. Thomas and B.P. Singh, "Frequency characteristics of very - fast transient currents in a 245 kV GIS," IEEE Trans. Power Delivery, vol. 20, no. 4, pp. 2450-2457, 2005.

[116] K. Nishimura, A. Ametani, N. Nagaoka and Y. Baba, "Modeling of a current transformer for electromagnetic transient simulation in a power station", CIGRE SC C4, Kushiro Colloquium, 2009.

[117] M. Szewczyk, K. Kutorasinski, M. Wronski and M. Florkowski, "Full - Maxwell simulation of very fast transients in GIS: case study to compare 3 - D and 2 - D - axisymmetric models of 1100kV test setup," IEEE Trans. Power Delivery, vol. 32, no. 2, pp. 733-739, 2017.

[118] A. Ametani, Distributed - Parameter Circuit Theory (in Japanese), Tokyo: Corona Pub, 1990.

[119] A. Ametani, K. Matsuoka, H. Omura and Y. Nagai, "Surge voltages and currents into a customer due to nearby lightning," Electric Power Systems Research, vol. 79, no. 3, pp. 428-435, 2009.

[120] A. Ametani, E. Ohsaki and Y. Honaga, "Surge characteristics on an untransposed vertical line," IEEJ Trans. Power and Energy, vol. 103, no. 2, pp. 117-124, 1983.

[121] N. Nagaoka and A. Ametani, "Transient calculations on crossbonded cables," IEEE Trans. Power Apparatus and Systems, vol. 102, no. 4, pp. 779-787, 1983.

[122] MATLAB Release 2014b, MathWorks, United States, 2014.

APPENDIX A - EXPRESSIONS OF SOMMERFELD INTEGRALS

In this appendix, the derived formulas of Sommerfeld integrals in previous chapters are summarized. The Sommerfeld integrals are numerically solved by using logarithmic sampling of Fourier transform [71] and validated by using global adaptive quadrature method in Matlab 2014b [122].

A.1 Sommerfeld integrals for a multi-phase overhead line

The functions $\Lambda_{0x}(y,z,d_m,h_m,v)$, $\Lambda_{0y}(y,z,d_m,h_m,v)$, $\Lambda_{0z}(y,z,d_m,h_m,v)$, $\Psi_{0x}(y,z,d_m,h_m,v)$, $\Psi_{0y}(y,z,d_m,h_m,v)$ and $\Psi_{0z}(y,z,d_m,h_m,v)$ in (2.19) to (2.24) are given by:

$$\begin{aligned}\Lambda_{0x}(y,z,d_m,h_m,v) = &-\frac{j\omega\mu_0}{4\pi}\left[\underline{\Delta}_1(y,z,d_m,h_m,v)+2\underline{S}_1(y,z,d_m,h_m,v)\right]\\ &+\frac{j\omega\mu_0 k_v^2}{4\pi k_a^2}\left[\underline{\Delta}_1(y,z,d_m,h_m,v)+2\underline{S}_2(y,z,d_m,h_m,v)\right]\end{aligned} \tag{A.1}$$

$$\Lambda_{0y}(y,z,d_m,h_m,v) = \frac{j\omega\mu_0 k_v}{4\pi k_a^2}\left[\underline{\Delta}_2(y,z,d_m,h_m,v)+2\underline{S}_4(y,z,d_m,h_m,v)\right] \tag{A.2}$$

$$\begin{aligned}\Lambda_{0z}(y,z,d_m,h_m,v) = -\frac{\omega\mu_0 k_v}{4\pi k_a^2}\Big[&\underline{\Delta}_3(y,z,d_m,h_m,v)+2k_a^2\underline{S}_7(y,z,d_m,h_m,v)\\ &-2k_v^2\underline{S}_8(y,z,d_m,h_m,v)-2\underline{S}_{10}(y,z,d_m,h_m,v)\Big]\end{aligned} \tag{A.3}$$

$$\Psi_{0x}(y,z,d_m,h_m,v) = \frac{k_v}{2\pi}\left[\underline{S}_5(y,z,d_m,h_m,v)-\underline{S}_6(y,z,d_m,h_m,v)\right] \tag{A.4}$$

$$\begin{aligned}\Psi_{0y}(y,z,d_m,h_m,v) = -\frac{1}{4\pi}\Big[&\underline{\Delta}_3(y,z,d_m,h_m,v)+2k_a^2\underline{S}_7(y,z,d_m,h_m,v)\\ &-2k_v^2\underline{S}_8(y,z,d_m,h_m,v)-2\underline{S}_9(y,z,d_m,h_m,v)\Big]\end{aligned} \tag{A.5}$$

$$\Psi_{0z}(y,z,d_m,h_m,v) = -\frac{j}{4\pi}\left[\underline{\Delta}_2(y,z,d_m,h_m,v)+2\underline{S}_3(y,z,d_m,h_m,v)\right] \tag{A.6}$$

with

$$\underline{\Delta}_1(y,z,d_m,h_m,v) = \int_{-\infty}^{+\infty}\frac{e^{-|z-h_m|u_{0v}}-e^{-(z+h_m)u_{0v}}}{u_{0v}}e^{-j(y-d_m)\lambda}d\lambda \tag{A.7}$$

$$\underline{\Delta}_2\left(y,z,d_m,h_m,v\right)=\int_{-\infty}^{+\infty}\frac{e^{-|z-h_m|u_{0v}}-e^{-(z+h_m)u_{0v}}}{u_{0v}}e^{-j(y-d_m)\lambda}\lambda d\lambda \tag{A.8}$$

$$\underline{\Delta}_3\left(y,z,d_m,h_m,v\right)=\int_{-\infty}^{+\infty}\left[e^{(z-h_m)u_{0v}}+e^{-(z+h_m)u_{0v}}\right]e^{-j(y-d_m)\lambda}d\lambda \text{ for } 0<z<h_m \tag{A.9}$$

$$\underline{\Delta}_3\left(y,z,d_m,h_m,v\right)=\int_{-\infty}^{+\infty}\left[e^{-(z+h_m)u_{0v}}-e^{-(z-h_m)u_{0v}}\right]e^{-j(y-d_m)\lambda}d\lambda \text{ for } z>h_m \tag{A.10}$$

$$\underline{S}_1\left(y,z,d_m,h_m,v\right)=\int_{-\infty}^{+\infty}\frac{e^{-(z+h_m)u_{0v}}}{u_{0v}+u_{1v}}e^{-j(y-d_m)\lambda}d\lambda \tag{A.11}$$

$$\underline{S}_2\left(y,z,d_m,h_m,v\right)=\int_{-\infty}^{+\infty}\frac{e^{-(z+h_m)u_{0v}}}{k_e^2k_a^{-2}u_{0v}+u_{1v}}e^{-j(y-d_m)\lambda}d\lambda \tag{A.12}$$

$$\underline{S}_3\left(y,z,d_m,h_m,v\right)=\int_{-\infty}^{+\infty}\frac{e^{-(z+h_m)u_{0v}}}{u_{0v}+u_{1v}}e^{-j(y-d_m)\lambda}\lambda d\lambda \tag{A.13}$$

$$\underline{S}_4\left(y,z,d_m,h_m,v\right)=\int_{-\infty}^{+\infty}\frac{e^{-(z+h_m)u_{0v}}}{k_e^2k_a^{-2}u_{0v}+u_{1v}}e^{-j(y-d_m)\lambda}\lambda d\lambda \tag{A.14}$$

$$\underline{S}_5\left(y,z,d_m,h_m,v\right)=\int_{-\infty}^{+\infty}\frac{e^{-(z+h_m)u_{0v}}}{u_{0v}\left(u_{0v}+u_{1v}\right)}e^{-j(y-d_m)\lambda}\lambda d\lambda \tag{A.15}$$

$$\underline{S}_6\left(y,z,d_m,h_m,v\right)=\int_{-\infty}^{+\infty}\frac{e^{-(z+h_m)u_{0v}}}{u_{0v}\left(k_e^2k_a^{-2}u_{0v}+u_{1v}\right)}e^{-j(y-d_m)\lambda}\lambda d\lambda \tag{A.16}$$

$$\underline{S}_7\left(y,z,d_m,h_m,v\right)=\int_{-\infty}^{+\infty}\frac{e^{-(z+h_m)u_{0v}}}{u_{0v}\left(u_{0v}+u_{1v}\right)}e^{-j(y-d_m)\lambda}d\lambda \tag{A.17}$$

$$\underline{S}_8\left(y,z,d_m,h_m,v\right)=\int_{-\infty}^{+\infty}\frac{e^{-(z+h_m)u_{0v}}}{u_{0v}\left(k_e^2k_a^{-2}u_{0v}+u_{1v}\right)}e^{-j(y-d_m)\lambda}d\lambda \tag{A.18}$$

$$\underline{S}_9\left(y,z,d_m,h_m,v\right)=\int_{-\infty}^{+\infty}\frac{e^{-(z+h_m)u_{0v}}}{u_{0v}\left(u_{0v}+u_{1v}\right)}e^{-j(y-d_m)\lambda}\lambda^2 d\lambda \tag{A.19}$$

$$\underline{S}_{10}\left(y,z,d_m,h_m,v\right)=\int_{-\infty}^{+\infty}\frac{e^{-\left(z+h_m\right)u_{0v}}}{u_{0v}\left(k_e^2k_a^{-2}u_{0v}+u_{1v}\right)}e^{-j\left(y-d_m\right)\lambda}\lambda^2d\lambda \tag{A.20}$$

A.2 Sommerfeld integrals for a multi-phase underground cable

The functions $\Lambda_{1x}\left(y,z,d_m,h_m,v\right)$, $\Lambda_{1y}\left(y,z,d_m,h_m,v\right)$, $\Lambda_{1z}\left(y,z,d_m,h_m,v\right)$, $\Psi_{1x}\left(y,z,d_m,h_m,v\right)$, $\Psi_{1y}\left(y,z,d_m,h_m,v\right)$ and $\Psi_{1z}\left(y,z,d_m,h_m,v\right)$ in (3.8) to (3.13) are given by:

$$\begin{aligned}\Lambda_{1x}\left(y,z,d_m,h_m,v\right)=&-\frac{j\omega\mu_0}{4\pi}\left[\underline{\Delta}_1^c\left(y,z,d_m,h_m,v\right)+2\underline{S}_1^c\left(y,z,d_m,h_m,v\right)\right]\\&+\frac{j\omega\mu_0k_v^2}{4\pi k_e^2}\left[\underline{\Delta}_1^c\left(y,z,d_m,h_m,v\right)+2\underline{S}_2^c\left(y,z,d_m,h_m,v\right)\right]\end{aligned} \tag{A.21}$$

$$\Lambda_{1y}\left(y,z,d_m,h_m,v\right)=\frac{j\omega\mu_0k_v}{4\pi k_e^2}\left[\underline{\Delta}_2^c\left(y,z,d_m,h_m,v\right)+2\underline{S}_4^c\left(y,z,d_m,h_m,v\right)\right] \tag{A.22}$$

$$\begin{aligned}\Lambda_{1z}\left(y,z,d_m,h_m,v\right)=&-\frac{\omega\mu_0k_v}{4\pi k_e^2}\left[\underline{\Delta}_3^c\left(y,z,d_m,h_m,v\right)-2k_e^2\underline{S}_7^c\left(y,z,d_m,h_m,v\right)\right.\\&\left.+2k_v^2\underline{S}_8^c\left(y,z,d_m,h_m,v\right)+2\underline{S}_{10}^c\left(y,z,d_m,h_m,v\right)\right]\end{aligned} \tag{A.23}$$

$$\Psi_{1x}\left(y,z,d_m,h_m,v\right)=\frac{k_v}{2\pi}\left[\underline{S}_5^c\left(y,z,d_m,h_m,v\right)-\underline{S}_6^c\left(y,z,d_m,h_m,v\right)\right] \tag{A.24}$$

$$\begin{aligned}\Psi_{1y}\left(y,z,d_m,h_m,v\right)=&\frac{1}{4\pi}\left[\underline{\Delta}_3^c\left(y,z,d_m,h_m,v\right)-2k_e^2\underline{S}_7^c\left(y,z,d_m,h_m,v\right)\right.\\&\left.+2k_v^2\underline{S}_8^c\left(y,z,d_m,h_m,v\right)+2\underline{S}_9^c\left(y,z,d_m,h_m,v\right)\right]\end{aligned} \tag{A.25}$$

$$\Psi_{1z}\left(y,z,d_m,h_m,v\right)=\frac{j}{4\pi}\left[\underline{\Delta}_2^c\left(y,z,d_m,h_m,v\right)+2\underline{S}_3^c\left(y,z,d_m,h_m,v\right)\right] \tag{A.26}$$

with

$$\underline{\Delta}_1^c\left(y,z,d_m,h_m,v\right)=\int_{-\infty}^{+\infty}\frac{e^{-\left|z-h_m\right|u_{1v}}-e^{\left(z+h_m\right)u_{1v}}}{u_{1v}}e^{-j\left(y-d_m\right)\lambda}d\lambda \tag{A.27}$$

$$\underline{\Delta}_2^c\left(y,z,d_m,h_m,v\right)=\int_{-\infty}^{+\infty}\frac{e^{-\left|z-h_m\right|u_{1v}}-e^{\left(z+h_m\right)u_{1v}}}{u_{1v}}e^{-j\left(y-d_m\right)\lambda}\lambda d\lambda \tag{A.28}$$

$$\underline{\Delta}_3^c\left(y,z,d_m,h_m,v\right)=\int_{-\infty}^{+\infty}\left[e^{(z-h_m)u_{1v}}-e^{(z+h_m)u_{1v}}\right]e^{-j(y-d_m)\lambda}d\lambda \text{ for } z<h_m \tag{A.29}$$

$$\underline{\Delta}_3^c\left(y,z,d_m,h_m,v\right)=\int_{-\infty}^{+\infty}\left[-e^{(-z+h_m)u_{1v}}-e^{(z+h_m)u_{1v}}\right]e^{-j(y-d_m)\lambda}d\lambda \text{ for } h_m<z<0 \tag{A.30}$$

$$\underline{S}_1^c\left(y,z,d_m,h_m,v\right)=\int_{-\infty}^{+\infty}\frac{e^{(z+h_m)u_{1v}}}{u_{0v}+u_{1v}}e^{-j(y-d_m)\lambda}d\lambda \tag{A.31}$$

$$\underline{S}_2^c\left(y,z,d_m,h_m,v\right)=\int_{-\infty}^{+\infty}\frac{e^{(z+h_m)u_{1v}}}{u_{0v}+k_a^2k_e^{-2}u_{1v}}e^{-j(y-d_m)\lambda}d\lambda \tag{A.32}$$

$$\underline{S}_3^c\left(y,z,d_m,h_m,v\right)=\int_{-\infty}^{+\infty}\frac{e^{(z+h_m)u_{1v}}}{u_{0v}+u_{1v}}e^{-j(y-d_m)\lambda}\lambda d\lambda \tag{A.33}$$

$$\underline{S}_4^c\left(y,z,d_m,h_m,v\right)=\int_{-\infty}^{+\infty}\frac{e^{(z+h_m)u_{1v}}}{u_{0v}+k_a^2k_e^{-2}u_{1v}}e^{-j(y-d_m)\lambda}\lambda d\lambda \tag{A.34}$$

$$\underline{S}_5^c\left(y,z,d_m,h_m,v\right)=\int_{-\infty}^{+\infty}\frac{e^{(z+h_m)u_{1v}}}{u_{1v}\left(u_{0v}+u_{1v}\right)}e^{-j(y-d_m)\lambda}\lambda d\lambda \tag{A.35}$$

$$\underline{S}_6^c\left(y,z,d_m,h_m,v\right)=\int_{-\infty}^{+\infty}\frac{e^{(z+h_m)u_{1v}}}{u_{1v}\left(u_{0v}+k_a^2k_e^{-2}u_{1v}\right)}e^{-j(y-d_m)\lambda}\lambda d\lambda \tag{A.36}$$

$$\underline{S}_7^c\left(y,z,d_m,h_m,v\right)=\int_{-\infty}^{+\infty}\frac{e^{(z+h_m)u_{1v}}}{u_{1v}\left(u_{0v}+u_{1v}\right)}e^{-j(y-d_m)\lambda}d\lambda \tag{A.37}$$

$$\underline{S}_8^c\left(y,z,d_m,h_m,v\right)=\int_{-\infty}^{+\infty}\frac{e^{(z+h_m)u_{1v}}}{u_{1v}\left(u_{0v}+k_a^2k_e^{-2}u_{1v}\right)}e^{-j(y-d_m)\lambda}d\lambda \tag{A.38}$$

$$\underline{S}_9^c\left(y,z,d_m,h_m,v\right)=\int_{-\infty}^{+\infty}\frac{e^{(z+h_m)u_{1v}}}{u_{1v}\left(u_{0v}+u_{1v}\right)}e^{-j(y-d_m)\lambda}\lambda^2 d\lambda \tag{A.39}$$

$$\underline{S}_{10}^c\left(y,z,d_m,h_m,v\right)=\int_{-\infty}^{+\infty}\frac{e^{(z+h_m)u_{1v}}}{u_{1v}\left(u_{0v}+k_a^2k_e^{-2}u_{1v}\right)}e^{-j(y-d_m)\lambda}\lambda^2 d\lambda \tag{A.40}$$

$$\underline{S}_{11}^{c}\left(y,z,d_m,h_m,v\right)=\int_{-\infty}^{+\infty}\frac{e^{\left(z+h_m\right)u_{1v}}}{u_{1v}^{2}\left(u_{0v}+u_{1v}\right)}e^{-j\left(y-d_m\right)\lambda}\lambda^{2}d\lambda \tag{A.41}$$

$$\underline{S}_{12}^{c}\left(y,z,d_m,h_m,v\right)=\int_{-\infty}^{+\infty}\frac{e^{\left(z+h_m\right)u_{1v}}}{u_{1v}^{2}\left(u_{0v}+k_a^{2}k_e^{-2}u_{1v}\right)}e^{-j\left(y-d_m\right)\lambda}\lambda^{2}d\lambda \tag{A.42}$$

$$\underline{S}_{13}^{c}\left(y,z,d_m,h_m,v\right)=\int_{-\infty}^{+\infty}\frac{e^{\left(z+h_m\right)u_{1v}}}{u_{1v}^{2}\left(u_{0v}+u_{1v}\right)}e^{-j\left(y-d_m\right)\lambda}d\lambda \tag{A.43}$$

$$\underline{S}_{14}^{c}\left(y,z,d_m,h_m,v\right)=\int_{-\infty}^{+\infty}\frac{e^{\left(z+h_m\right)u_{1v}}}{u_{1v}^{2}\left(u_{0v}+k_a^{2}k_e^{-2}u_{1v}\right)}e^{-j\left(y-d_m\right)\lambda}d\lambda \tag{A.44}$$

APPENDIX B - LIST OF PUBLICATIONS

H. Xue, A. Ametani, J. Mahseredjian, Y. Baba, F. Rachidi and I. Kocar, "Transient responses of overhead cables due to mode transition in high frequencies," IEEE Trans. Electromagnetic Compatibility, vol. 60, no. 3, pp. 785-794, 2018.

H. Xue, A. Ametani, J. Mahseredjian, Y. Baba and F. Rachidi, "Frequency response of electric and magnetic fields of overhead conductors with particular reference to axial electric field," IEEE Trans. Electromagnetic Compatibility, DOI: 10.1109/TEMC.2017.2763952.

H. Xue, A. Ametani, J. Mahseredjian and I. Kocar, "Generalized formulation of earth - return impedance / admittance and surge analysis on underground cables," IEEE Trans. Power Delivery, DOI: 10.1109/TPWRD.2018.2796089.

A. Ametani, **H. Xue**, M. Natsui and J. Mahseredjian, "Electromagnetic disturbances in gas - insulated substations and VFT calculations," Electric Power System Research, vol. 160, pp. 191-198, 2018.

H. Xue, A. Ametani and J. Mahseredjian, "Very fast transients in a 500 kV gas - insulated substation," submitted to IEEE Trans. Power Delivery, under review - minor comments.

H. Xue, A. Ametani, J. Mahseredjian and I. Kocar, "Review of earth - return impedance / admittance and the application to surge propagation on overhead lines," IEEJ High Voltage Engineering Technical Meeting, Montreal, 2018.

A. Ametani, M. Natsui, **H. Xue**, J. Mahseredjian and T. Goto, "Effect of elbow part of gas-insulated bus on surge propagation in GIS," IEEJ High Voltage Engineering Technical Meeting, Montreal, 2018.

H. Xue, A. Ametani, J. Mahseredjian and I. Kocar, "Computation of overhead line / underground cable parameters with improved MoM - So method," Power Systems Computation Conference (PSCC), Dublin, 2018.

H. Xue, A. Ametani and J. Mahseredjian, "Complete electromagnetic earth - return parameters on multi - phase underground cables - part I: theory," IEEJ High Voltage Engineering Technical Meeting, Okinawa, 2018.

H. Xue, A. Ametani and J. Mahseredjian, "Complete electromagnetic earth - return parameters on multi - phase underground cables - part II: calculation examples," IEEJ High Voltage Engineering Technical Meeting, Okinawa, 2018.

A. Ametani, **H. Xue**, J. Mahseredjian and I. Kocar, "Numerical instabilities of very - fast - transients in EMTP simulation," IEEJ High Voltage Engineering Technical Meeting, Okinawa, 2018.

A. Ametani, **H. Xue**, M Cervantes, I. Kocar and T. Noda, "A study on the effect of a source circuit on switching surges," IEEJ High Voltage Engineering Technical Meeting, Okinawa, 2018.

H. Xue, "Formulations of earth - return impedance and admittance for overhead / underground cables," International Symposium on EMC and Transients in Infrastructures (ISET) and International Student Session (ISS), Kyoto, 2017.

H. Xue, M. Natsui, A. Ametani, J. Mahseredjian, H. Tanaka and Y. Baba, "Comparison of transient simulations on overhead cables by EMTP and FDTD," International Conference on Power Systems Transients (IPST), Seoul, 2017.

A. Ametani, **H. Xue**, M. Natsui and J. Mahseredjian, "Electromagnetic disturbances in gas - insulated substations and VFT calculations," International Conference on Power Systems Transients (IPST), Seoul, 2017. (Best Conference Paper - Top 10%)

A. Ametani, Y. Baba, Y. Miyamoto, T. Asada, **H. Xue** and J. Mahseredjian, "Phase velocity on overhead conductors in high frequencies," IEEJ Power and Energy Conference, Kyushu, 2016.